UNIVERSITÀ DEGLI STUDI DI TORINO

DOCTORAL THESIS

Innovative thin silicon sensors for beam monitoring in particle and FLASH radiotherapy

---

Author:
Oscar A. MARTI VILLARREAL

Supervisor:
Dr. Anna VIGNATI

A thesis submitted in fulfillment of the requirements for the degree of Doctor of Philosophy

in the

Research Group: Medical Physics
Department of Physics

May 16, 2023

Declaration of Authorship

I, Oscar A. MARTI VILLARREAL, declare that this dissertation titled, "Innovative thin silicon sensors for beam monitoring in particle and FLASH radiotherapy" and the content presented in it are my own original work and do not in any way compromise the rights of third parties, including those related to the security of personal data.

Signed: 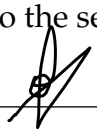

Date: 16/05/2023

"THE ONLY PERSON WHO NEVER MAKES A MISTAKE IS THE PERSON WHO NEVER DOES ANYTHING"

THEODORE ROOSEVELT

UNIVERSITÀ DEGLI STUDI DI TORINO

Abstract

Coordinator: Paolo Olivero
Department of Physics

Doctor of Philosophy

Innovative thin silicon sensors for beam monitoring in particle and FLASH radiotherapy

by Oscar A. MARTI VILLARREAL

The work carried out in this thesis was part of three National Institute of Nuclear Physics (INFN) projects called: Modeling and Verification for Ion beam Treatment planning (MoVe-IT)[1], Superconducting Ion Gantry (SIG), and Flash Radiotherapy with hIgh Dose-rate particle beAms (FRIDA)[2].
Within the MoVe-IT project, two prototypes of silicon sensors were developed. The first one is a proton counter to be used as an online monitor of the fluence rate of clinical proton beams (Vignati et al., 2017; Sacchi et al., 2020; Fausti et al., 2021) and the second is a device able to measure the beam energy using Time-of-Flight technique (Marti Villarreal et al., 2021; Vignati et al., 2020a). The sensors used in these two prototypes represent an evolution of the n-on-p planar silicon sensor where a thin (1 micrometer) p^+ gain layer is implanted under the n^{++} cathode. As a result of the doping profile, characterized by a large doping concentration at the n^{++}/p^+ junction, a local increase of the electric field up to 300 kV/cm in this region creates a controlled moderate electron/hole avalanche multiplication without a complete breakdown. This effect leads to a proportional signal enhancement with a noise level similar to that of a traditional silicon sensor of the same geometry. In 2020, we designed several sensors with diverse characteristics tailored to the needs of the two devices developed. The production is called MoVe-IT-2020. They are segmented into strips to reduce the particle rate per channel and minimize the signal pile-up. Chapter 2 describes the laboratory characterization of all the sensors used in this thesis. Additionally, the signals obtained in a preliminary test with proton beams at the National Centre for Oncological Hadrontherapy (CNAO, Pavia, Italy) are presented, using a sensor with a large area from the MoVe-IT-2020 production. In chapter 3, the results of the telescope system proposed by the University of Turin and the National Institute of Nuclear Physics (Turin Section) in two Italian particle therapy centers are presented and discussed.
Developments similar to the MoVe-IT project for clinical carbon ion beams are in progress within the SIG project. Chapter 4 reports the measurements of individual carbon ions in the CNAO clinical beam with 60 μm thick silicon sensors.
Within the FRIDA project, the University and INFN of Turin are studying thin silicon sensors, recently designed and produced for single particle tracking in proton therapy, for electron beam monitoring in high dose-rate regimes. Chapter 5 describes the results of testing thin silicon sensors at Ultra-High

[1] https://www.tifpa.infn.it/projects/move-it/
[2] https://web.infn.it/FRIDA/index.php/en/

dose rate (UHDR). In addition, the partial results of the first attempt to upgrade the LINAC (Elekta SL 25 MV) installed in the Physics Department of the University of Turin, dedicated entirely to research, is presented, which will allow in the near future experiments to study the FLASH effect.
During my PhD, I wrote the following papers: Marti Villarreal et al., 2021; Villarreal et al., 2023; Villarreal et al., 2022, which reported the same results presented in this thesis. The content of chapter 2 has been described in Villarreal et al., 2023; Villarreal et al., 2022 and a summary of the content of chapter 3 has been published in Marti Villarreal et al., 2021. Additionally, my work along my PhD contributed also to the following papers: Vignati et al., 2020c; Vignati et al., 2020a; Vignati et al., 2022b; Croci et al., 2023; Mohammadian-Behbahani et al., 2022; Giordanengo et al., 2022; Pennazio et al., 2022; Vignati et al., 2022a; Vignati et al., 2020b.

Acknowledgements

To my wife and my son, the only reason why all this sacrifice made some sense in the first place. You have been the motivation, support, and the driving force.
To all my family and my wife's family who, despite being so far away, have always been there to supported me.
To my supervisor Anna, you deserves much more praise than myself for this work in all the senses... including the patience to overcome the countless setbacks, the unconditional availability and, of course, the human support.
My sincere thanks also go to the entire Medical Physics Group of Torino in special: Felix, Diango, Cirio, Simona, Sacchi, Vincenzo, Mohammed, Emanuele, Davide, and Elisabetta for keeping me on track and for always being there whenever I needed your help. Thanks for allowing me to learn so much from all of you.
To the external reviewers of this thesis for all your comments, suggestions, and for your time which helped to improve the manuscript.
I also would like to express my special appreciation to the UFSD group of INFN-Torino, the electronic lab of Torino, Flori, Barbara, and the staff of CNAO, TIFPA, and FBK. It was a great pleasure collaborating with them. Thank you for your help and allowing me access to your labs and facilities.
To the University of Torino for the opportunity.
Thanks to all of you. I am very grateful for all the personal, professional and academic growth and for all the experiences. The way was hard, but there is no resurrection without Calvary.
The author

Contents

List of Figures

List of Tables

To my wife Yaimarys and my son Gael

Chapter 1

Introduction

1.1 Radiotherapy with charged particle beams

In 2020, according to GLOBOCAN 2020 (Sung et al., 2021), an estimated 19.3 million new cancer cases occurred worldwide. Furthermore, among the data taken in 57 from 183 countries in 2019, cancer is the leading cause of death before the age of 70, as shown in Fig. 1.1, and is responsible for one in six deaths.

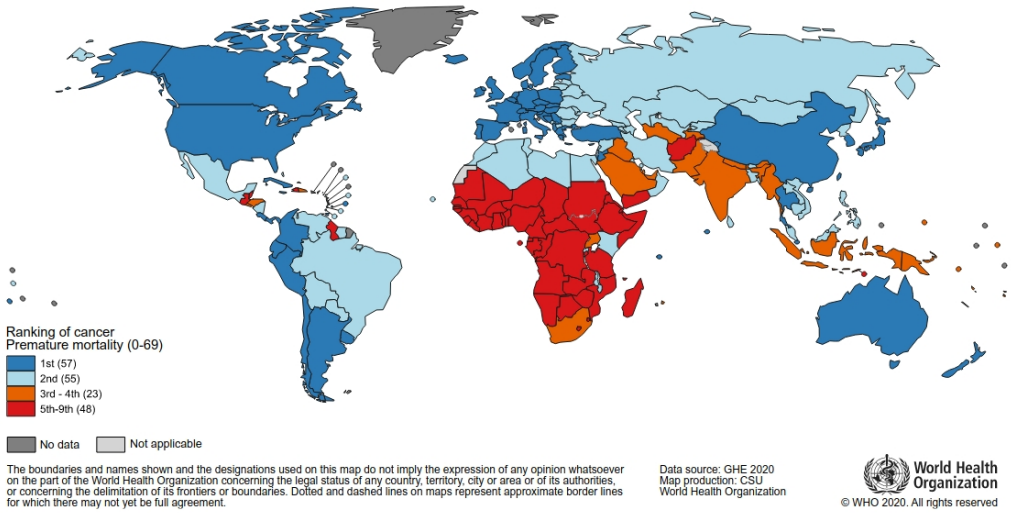

FIGURE 1.1: National Ranking of Cancer as a Cause of Death at Ages < 70 Years in 2019. The numbers of countries represented in each ranking group are included in the legend. Figure taken from (Sung et al., 2021).

Nowadays, conventional treatment approaches such as surgery, chemotherapy, and radiotherapy are used to treat cancer. At the same time, recent advances have been made to improve the patient's outcome, which includes stem cell therapy, targeted therapy, ablation therapy, nanoparticles, natural antioxidants, radionics, chemodynamic therapy, sonodynamic therapy, and

ferroptosis-based therapy (Debela et al., 2021).
However, still, more than 50% of patients with diagnosed cancer undergo radiation therapy, typically combined with other treatment modalities such as surgery and chemotherapy. Radiotherapy encompasses all the methodologies that use radiation for therapeutic purposes and mainly focuses on cancer treatment and can be divided into two branches: External beam radiation therapy (EBRT) and Brachytherapy. Within EBRT, we can find: superficial X-ray (also known as Orthovoltage), megavoltage electron and photon beams (produced with electron linear accelerators) radiotherapy, gamma-ray therapy, hadrontherapy (protons, ions), and intraoperative radiotherapy.
When it is used radiotherapy to treat tumors, exists a therapeutic window in which the dose delivered to the patients has to be enough to provide high Tumor Control Probability (TCP ≥ 0.5) with a moderate Normal Tissue Complications Probability (NTCP ≤ 0.05). Progress in radiotherapy has always been related to improved dose distribution, which is well-linked to the performance of accelerators, beam delivery, and treatment planning systems. At first, it was thanks to increasing the energy of the photons until reaching the megavoltage range that improved the patients' survival rate. Although radiotherapy with photons has continuously increased, the physical limitation of the photon beams makes it impossible to avoid a high dose contribution in the region before/beyond the tumor, as shown in Fig. 1.2a. On the other hand, the phenomenon of the Bragg peak in particle therapy is applied to maximize the dose in the target and minimize the dose in healthy tissue (see Fig. 1.2a and Fig. 1.2b). Therefore, particle therapy delivers radiation to tumors and areas nearby, decreasing integral radiation dose to normal tissues and theoretically avoiding collateral damage.
Worldwide, by the end of 2021, about 325000 patients have been treated with Particle Therapy, mainly using protons (280000) and C-ions (42000) (PTCOG, 2021). Although the number of centers treating tumors with light ions (mainly protons) has increased in the last decade, its growth is still low compared to conventional radiotherapy, mainly due to its cost. For example, including a cyclotron, multi-story gantries, and multiple treatment rooms, the average cost of a proton facility ranges from 140 million and 200 million euro (Kryder, 2017).

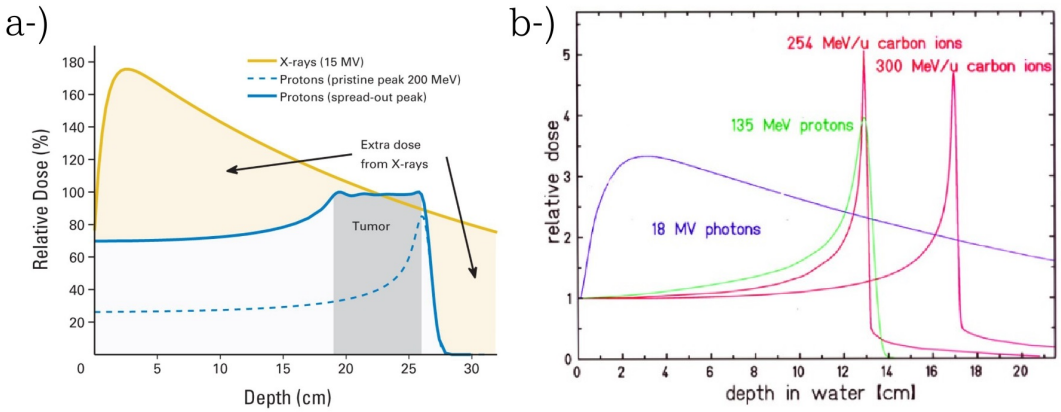

FIGURE 1.2: (a) Relative dose as a function of depth for X-rays and protons. For the protons, the typical Spread-Out Bragg Peak (SOBP) can be seen, which is obtained by a superposition of protons at different energies. Figure taken from (Mitin and Zietman, 2014). (b) Relative Dose as a function of depth in water for 18 MV photons, 135 MeV protons, and carbon ions of 254 MeV/u and 300 MeV/u. Figure taken from (Durante and Paganetti, 2016).

1.1.1 FLASH Radiotherapy (FLASH-RT)

The so-called FLASH effect is a radiobiological effect that reduces the damage to healthy tissue while maintaining the therapeutic efficacy on tumor tissue obtained by drastically reducing the delivery time of the treatment dose, for instance, the total irradiation time below 200 ms with a dose-rate higher than 40 Gy/s (Vignati et al., 2020c). It is important to remark that today a dose-rate of about 8 Gy/min in conventional radiotherapy is considered high. These parameters indicate the order of magnitude in which the FLASH effect was observed.

The FLASH effect has been verified experimentally in different centers worldwide for diverse tissue such as the brain, lungs, skin, etc., mainly using low-energy electrons beam (4-7 MeV) but also with protons and carbon ions. For example, (Favaudon, 2014) reported one of the more notable experimental studies on FLASH effect. The authors made an in-vitro study of lung tissue in mice and confirmed that FLASH is effective against tumor cells but causes minor damage to normal tissue. These results suggest that FLASH-RT may be a viable option for treating lung tumors, although this will need to be confirmed in human patients. Another study performed in mice (Montay-Gruel et al., 2017) demonstrated that FLASH with mean dose rates above 100 Gy/s preserves mouse memory; instead, when used at 10 Gy at conventional radiotherapy (0.1 G/s) the spatial memory is affected. The first study with

FLASH-RT in a human was performed by (Bourhis et al., 2019). In that investigation, a 75-year-old patient with a multi-resistant cutaneous lymphoma was treated with 15 Gy in 90 ms with 5.6 MeV electrons accelerated by a LINAC, specifically designed for FLASH-RT with a favorable outcome for both: normal skin and the tumor.
The multiple benefits of using FLASH-RT in the near future have been widely pointed out. For instance, it would allow treating radioresistant tumors, increasing the total dose without the associated surrounding tissue toxicity of conventional radiotherapy. It would also treat tumors where the radiotherapy already offers reasonable local control but without the side effect typical of conventional radiotherapy.
Today, the implementation of FLASH-RT at the clinical level is not yet possible because the technology and equipment necessary to deliver the doses per pulse to trigger the FLASH effect are still in the research and development phase. Likewise, dosimetric protocols and radiobiological clinical studies must be defined and tested. Therefore, the international community is focused on overcoming all the mentioned limitations, first by upgrading current LINAC accelerators to run quantitative experiments with the aim of testing new sensors for beam monitoring and dosimetry, conducting preclinical studies and developing treatment planning systems.

1.2 Basic concepts of interaction and detection of charged particles

1.2.1 Interaction of charged particles with matter

Interaction of heavy charge particle with matter

The particles with charge *ze* more massive than electrons are called "heavy" charged particles (Patrignani, 2016). The main mechanism of interaction of heavy charged particles (For example: protons, alpha particles, light ions, etc) with atoms in an absorbing medium is through Coulomb forces between their positive charge and the negative charge of orbiting electrons. Although these particles can directly or indirectly interact with the nuclei, these interactions are not significant.
After entering any material, charged particles simultaneously interact with many electrons in their respective track. Electrons in the vicinity of the path of the positively charged particle feel the attractive Coulomb force, as soon

as it approaches. Depending on how close the encounter is, the interaction between the projectile (charged particle) and the orbiting electron can either excite the electrons (i.e., move them to a higher energy shell within the atom) or eject them. Since energy must be conserved, the energy transferred to the electron is given by the projectile's velocity loss. The maximum energy that can be transferred in this type of interaction to the electron of mass (m_0) by the charged particle of mass (m) and kinetic energy (E) in a simple collision is $4Em_0/m$, which is a tiny fraction of its total energy. The primary charged particle gradually loses its energy in many small interactions with the electrons during its passage through the medium until it is completely stopped. The trajectory of the projectile, except when its energy is small (almost before stopping), is in a straight line since it only deflected small angles in its interactions with the electrons of the medium. Thus, heavy charged particles are characterized by a defined range in a given absorbent material, representing the distance beyond which no particle will penetrate.

Other interaction needs to be considered, particularly in the close encounters between the projectile and the electrons of the medium, resulting in fast electrons from the ionization process. These energetic electrons (also called δ-rays) can ionize or excite other atoms in the material, and for thinner absorbers they can escape from the medium. Therefore, the deposited energy will be lower than the lost energy for the incoming particle (Leroy and Rancoita, 2011). This phenomenon must be taken into account in the detectors used in this thesis due to their thickness.

The linear stopping power (S) for charged particles in a given medium is defined as the differential of the mean energy lost (dE) by the charged particle within a material divided by the differential of the path traveled (dx), as shown below:

$$S = -\frac{dE}{dx} \tag{1.1}$$

where, $-\frac{dE}{dx}$ is called the rate of energy loss, and it is well described by the Bethe-Bloch formula, which for an incoming particle of mass m_p, velocity equal to $v = \beta c$, charge number: z and, thus, charge ze, can be written as follows (Leroy and Rancoita, 2011):

$$-\frac{dE}{dx} = \frac{2\pi n z^2 e^4}{m_e v^2}\left(\ln\left[\frac{2m_e v^2 W_m}{I^2(1-\beta^2)}\right] - 2\beta^2 - \delta - U\right) \tag{1.2}$$

where:
m_e: is the electron mass
n: is the number of electrons per cm^3 of the traversed material
I: is the mean excitation energy of the atoms of the material
W_m: is the maximum energy transfer from the incident particle to atomic electrons
δ: is the density effect correction factor[1]
U: is the shells effect correction factor[2]
β: is the ratio of v to c
c: is the speed of light
The number of electrons per cm^3 of the traversal material is obtained by the next expression:

$$n = \frac{Z\rho N_A}{A} \tag{1.3}$$

where:
ρ: is the density of the target
N_A: is the Avogadro constant
Z: is the atomic number
A: is the relative atomic mass of the target

The maximum energy transfer (W_m) from the incident particle to atomic electrons is obtained using the two-body scattering (Leroy and Rancoita, 2011) in which the target particle is almost at rest, and it is given by:

$$W_m = 2m_e c^2 \beta^2 \gamma^2 [1 + (\frac{m_e}{m})^2 + 2\gamma \frac{m_e}{m}]^{-1} \tag{1.4}$$

where:
m: is mass of the incident particle
γ: is the Lorentz factor

For incoming particles such as proton and carbon ions, in which the masses

[1] It is because the electrons farther from the projectile path are shielded from the full strength of the electric field by the electrons close to the particle. It makes a reduction in the energy loss. Depends on the particle velocity and the density of the material, in which it is greater for high velocities and material with higher densities.

[2] It is due to non-participation of inner shells electrons in the collision loss process and is equal to $2(\frac{C}{Z})$. This terms is important and can not be neglected for charged particles with energies lower than few MeV/u in which the particle velocity is near the velocity of the atomic electrons.

are much larger than the one of the electrons, the expression 1.4 can be rewritten as:

$$W_m = 2m_e c^2 \beta^2 \gamma^2 \tag{1.5}$$

Substituting equations 1.3 and 1.5 in 1.2, we obtain the following expression for the energy-loss formula:

$$-\frac{dE}{dx} = \frac{4\pi Z \rho N_A z^2 e^4}{m_e v^2 A}(\ln[\frac{2m_e v^2 \gamma^2}{I}] - \beta^2 - \delta/2 - U/2) \tag{1.6}$$

Equation 1.6 can conveniently be rewritten as follows, taking into account, the classical electron radius $r_e = \frac{e^2}{m_e c^2}$,

$$-\frac{dE}{dx} = \frac{4\pi N_A m_e c^2 r_e^2 \rho z^2 Z}{A\beta^2}(\ln[\frac{2m_e v^2 \gamma^2}{I}] - \beta^2 - \delta/2 - U/2) \tag{1.7}$$

As can be seen, the Bethe Bloch formula shows a dependence proportional to the electron density of the target $(\frac{Z\rho N_A}{A})$ and the square of particle charge (z), for instance, $z = 1$ for protons. Additionally, $4\pi N_A m_e c^2 r_e^2$ is a constant equal to 0.307 $MeVcm^2mol^{-1}$, thus, the Bethe-Bloch formula can be re-written as follow:

$$-\frac{dE}{dx} = \frac{0.3071 \rho z^2 Z}{A\beta^2}(\ln[\frac{2m_e v^2 \gamma^2}{I}] - \beta^2 - \delta/2 - U/2)[MeV/cm] \tag{1.8}$$

For instance, in Fig. 1.3 is shown a plot in log-log scale of the mass stopping power $MeVcm^2/g$ for positive muons in copper as a function of $\beta\gamma$. The equation 1.8 describes with an accuracy of a few percent the mean rate of energy loss in the region between $0.1 \lesssim \beta\gamma \lesssim 1000$ for intermediate-Z materials, the Bethe region of Fig. 1.3. In the Bethe region the dominant form of energy losses for a charged heavy particle are collisions with atomic electrons from the medium that transfer their energy in ionization and excitation of these atoms. For low (non relativistic) energies, the energy loss rate shows a dependence inversely proportional to the square of the incoming particle velocity $(1/\beta)$, therefore, decrease with increasing the velocity until about $v = 0.96c$, where the minimum is reach, as shown also in Fig. 1.3.
By definition, a particle whose energy loss is at the minimum of the Bethe-Bloch function is called a Minimum Ionization Particle (MIP), and is almost

the same for all particles of the same charge. After this minimum, as the energy increases beyond this point, the term $(1/\beta)$ becomes almost constant and dE/dx rises again due to the logarithmic dependence. As can be observed, the Bethe-Bloch formula is not applicable at very low energies $\beta \leq 0.05$ (which is about 1 MeV for protons).
On the right-hand side of the plot in Fig. 1.3, it can be seen that the density effect term of the Bethe-Bloch formula becomes important for the high energy range. Also, at sufficiently high energies, the radiative process becomes more important than ionization for all charged particles. Additionally, the energy losses due to bremsstrahlung which depend on the particle and is not simply as a function of β, dominate by above a certain value, the so-called critical energy. It is shown in Fig. 1.3 for muon as: $E_{\mu c}$, it is defined as the energy at which radiative and ionization losses are equal. At very low energies, it is shown the "Barkas effect" as -μ. This effect is due to at low energies, heavier ions collect electron from the surrounding material thus rapidly decreasing its z_{eff} (Leroy and Rancoita, 2011; Patrignani, 2016).

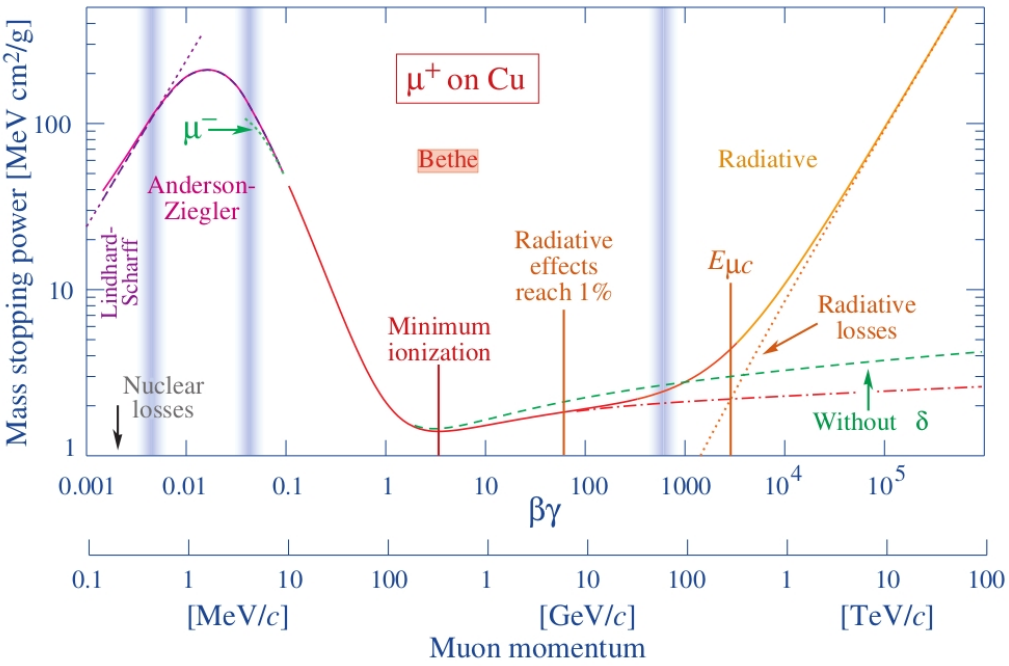

FIGURE 1.3: Mass stopping power for positive muons in copper as a function of $\beta\gamma = p/Mc$ over nine orders of magnitude in momentum. Solid curves indicate the total stopping power. Vertical bands indicate boundaries between different approximations. The short dotted lines labeled "$\mu-$" illustrate the "Barkas effect". Picture taken from (Patrignani, 2016).

Fig. 1.4 shows the mass stopping power as a function of protons energy for

different materials such as: Silicon,Titanium, Copper, Silver, and Lead. All curves have a similar shape, showing that there is a tendency to decrease the rate of energy loss with increasing atomic number (Si<Ti<Cu<Ag< Pb). In silicon the minimum ionization occurs at 2500 MeV, which corresponds to a mass stopping power of 1.661 $MeVcm^2/g$, this means that the stopping power is 3.87 MeV/cm for a MIP.

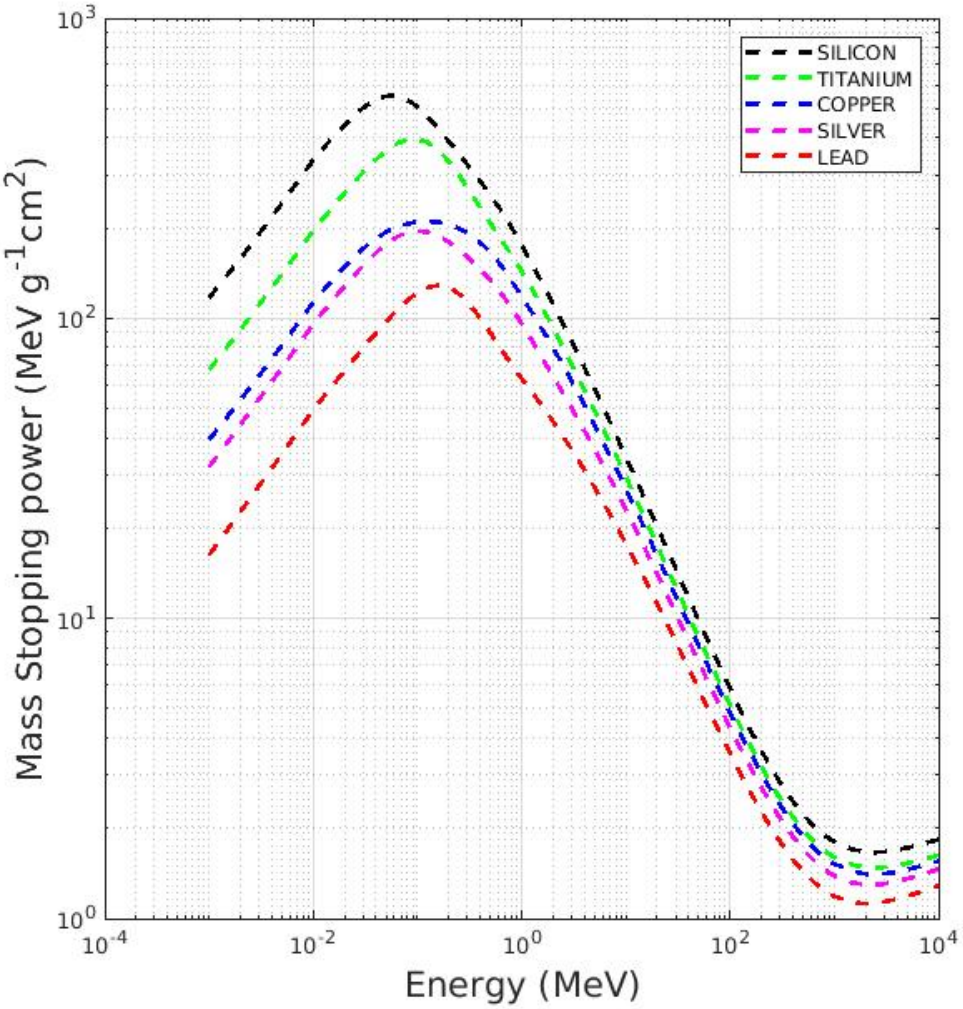

FIGURE 1.4: Mass stopping power as a function of protons energy for different materials.

For the proton energy range used in this work: 62.6 MeV (4.9 MIP) to 230 MeV (2 MIP), which roughly corresponds to the conventional clinical range, the stopping power in Si ranges from 19.12 MeV/cm to 7.74 MeV/cm, respectively. In addition, the MIP crossing a silicon sensor produces, by ionization (Most Probable Value) about 72 $e-h/\mu m$. In a sensor with an active thickness of 45 μm, the expected charge for protons in the aforementioned energy

range will vary from 2.57 fC to 1.04 fC. From the Eq. 1.8, it can be noted that the energy losses depend not only on the atomic number of the absorbing material (Z), but also on the charge of the projectile (z). Since this is a direct square dependence, the energy loss for higher z ions increases substantially, as can be seen for protons and carbon ions impinging on a silicon target at the same speed (Fig. 1.5). In this case, the energy loss of carbon ions of 200 MeV/u is greater by a factor of 36 than that of protons with the same energy per nucleon (see in Fig. 1.5 the data tip for 200 MeV/u). Taking that into consideration, the typical clinical energy used for carbon ions for example at National Centre for Oncological Hadrontherapy (CNAO, Pavia, Italy) is between 115.23 MeV/u and 398.84 MeV/u, which is equivalent to 114 MIP and 54 MIP, respectively. Therefore, the expected signal in a silicon sensor with an active thickness of 45 μm, is between 28 fC and 60 fC for 398.84 MeV/u and 115.23 MeV/u, respectively.

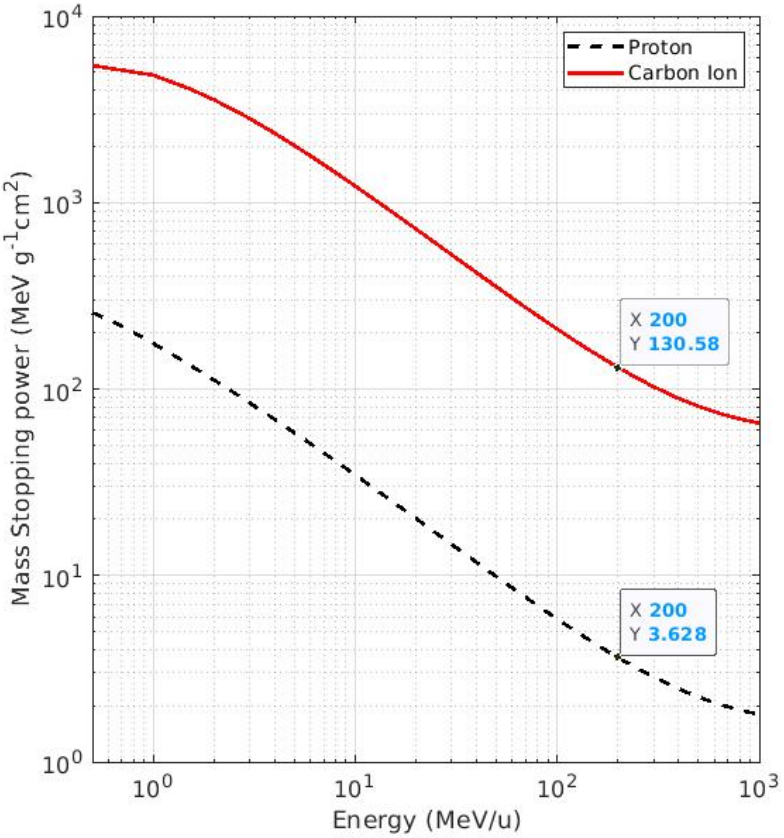

FIGURE 1.5: Mass stopping power as a function of energy for carbon ion and proton impinging on a silicon target.

It is important to point out that the Bethe Bloch formula calculates the mean amount of energy lost due to ionization and excitation per unit of distance,

which are a statistical phenomena. For that cause, the energy loss (Δ) given by equation 1.8 fluctuates in each projectile interaction with the atomic electrons. Accordingly, the energy loss by the incoming particle follows an energy distribution, the so-called energy-loss distribution or energy straggling function, $f(x,\Delta)$, which is the solution of the integral transport equation.

$$\frac{\partial f(x,\Delta)}{\partial x} = \int_0^\infty \omega(\epsilon)[f(x,\Delta-\epsilon) - f(x,\Delta)]d\epsilon \tag{1.9}$$

where:
$\omega(\epsilon)d\epsilon$: is the probability per unit path length of a collision transferring energy (ϵ) to an electron in the material.
Several authors solved equation 1.9 in which the most remarkable solutions were found by Landau and Vavilov (Landau (Landau, 1944), Vavilov (Vavilov, 1957)). Landau (Landau, 1944) solved the equation 1.9 by a method based on Laplace transform using the free electron (Rutherford) cross section ($\omega(\epsilon) = \frac{\xi}{x}\frac{1}{\epsilon^2}$) for thin absorbers $(\xi/W_m) << 1$ $(W_m \to \infty)$, in which (ξ) is express as:

$$\xi = 0.1535x\frac{\rho z^2 Z}{A\beta^2} \tag{1.10}$$

For the case of silicon, the equation 1.10 can be rewritten as:

$$\xi = \frac{1.78}{\beta^2}\cdot 10^{-2} keV/\mu m \tag{1.11}$$

Therefore, the Landau distribution $f_L(x,\Delta)$ as a solution of equation 1.9 is:

$$f_L(x,\Delta) = \frac{\phi(\lambda)}{\xi} \tag{1.12}$$

where $\phi(\lambda)$ is a function of the parameter λ, and is expressed as:

$$\phi(\lambda) = \frac{1}{\pi}\int_0^\infty e^{(-\pi u/2)} cos[u(\ln(u)+\lambda)]du \tag{1.13}$$

with λ equal to

$$\lambda = \frac{\Delta - <\Delta>}{\xi} - \beta^2 - \ln(\xi/W_m) - 1 + C_E \tag{1.14}$$

where:
C_E is the euler constant.
$f_L(x,\Delta)$ has a maximum for λ =-0.229 and a Full Width Half Maximum $(FWHM)$ equal to 4.02ξ. The maximum of the landau distribution is called Most Probable Value (MPV) and it corresponds to the most probable energy loss (ϵ_{MPV}). This distribution is asymmetric with not negligible tail due to fast emitted $\delta - rays$ located to the right of ϵ_{MPV}.
The solution found by Vavilov $f_V(x,\Delta)$ (Vavilov, 1957) for equation 1.9 which tends to the Landau distribution for $(\xi/W_m) \leq 0.06$ (the region where $\Delta \approx \xi$) was based on taking into account the spin of the incoming particle. For that reason, for thin absorbers, the energy loss distribution is called Landau-Vavilov distribution, and the notation usually used is $f_{L,V}(x,\Delta)$ Then, for the collision cross-section the following expression was used:

$$\omega(\epsilon) = \frac{\xi}{x}\frac{1}{\epsilon^2}(1 - \frac{\beta^2\epsilon}{W_m}) \tag{1.15}$$

In addition, the Landau solution for thick absorbers $(\xi/W_m) >> 1$), turns into a Gaussian distribution. In the same way, the Vavilov distribution for thick absorbers also becomes almost a Gaussian function:

$$f_V(x,\Delta) = \frac{1}{\sqrt{\frac{2\pi W_m}{\xi}(1-\frac{\beta^2}{2})}} exp[-\frac{(\Delta - <\Delta>)^2}{2W_m\xi(1-\frac{\beta^2}{2})}] \tag{1.16}$$

with σ_V equal to

$$\sigma_V = \sqrt{\xi W_m(1-\frac{\beta^2}{2})} \tag{1.17}$$

The MPV for $f_{L,V}(x,\Delta)$ can be calculated using the equation 1.14 as:

$$\Delta = <\Delta> + \xi[\lambda + \beta^2 + \ln(\xi/W_m) + 1 - C_E] \tag{1.18}$$

Substituting the values of: $\lambda = -0.229$, $C_E = 0.577215$ in equation 1.18 we obtain:

$$\Delta = <\Delta> + \xi[\beta^2 + \ln(\xi/W_m) + 0.194][MeV] \tag{1.19}$$

Finally, in thin absorbers, such as silicon detectors, for example, with a thickness of a few hundred micrometers or less, deviations from the Landau-Vavilov energy straggling distribution and the experimental data were observed. The difference was attributed to the assumption that distant collisions were neglected in the Landau-Vavilov theories for thin absorbers. The solution for equation 1.19 was derived under the assumption that scattering occurs on quasi-free electrons and follows the Rutherford collision probability, neglecting the electron binding energies. For that reason, $f_{L,V}$ was improved by modifying the cross-section to consider the electron binding energy, finally obtaining:

$$f(x,\Delta) = \frac{1}{\sqrt{2\pi\delta_2}} \int_{-\infty}^{+\infty} f_{L,V}(x,\Delta-\tau) e^{-\frac{\tau^2}{2\delta_2}} d\tau \tag{1.20}$$

where δ_2 is the variance of the Gaussian convolving distribution, and can be calculated as:

$$\delta_2 = \frac{8}{3}\frac{\xi}{x} \sum_{i=1} I_i f_i \ln \frac{2m_e c^2 \beta^2}{I_i} \tag{1.21}$$

where I_i is the effective ionization potential of the $i-th$ shell and f_i is the fraction of electrons in that shell.
The equation 1.20, it is known as the Langaus distribution. It is the convolution between the Landau and the Gaussian distribution in which the MPV no longer corresponds to the maximum of the curve. This is because the Landau function is asymmetric and, when it is convoluted with a symmetric (Gaussian) function, the net result is a slight shift of the distribution peak to a larger value (≈3 %). From now on, equation 1.20, when used, will refer as the Langaus.
While the stopping power is a quantity representing the differential amount of energy lost as a function of distance, the range of the particle describes how far the particle goes using the continuous slowing down approximation (CSDA), and it is obtained as follows:

$$R_{CSDA} \approx \int_0^{E_{ki}} \frac{dE}{\frac{dE}{dx}} \propto E^{\sim 2} \tag{1.22}$$

Where, E_{ki} is the initial kinetic energy. The energy transferred to tissue by a heavy charge particle (projectile) is inversely proportional to the incoming particle velocity once loses its energy mainly by electromagnetic interactions

with orbital electrons of atoms, as explained previously. Therefore, as the projectile slows down, the energy transfer to the tissue per track length is higher. This effect causes a maximum dose deposition at a certain depth in tissue. It is known as the Bragg peak (see Fig. 1.6). For example, for a single proton, this peak is very sharp. Instead for a proton beam, it is broadened into a peak of typically a few millimeters width due to the statistical distribution of the proton tracks. The depth and width of the Bragg peak are a function of the beam energy and the material (tissue) heterogeneity in the beam path. The peak depth can be influenced by changing the beam energy and can thus be positioned within the target for each beam direction (Paganetti, 2018).

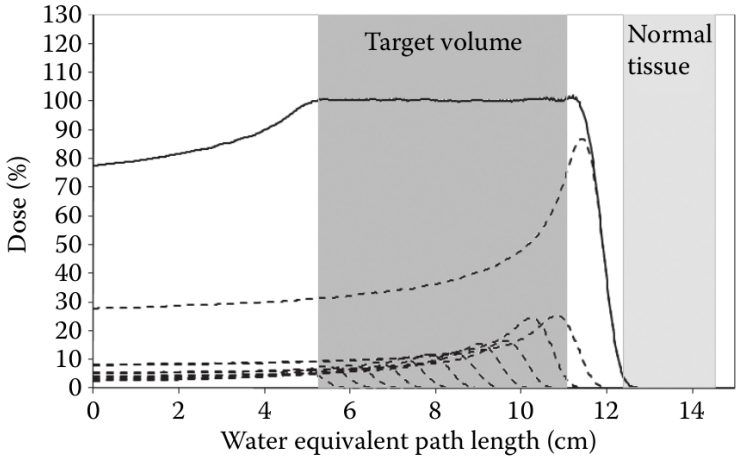

FIGURE 1.6: A schematic view of spread-out Bragg peaks (SOBP) construction, showing the SOBP depth–dose distribution (solid line) and the component Bragg peaks (dashed lines). Picture taken from (Paganetti, 2018).

The quantity of equation 1.22 is directly proportional to almost the square of the incoming particle's kinetic energy. It is a physical quantity widely used in hadrontherapy that allows treating tumors at different depths. For example, using the data from (Tommasino et al., 2017) for the range at 90% ($R_{90}(g/cm^2)$) of the distal fall-off of the Bragg curve, shown that for the effective energy at the isocenter of 68.5, 72.4, 104.2, 136.1, 222.9, and 227.4 MeV, the R_{90} is equal to 3.9, 4.3, 8.3, 13.3, 31.2, and 32.3, respectively. Therefore, the beam's energy needs to be precisely modulated and controlled to treat tumors once its range depends upon its energy. A technique used for treating tumors is by a superposition of many Bragg peaks with appropriate intensity and locations, the so-called spread-out Bragg peaks (SOBP), as shown in Fig. 1.2a and Fig. 1.6. Two methods are widely extended to produce the SOBP.

They are either by inserting materials in the beam path to modify the beam energy or by modifying the energy coming from the accelerator.

Interaction of light charge particle with matter

In the case of light charged particles (electrons and positrons), the total stopping power is customarily separated into two main components: the collision stopping power and the radiative stopping power, as shown in Eq. 1.23 (Cross et al., 1997). Electrons (also positrons) penetrating in matter primary loss energy due to inelastic Coulomb collisions with bound atomic electrons resulting in the excitation and ionization of orbital electrons, as mentioned before for the heavy charged particles. Considering that the collision is between two identical particles, the maximum energy transfer in a single collision is the half of the entire kinetic energy. Therefore, for electrons the energy transferred per collision can be large that's why they are strongly deflected from their original course and do not follow a straight path inside the material (Patrignani, 2016).

$$\frac{dE}{dx}_{total} = \frac{dE}{dx}_{collision} + \frac{dE}{dx}_{radiative} \tag{1.23}$$

The first term of equation 1.23 corresponds to the collision stopping power and can be calculated using the theory developed by Møller (Møller, 1932; Uehling, 1954). In the relativistic region, the equation can be written as follows (Patrignani, 2016):

$$-\frac{dE}{dx}_{collision} = K(\ln[\frac{m_e c^2 \beta^2 \gamma^2 (m_e c^2(\gamma-1)/2)}{I^2}] + B) \tag{1.24}$$

where: $K = \frac{4\pi N_A m_e c^2 r_e^2 Z}{2A\beta^2}$ and $B = (1-\beta^2) - \frac{2\gamma-1}{\gamma^2}\ln 2 + \frac{1}{8}(\frac{\gamma-1}{\gamma})^2 - \delta$
In addition to the collision-related energy loss, there is an energy loss due to radiation emission (Bremsstrahlung) when the electron is accelerated in the Coulomb field of a nucleus. The average energy loss due to radiation emission is given by the Bethe-Heitler formula (see Eq. 1.25,(Bethe and Heitler, 1934)) in the region between $mc^2 << E << 137mc^2 Z^{-\frac{1}{3}}$, showing that the energy loss increases quadratically with increasing atomic number (Z):

$$-\frac{dE}{dx}_{radiative} = \frac{NEZ^2 e^4}{137(mc^2)^2}(4\ln(\frac{2E}{mc^2}) - 4/3) \tag{1.25}$$

where:
Z: is the atomic number of the target
N: is the number of atoms per cm^3
From this equation, it can be noticed that the Bremsstrahlung yield is inversely proportional to the square of the particle's mass (m), so for heavy particles this effect is almost negligible for lower energies. The other conclusion is that for relatively small energies, the loss is independent of the kinetic energy of the incident electron, while for large energies, it increases proportionally to (E). In the case of collision stopping power, the loss decreases sharply for lower energy and begins to slowly increase with increasing energy. The behavior of both energy loss mechanisms can be appreciated in Fig. 1.7, which shows the energy loss of electrons in silicon, where for energies greater than 48 MeV energy loss by radiation becomes the dominant process. This value corresponds to the so-called critical energy defined as the energy value at which collision energy loss equals Bremsstrahlung loss. (Patrignani, 2016; Bethe and Heitler, 1934).

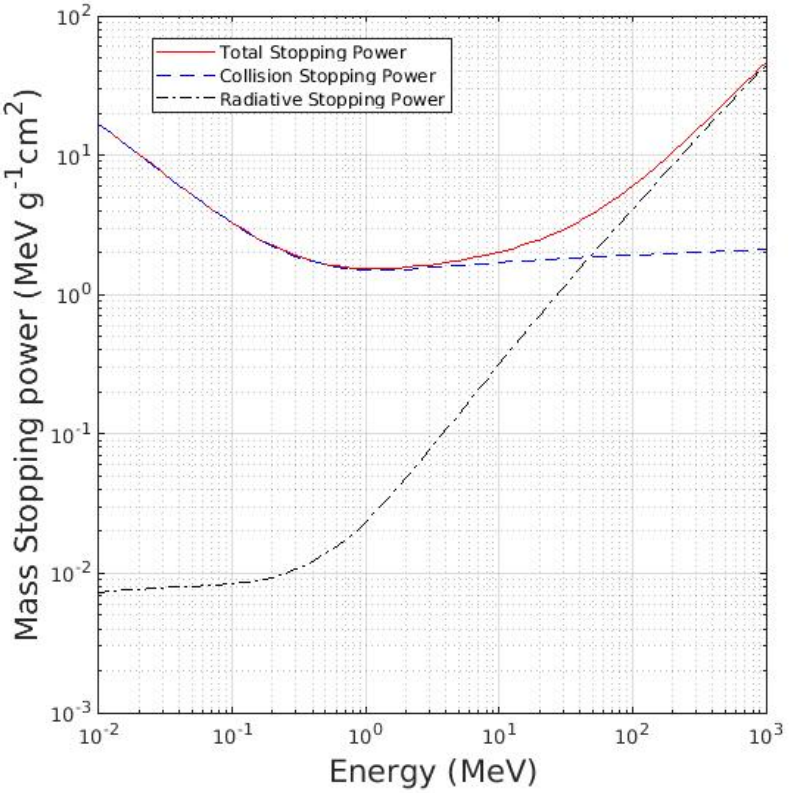

FIGURE 1.7: Mass stopping power as a function of energy for electrons impinging on a silicon target.

1.2.2 Basic principles of the semiconductor physics

This thesis focuses on testing thin silicon sensors for beam monitoring in particle and FLASH radiotherapy. Therefore, in this section, the basic physics of the semiconductor sensor and the operating principles of the silicon detectors will be presented, along with a brief introduction to the PiN and LGAD sensors.

The insulators have a very low conductivity, on the order of 10^{-18} to 10^{-8} S/cm. The metals have a conductivity of more or less between 10^{3} to 10^{8}. Semiconductors are a class of materials with conductivity between metals and insulators. They are divided into two classes: the elemental semiconductors materials, which are located in group IV of the periodic table, such as Carbon, Silicon, and Germanium, and the other class, the compound semiconductor materials, most of which are formed by a particular combination of elements from group III and group V. Examples of compound semiconductors are Gallium Arsenide, Gallium Phosphide, Aluminum Arsenide, and others (Sze, 2008). It is essential to point out that compound semiconductors can also be formed from combinations of elements of group II and group VI but are less common. The conductivity of a semiconductor is generally susceptible to temperature, illumination, magnetic field, and minute amounts of impurity atoms (doping) (Sze, 2008). This variability, upon several conditions, makes a semiconductor one of the most important materials for electronic applications.

In the middle of the last century, Germanium was the major semiconductor material. However, since early 1960, silicon started to substitute Germanium as a semiconductor material in many applications due to economic considerations, and due to the silicon exhibiting better properties at room temperature. Consequently, silicon technology is by far the most advanced among all semiconductor technologies worldwide.

Silicon has a diamond lattice arrangement characterized by an energy band structure in which each atom has four electrons in the outer orbit, and each atom shares these valence electrons with its four neighbors. More details about the formation of energy band structure for a diamond lattice crystal from N isolated atoms can be observed in Fig. 1.8. The x-axis refers to the spacing between the atoms or lattice spacing, and E in the y-axis refers to the Electron energy. In Figure 1.8 is not shown the core (n=1 and n=2) levels once they are completely full and are tightly bound to the nucleus. As can be appreciated, decreasing the lattice spacing makes the 3s and 3p subshells

of the N silicon crystal interact and overlap to form bands that contain 8 N states. At the equilibrium interatomic distance, which is in silicon 5.43 A, the bands will again separate, with 4 N states in the lower (Valence) and upper (Conduction) bands, respectively.

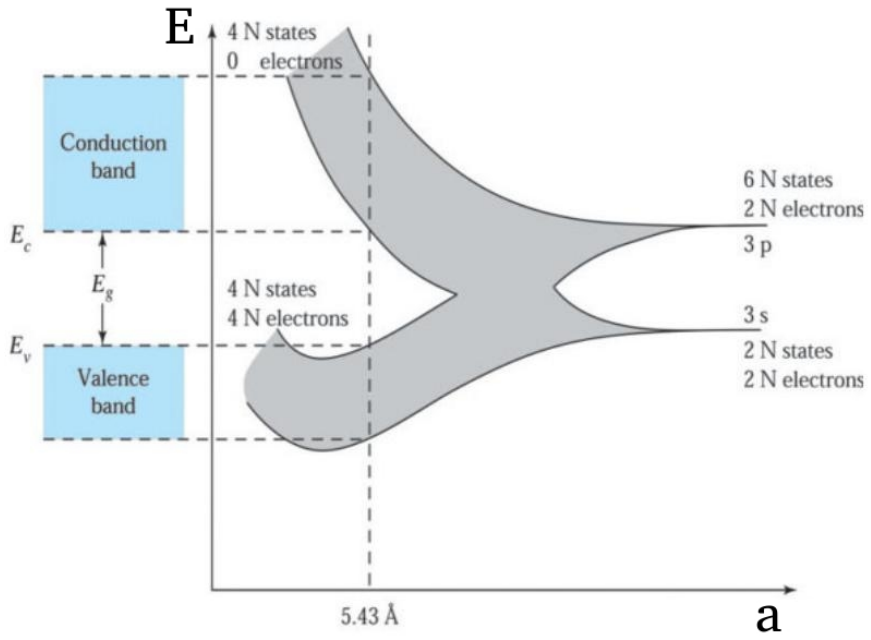

FIGURE 1.8: Formation of energy bands as a diamond lattice crystal is formed by bringing isolated silicon atoms together. Picture taken from (Sze, 2008).

At T=0 K, electrons are in the valence band (E_V), therefore fully occupied, and the conduction band (E_C) is completely empty. The separation between these two bands ($E_C - E_V$) is the bandgap energy (E_g) which is the width of the so-called forbidden energy band. By increasing the temperature, there is a certain probability that a fraction of the electrons from the valence band are excited to the conduction band. In a semiconductor, the forbidden gap is small enough that at room temperature, the fraction of thermally excited electrons into the conduction band is not negligible. For insulator material, the forbidden gap is large compared to semiconductor $E_g > 5eV$, then at room temperature, the fraction of electrons that are thermally excited from the valence band to the conduction band is tiny (Betta, 2019). In the other hand, in the metals the valence and conduction band are in contact.
Silicon is largely used nowadays as a radiation detector. Given the small energy gap, a small energy deposition can move electrons from the valence band to the conduction band, leaving behind a positive charge vacancy, called

hole. Under the influence of the electric field in the depletion region, the two charge carriers (electron and hole) drift in different directions, inducing a signal in the readout electrode. Consequently, the passage of an ionizing particle can be detected by collecting the charge carriers released by energy deposition in the silicon.

An intrinsic semiconductor, or pure semiconductor, contains negligible impurities. In thermal equilibrium, electrons in the conduction band only originate from thermal excitation from the valence band. For that reason, the concentration of electrons and holes is equal. Therefore, the probability that an electron occupies an energy states follows the Fermi-Dirac statistical distribution (Sze, 2008)

$$f_e(E) = \frac{1}{e^{(E-E_F)/k_BT} + 1} \tag{1.26}$$

where: E_F is energy of the Fermi level, k_B is the Boltzmann's constant, and T is the temperature. The Fermi level is the energy at which the probability of occupation by an electron is exactly 0.5. Assuming that the Fermi energy is within the forbidden bandgap, and for electrons in the conduction band, $E > E_C$. Then, for the non-degenerate case ($E_C - E_F >> k_BT$), consequently $(E - E_F) >> k_BT$, the Eq. 1.26 reduces to the following:

$$f_e(E) \approx e^{\frac{-(E-E_F)}{k_BT}} \tag{1.27}$$

The density of electrons in the conduction band at thermal equilibrium for the non-degenerate case can be found by integrating Eq. 1.28 over the conduction band energy:

$$n_0 = \int_{E_C}^{E_\infty} (\frac{4\pi(2m_n^*)^{3/2}}{h^3}\sqrt{E - E_C})e^{\frac{-(E-E_F)}{k_BT}}dE \tag{1.28}$$

where: E_C is the energy at the bottom of the conduction band. The quantity inside the parenthesis is the density of quantum states in the conduction band, instead the outside terms are the Fermi-Dirac probability for the non-degenerate case as shown in Eq. 1.27. The solution of Eq. 1.28 is:

$$n_0 = (2(\frac{2\pi m_n^* k_B T}{h^2})^{3/2} e^{\frac{-(E_C-E_F)}{k_BT}} \tag{1.29}$$

where: $(2(\frac{2\pi m_n^* k_B T}{h^2})^{3/2}$ is the effective density of states in the conduction band, and is normally refers as N_C. The parameter m_n^* is the effective mass of the electron. Usually, Eq. 1.29 is express as:

$$n_0 = N_C e^{\frac{-(E_C - E_F)}{k_B T}} = n_i e^{\frac{-(E_F - E_{Fi})}{k_B T}} \tag{1.30}$$

In the same way, the density of holes in the valence band at thermal equilibrium for the non-degenerate case is given by:

$$p_0 = N_V e^{\frac{-(E_F - E_V)}{k_B T}} = n_i e^{\frac{-(E_{Fi} - E_F)}{k_B T}} \tag{1.31}$$

where: N_V is called the effective density of states in the valence band.
For ideally pure semiconductors, the concentration of electrons in the conduction band is the same as the concentration of holes in the valence band, then $n_0 = p_0 = n_i$. In which n_i is the intrinsic carrier concentration and refers to either the intrinsic electron or hole concentration. The Fermi energy level for the intrinsic semiconductor is called the intrinsic Fermi energy (E_{Fi}) (Neamen, 2003). Therefore, applying equations 1.30 and 1.31 for the intrinsic semiconductors, we obtain:

$$n_0 = n_i = N_C e^{\frac{-(E_C - E_{Fi})}{k_B T}} \tag{1.32}$$

and

$$p_0 = n_i = N_V e^{\frac{-(E_{Fi} - E_V)}{k_B T}} \tag{1.33}$$

where: E_V is the value of energy at the top of the valence band. By multiplying Eq. 1.32 and 1.33, an important relation is obtained:

$$n_i^2 = N_C N_V e^{\frac{-(E_C - E_V)}{k_B T}} \tag{1.34}$$

where: $E_C - E_V$ is the bandgap energy E_g, which for Silicon is equal to 1.12 eV, so the intrinsic concentration for this material at room temperature (300K) is $n_i = 1.45x10^{10} cm^{-3}$ (Spieler, 2005). The Fermi level position for intrinsic semiconductor is obtained by equating the Eqs. 1.32 and 1.33:

$$E_{Fi} = \frac{1}{2}(E_C + E_V) + \frac{3}{4} k_B T Ln(\frac{m_p^*}{m_n^*}) \tag{1.35}$$

where: m_p^* is the effective mass of the hole. The Eq. 1.35 establish that the Fermi level position is slightly below the center of the bandgap once the electron and hole effective masses are different. In silicon, the Fermi level is 12.8 meV below the midgap energy (560 meV).

In the extrinsic semiconductor, the conductivity is modified by adding a small and controlled amount of impurity. When is added to the silicon lattice a group V element, such as phosphorous (P), as a substitutional impurity, four of the valence electrons will contribute to the covalent bonding with the silicon atoms. The fifth valence electron, lightly bound to the impurity atom, is left without a partner. Therefore is called a donor once it contributes an excess of electrons to the lattice. The donor electron is bound to the P atom at very low temperatures. However, the energy required to elevate the donor electron into the conduction band (leaving behind a positively charged P ion) is smaller than for the electrons involved in the covalent bonding. The electron in the conduction band can now move through the crystal generating a current, while the positively charged ion is fixed in the crystal. The donor impurity atoms add electrons to the conduction band without creating holes in the valence band. The resulting material is referred to as an n-type semiconductor.

In the case of adding to the silicon lattice, a group III element, such as boron (B), it provides bonds for all Si valence electrons but leaves one impurity valence electron without a partner. Therefore, one covalent bonding position is left empty and can be occupied by valence electrons, which need an energy smaller than the necessary energy to be in the conduction band to fill the vacant position. Therefore, the group III atom accepts an electron from the valence band and is referred to as an acceptor. The acceptor atom can generate holes in the valence band without generating electrons in the conduction band. This type of semiconductor is known as a p-type material.

In summary, if the position of the energy level of the donor/acceptor (E_D/E_A) is very close to (E_C/E_V), then the donor/acceptor can be very easily ionized at room temperature by the thermal energy.

For the case of n-type material in which the concentration of donor (N_D) added to the silicon lattice is larger compared to n_i, the position of the Fermi Energy level can be easily derived assuming the Boltzmann approximation and using the Eq. 1.30.

$$E_F = E_C - k_B T Ln(\frac{N_C}{N_D}) \tag{1.36}$$

On the other hand, for the case of p-type material in which the concentration of acceptor (N_A) added to the silicon lattice is larger compared to n_i, the position of the Fermi Energy level can be easily derived assuming the Boltzmann approximation and using the Eq. 1.31.

$$E_F = E_V + k_B T Ln(\frac{N_V}{N_A}) \tag{1.37}$$

The charge transport mechanism in a semiconductor is governed by two phenomena, diffusion and drift. The diffusion is given by a gradient in the carrier's concentration. Instead, the drift is how the carriers react to an electric field. Then, the drift current density for both, electron and holes, can be written as:

$$J_{drift} = e(\mu_n n + \mu_p p)E \tag{1.38}$$

where: μ_n and μ_p is the mobility for electron and holes, respectively. It is an indicator of how well the carriers move into a semiconductor as a result of the force of an electric field. The diffusion for both carriers is given by:

$$J_{diff} = e(D_n \frac{\partial n}{\partial x} - D_p \frac{\partial p}{\partial x}) \tag{1.39}$$

where: $D_{n,p}$ is the Einstein diffusion coefficients.
There are several golden rules that can be applied to the energy-band diagram in order to understand whether the drift and diffusion current density are equal or/and different from 0. For instance, rule number one states that whenever exist a slope in the E_C, E_V, and E_{Fi}, then the drift current density is different from 0. The second rule stipulates whenever is observed a gradient in the energy band, for example, $\frac{\partial(E_F - E_C)}{\partial x}$, $\frac{\partial(E_V - E_F)}{\partial x}$ different from 0, therefore the diffusion current density is different from 0. Finally, if the Fermi level is constant, then the total current density is 0, and viceversa, this establishes the last golden rule.

p-n junction

A p-n junction is formed at the interface of a p- and an n-type region as shown in Fig. 1.9a. Because the concentration of electrons in the n-region is greater than in the p-region, there is a gradient in the carrier's concentration. Therefore, the electrons will diffuse into the p-region. Correspondingly, in the p-region there is a concentration of holes greater than in the n-region, then the holes will diffuse into the n-region. As electrons and holes diffuse across the

junction, a space charge due to the ionized donor and acceptor atoms builds up. The field due to this space charge is directed to impede the flow of electrons and holes. The gradient concentration causes a continuous diffusion current to flow, whereas the field due to the space charge drives a drift current in the opposite direction. Equilibrium is attained when the two currents are equal, i.e., the sum of the diffusion and drift currents is zero. The net hole current density is expressed as follow:

$$J_p = -q_e D_p \frac{\partial p}{\partial x} + q_e p \mu_p E_p \tag{1.40}$$

where: D_p is the diffusion constant for holes and E_p is the electric field in the p-region. Using the Einstein relationship, which relates the mobility to the diffusion constant and substituting the derivative of Eq. 1.31 in Eq. 1.40 and since the force on a charge q_e due to an electric field E is equal to the negative gradient of the potential energy (Spieler, 2005):

$$q_e E = -\frac{\partial E_C}{\partial x} = -\frac{\partial E_V}{\partial x} = -\frac{\partial E_{Fi}}{\partial x} \tag{1.41}$$

The three: E_C, E_V, and E_{Fi} only differ by a constant offset, and once only the gradient is of interest, as observed in Eq. 1.41, it was used the intrinsic Fermi level since it applies throughout the sample. Therefore, we obtain for the net hole current, the following:

$$J_p = -q_e p \frac{D_p}{k_B T} \frac{dE_F}{dx} = \mu_p p \frac{dE_F}{dx} \tag{1.42}$$

Similarly, for the net electron current:

$$J_n = -q_e n \frac{D_n}{k_B T} \frac{dE_F}{dx} = -\mu_n n \frac{dE_F}{dx} \tag{1.43}$$

Since each of the net hole and electron currents in equilibrium must be zero, the derivative of the Fermi level in the previous equation is zero. In thermal equilibrium the Fermi level must be constant throughout the junction region as observed in Fig. 1.9b. As appreciated, on the p-side the Fermi level is near to the valence band, and on the n-side it is near to the conduction band.
Considering that on the n-side, the dopant is only donors, and on the p-side,

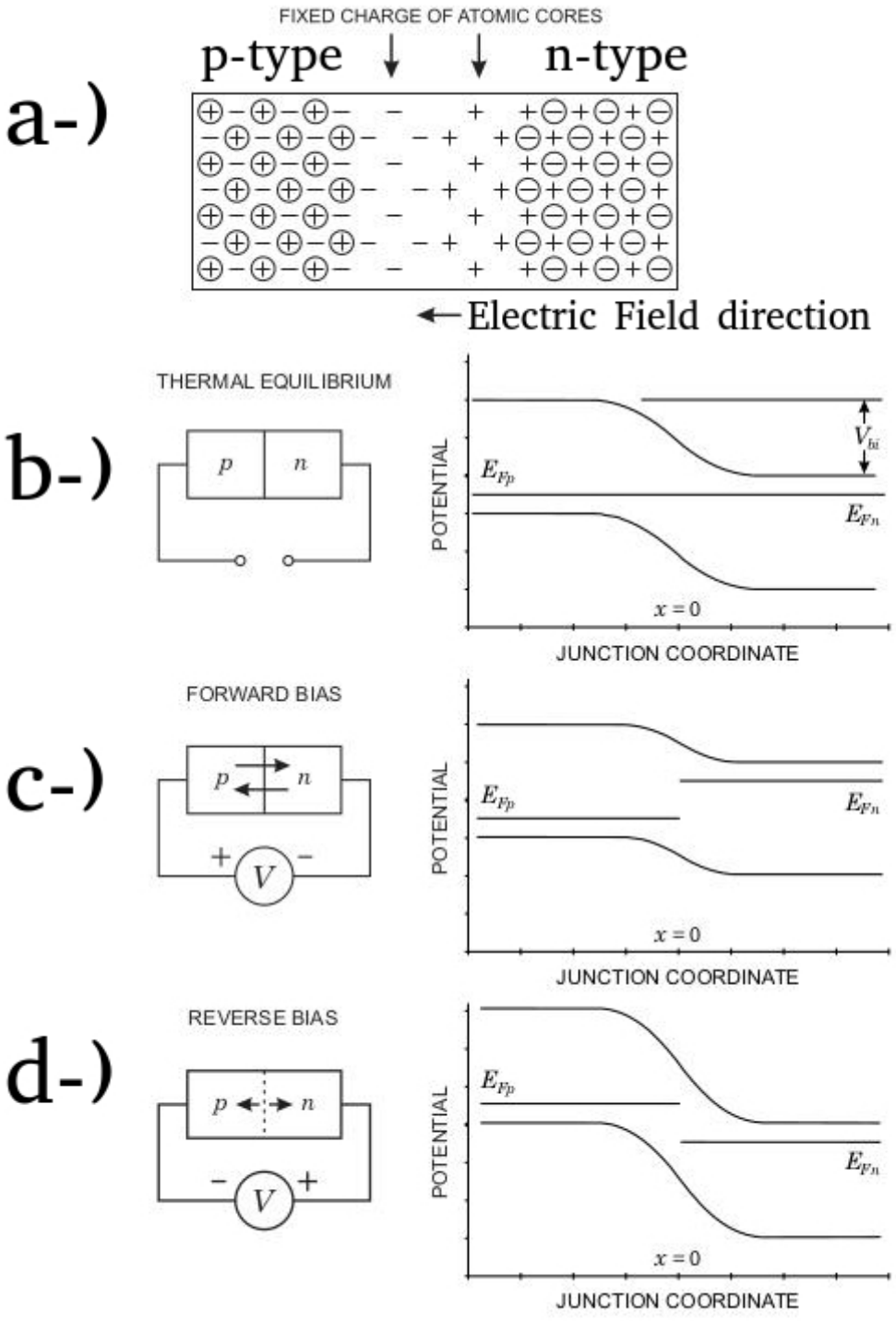

FIGURE 1.9: (a) Diffusion of electrons and holes across the junction forms a depletion zone with a resulting potential between the p- and n-regions. (b) In a p-n junction at thermal equilibrium the valence and conduction bands bend so that the Fermi level is constant throughout the device. (c) Applying forward bias lowers the potential difference and increases the flow of electrons and holes across the junction. (d) Reverse bias raises the potential barrier, which reduces the electron and hole concentrations at the p-n junction and widens the depletion region. Pictures adapted from (Spieler, 2005).

only the dopant are acceptors, the difference in the respective Fermi levels is

$$\Delta E_F = -k_B T Ln \frac{N_A N_D}{n_i^2} \tag{1.44}$$

which correspond to an electric potential, the so called built-in voltage (V_{bi}):

$$\Delta V_F = V_{bi} = \Delta E_F / q_e = -\frac{k_B T}{q_e} Ln \frac{N_A N_D}{n_i^2} \tag{1.45}$$

The built-in voltage depends logarithmically on the doping level, where N_A and N_D are the acceptor and donor concentrations, and n_i is the intrinsic carrier concentration. When a bias voltage (non-equilibrium conditions) with a positive potential is applied to the p-region and a negative to the n-region, the potential barrier is reduced (see Fig. 1.9c). This will cause an increase in the flow of electrons and holes across the junction. This case is known as forward bias. In the other case, the opposite polarity is applied in both regions, causing an increase in the potential barrier and provoking the width of the depletion region to grow. This case is known as reverse bias, as shown in Fig. 1.9d.
The total current density in the p-n junction can be expressed as:

$$J = [\frac{eD_p p_{n_0}}{L_p} - \frac{qD_n n_{p_0}}{L_n}](e^{\frac{eV}{k_B T}} - 1) \tag{1.46}$$

Also the Eq. 1.46 can be defined like:

$$J = J_0(e^{\frac{eV}{k_B T}} - 1) \tag{1.47}$$

where:

$$J_0 = [\frac{eD_p p_{n_0}}{L_p} - \frac{qD_n n_{p_0}}{L_n}] \tag{1.48}$$

and, knowing that:
e : is the elementary charge
D_p / D_n : is the diffusion coefficients of holes and electrons, respectively
L_p / L_n : are the diffusion length of holes and electrons, respectively
p_{n_0} : is the thermal equilibrium minority carrier hole concentration in the n-side
n_{n_0} : is the thermal equilibrium minority carrier electrons concentration in the p-side

The equation 1.46 was obtained under the assumption that the depletion region is transparent, which means that charges do not recombine or get trapped within it (because the strong electric field is quickly drifting them from one side to the other). Also was assumed that we are working with a low injection regime, a complete ionization and an abrupt depletion layer.
Eq. 1.46, called Diode Law, represents the ideal current density-voltage in a p-n junction. For forward bias voltage (V), the exponential term dominates and the current increases rapidly with voltage. It can be noticed that when the values of V become negative (reverse bias), the exponential term reaches values close to zero. Once it is negligible $(e^{\frac{eV}{k_B T}} << 1)$ the reverse biased current density becomes independent of the reverse-biased voltage and the value of J reach $-J_0$. This parameter is known as the reverse-saturation of the current density. J can be multiplied by the area (A) of the device and obtain the current (I) instead of its density:

$$I = I_0(e^{\frac{eV}{k_B T}} - 1) \tag{1.49}$$

where: I_0 is the reverse bias saturation current.
At very high reverse bias voltage, however, the device's behavior differs from the Diode law and enters in the multiplication region. In this condition, the electric field is so high that a carrier entering the depletion region can gain enough energy to generate other charge couples mainly by impact ionization. It is known as junction breakdown and it is characterize by overexponential increase of the current of the device.
For radiation detectors, as in the case of this thesis, it only uses the device in reverse bias. Since the depletion region is a volume devoid of mobile carriers, it forms a capacitor. The undepleted p- and n-regions are the electrodes, and the depletion region is the dielectric. The electric field in the depletion region will sweep mobile carriers to the electrodes, inducing a signal.

Operating principles of a silicon detector

The silicon sensor's operating principle is depicted in Fig. 1.10. Basically, in a planar n-on-p sensor, reverse biased by an external source, a large depleted volume is created which is the sensitive part of the detector. The sensors used in this research aim to detect charged particles such as protons, electrons, and carbon ions. As explained in section 1.2.1, a charged particle creates electron-hole (e-h) pairs along its path when it crosses the active area of the sensor. The number of $(e - h)$ created depends on the thickness of the sensor. In

a conventional detector of 50 μm, protons of 62 MeV will generate approximately $1.8x10^4$ e-h pairs, which corresponds to a charge of 2.85 fC.
Under the influence of the electric field, the electrons move towards the n^{++} electrode and the holes to the opposite contact, the p^{++}, creating as fast they start to move an induced current on the electrodes. The time that takes the $(e-h)$ pairs to be completely collected in their respective electrode depends on the electric field inside the detector's active area. For a PiN sensor with a resistivity of 25 kΩcm, an active thickness of 50 μm, and a reverse bias voltage of 200 V, the electron and hole collection times are about 0.5 ns 0.75 ns, respectively.
The signal induced can be calculated using Ramo-Shockley's theorem (Shockley, 1938; Ramo, 1939), which states that the current induced by charge carriers is proportional to its electric charge, the drift velocity, and the weighting field E_w, as shown in Eq. 1.50.

$$i(t) = -q\vec{v}\vec{E}_w \tag{1.50}$$

In the design of a detector, the drift velocity must be constant throughout the active volume. The most straightforward method to obtain it is to have an electric field high enough everywhere in the active volume of the sensor, allowing the carriers always move with saturated drift velocity. Non-uniform drift velocity induces variations in signal shape as a function of the hit position, spoiling the overall time resolution.

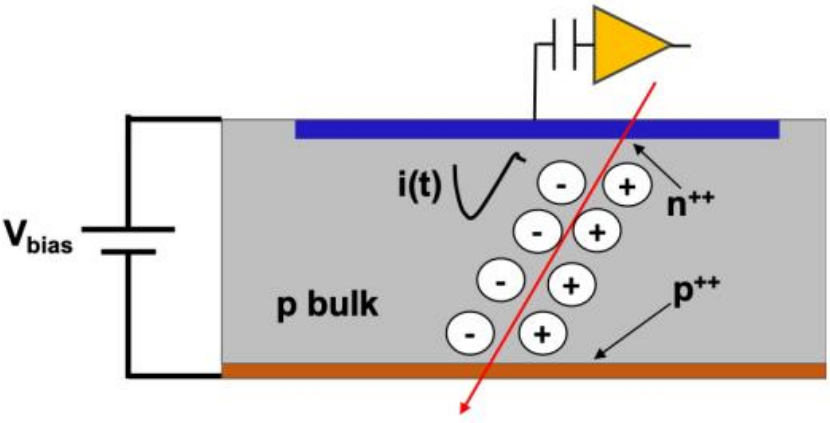

FIGURE 1.10: Scheme of the basic operational principles of a silicon detector. Picture taken from (Ferrero et al., 2021).

The weighting field, representing the capacitive coupling of a charge e to the read-out electrode, should not vary along the electrode pitch, if this coupling depended on the impinging particle position along the implant pitch, the

signal shape would be different depending on the hit position, spoiling the time resolution as well. In a detector segmented in strips, as in our case, the signal will be unipolar on the collection electrode and bipolar on the others. The reason for the bipolar signal shape is a consequence of the change in the direction of the weighting field along the path from the read-out strip to the farthest neighbor strip.

The current induced by the incident charged particle, which is at the end an electrical signal, will be followed by the front-end electronics. The first step of the front-end electronics is the pre-amplification stage, where trans-impedance amplifiers are usually used to extract the current signal from the detector and convert it to a voltage signal. It can be designed to pre-amplify the signal, with the low contribution of noise and distortion, and provide an input impedance such that the current signal can be extracted from the sensor and used as an input for the other steps. After the first stage, additional stages can be used to further amplify and shape the voltage signal to a level that can be used in the discriminator to count the particle.

The gain of the avalanche process is defined as the ratio between the total number of $e - h$ pairs collected with/without multiplication, and it is usually about 10 in LGAD that are used for charge particle application. In a PiN sensor, as shown in 1.11a, theoretically, one can increase the electric field to a high value by simply applying a high external reverse bias voltage until it reaches an electric field higher than 300 kV/cm, triggering the avalanche process. This is not a viable solution once the detector is susceptible to a breakdown due to a very high electric field on the device's periphery (Ferrero et al., 2021). Conversely, in the LGAD design, the electric field value of about 300 kV/cm is obtained in a very localized region by depleting an additional p^+ doped layer implanted near the p-n junction. This additional layer, which is implanted at a depth of about 0.5-2 μm, has an acceptor doping concentration of about 10^{16} $atoms/cm^3$ (Ferrero et al., 2021). When depleted, that layer generates an electric field high enough to activate the avalanche process. In this thesis, LGAD sensors were used for application with protons since the signal generated by a proton in the clinical energy range has a small amplitude in a thin PiN detector, not allowing noise separation. Therefore, those detectors are not suitable for counting and timing applications in proton therapy.

PiN and LGAD sensors

In this thesis, either was tested Low Gain Avalanche Detector (LGAD) and PiN sensors. It is crucial to point out that the term PiN detector refers to a structure composed by a sequence of p-doped/intrinsic/n-doped silicon. Standard silicon sensors are often called PiN diode, PiN detector, or PiN sensors, even though the bulk is not made of intrinsic silicon but is lightly doped (Ferrero et al., 2021). A schematic of an n-in-p PiN and LGAD sensor is depicted in Fig. 1.11a. Charge multiplication by impact ionization happens for the electrons and less extent the holes in silicon detectors when charge carriers drift in a region with an electric field greater than 300 kV/cm (Sola et al., 2019).

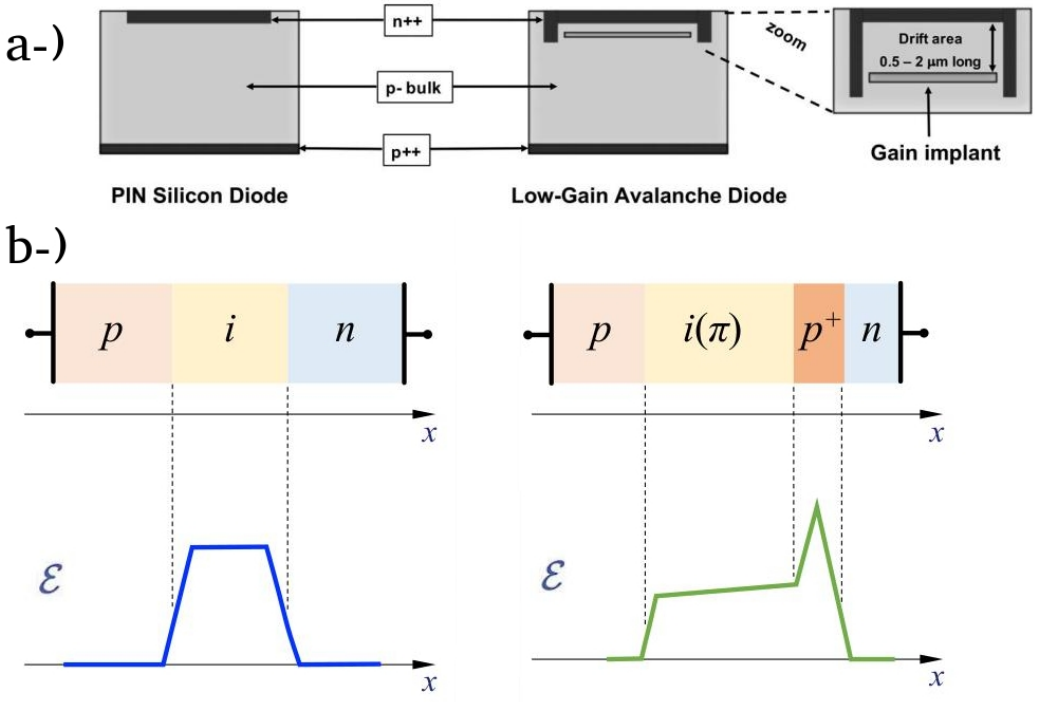

FIGURE 1.11: (a) A schematic view of: (left) an n-in-p PiN diode. (right) a Low-Gain Avalanche Diode. The LGAD design is characterized by the presence of an additional p^+ implant underneath the pn junction. Picture taken from (Ferrero et al., 2021). (b) Schematic of the Electric Field in depth in (left) PiN diode (right) LGAD. The dashed lines for the position of the electric field in each regions of both detectors do not match its exact position, they are only illustrative.

For the cases of carbon applications in which the expected deposited charge

in a PiN sensor is between 37 fC and 78 fC for 398.84-115 MeV/u, respectively, in 60 μm of active thickness, a gain layer is not more necessary. For that reason, a simple thin PiN detector was used in measurements related to carbon ions. For FLASH applications, a PiN detector was also used because the expected generated charge is sufficiently large to be detected for a single PiN diode. For example, in a sensor with an active thickness of 100 μm with a pixel area of 1 mm^2, a 5 μs of pulses of 6-MeV electron beam with a dose rate of 10^7 Gy/s will produce a charge of 2.2 μC (Vignati et al., 2020c).

1.3 Italian particle therapy centers involved in this work

Currently, in Italy, there are three charged particle therapy facilities in operation:
◦ The CATANA (Centro di AdroTerapia Applicazioni Nucleari Avanzate) proton therapy center located in Catania is equipped with a superconductive cyclotron and it was the first Italian clinical facility to make use of energetic (62 MeV) proton beams for the radioactive treatment of solid tumors. The CATANA facility is based on a passive transport system of a 62 MeV proton beam. The proton maximal range, at the irradiation point, is about 3 cm, ideal for the treatment of eye tumors (CATANA, 2023-02-25).
◦ The Trento Proton Therapy Center located in Trento is equipped with a cyclotron (IBA, Proteus 235). It has two treatment rooms for patients and one for experimental use and research (PTC, 2023-02-25).
◦ The National Centre for Oncological Hadrontherapy located in Pavia is the first hospital-based light ion therapy facility built in Italy. It is equipped with an "in-house" built synchrotron and beam monitor (BM) systems, providing actively scanned proton and carbon ion pencil beams (CNAO, 2023-02-25).
The following section summarizes the main characteristics of the two Particle Therapy Centers (Trento, Pavia) where the detectors were tested.

1.3.1 Trento Proton Therapy Center (Cyclotron)

The Trento proton beam is provided by a cyclotron, which is a particle accelerator developed by E.O. Lawrence in the 30s at the University of California, Berkeley (USA) (Lawrence, 1934). Basically, a cyclotron is a flat cylindrical vacuum chamber separated into two hollow D-shaped sheet metal electrodes

(called "Dees") by a small gap along its diameter (see Figure 1.12a). The Dees are mounted with their adjacent diametrical edges between two electromagnets, which produce a uniform magnetic field normal to the Dees plane. At the same time, a high-frequency alternating voltage is applied to these plates, therefore, in the narrow gap between the "Dees" an oscillating electric field is created. An emitted proton with an initial velocity (v_0) is initially accelerated by the electric field when it crosses the gap between the Dees. Inside the plate, the particles will follow a semicircular path, due to the influence of the Lorentz force caused by the magnetic field, emerging again in the gap region. The magnetic field is adjusted so that the time it takes to traverse the semicircular path within the Dee is equal to the half period of the oscillations. Accordingly, the electric field will have reversed its direction when the protons return to the gap region. The protons will then receive a second speed increase as they pass into the other Dee. Since the radius of the paths is proportional to the speeds of the protons, the time it takes to travel a semicircular path is independent of their velocities. Therefore, if the protons use precisely half a cycle $P_{1/2}$ in the first semicircle, they will behave similarly in all the successive ones and, therefore, will move in a spiral and in resonance with the oscillating field until they reach the periphery of the accelerator. Its final kinetic energy will be many times greater than its initial one, and will be proportional to the voltage applied to the electrodes multiplied by the number of times the proton has passed through the space between the Dees. However, since the frequency depends on the mass of the proton $(\frac{qB}{2\pi m})$, it will begin to decrease for higher energies as a consequence of the relativistic effects that appear when protons are accelerated to energies higher than 20 MeV. For this energy, the speed of the proton becomes a considerable fraction of the speed of light (0.2) and the mass of the proton increases by 2% with respect to the rest mass. This unavoidable effect becomes worst with the further increase of the proton energy. For instance, for 250 MeV, the ratio between v/c is about 0.61; consequently, the mass increase is 1.27. In a homogeneous magnetic field, would imply that the frequency would drop with energy. For example, with increasing energy (i.e., radius), the protons would lose pace with the acceleration voltage and would no longer be accelerated. The way some cyclotron producers, such as Varian and IBA, address this physical limitation on the world's most advanced cyclotron is by increasing the magnetic field with the radius in the isochronous cyclotrons (Paganetti, 2018). Therefore, the relativistic proton increase of mass is compensated by the lower magnetic field in the" valleys" in order to reduce the proton path

and adjust to constant frequency.
The isochronous cyclotron installed by the IBA company (Ion Beam Application, Belgium) at the Trento Proton Therapy Center (Italy) is the model IBA, Proteus 235, as shown in Fig. 1.12b. It has a diameter of about 4.5 m with a weight of 240 tons (IBA, 2023-02-25). It can accelerate protons to a maximum energy of 228 MeV shortly after the cyclotron exit. A rotating degrader of different thicknesses and materials performs a coarse energy selection to reduce the beam energy reaching a minimum value of 70 MeV with a beam intensity at the extraction ranging between 1 and 320 nA (It is the charge collected by an ionization chamber which can be positioned in the beam line shortly after the cyclotron exit and before the energy selection system), modulated by a 50 percent duty-cycle square wave, with a 100 ms period. The flux measured at the isocenter, integrated over the beam profile for 1 nA goes from $3.8x10^6$ p/s for 70.2 MeV to $2.3x10^8$ p/s for 228.2 MeV. These values can be scaled accordingly up to 320 nA (Tommasino et al., 2017).

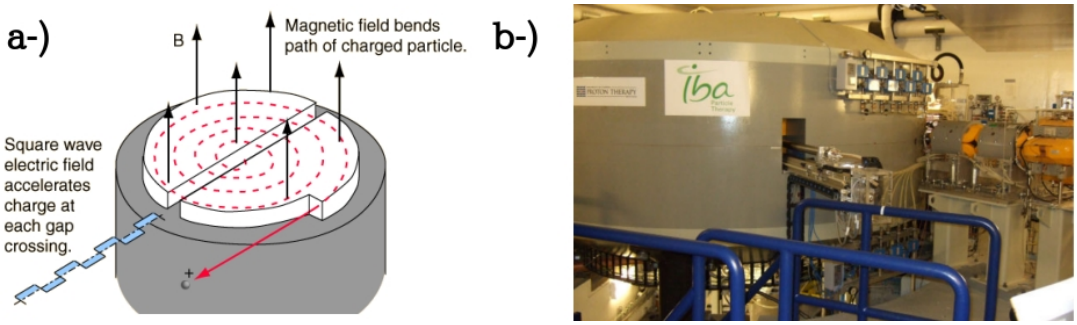

FIGURE 1.12: (a) Scheme of a typical cyclotron. Picture taken from (Peach, Wilson, and Jones, 2011). (b) The isochronous cyclotron model Proteus 235 from the IBA company. Picture taken from (Ridolfi, 2015).

1.3.2 National Centre for Oncological Hadrontherapy (Synchrotron)

The first accelerator to break the 1 GeV barrier was the cosmotron, a proton synchrotron at Brookhaven National Laboratory (United States). The cosmotron reached energies of 2.3 GeV in 1952 and later reached about 3 GeV. In the mid-1960s, two operating synchrotrons regularly accelerated protons to energies of about 40 GeV: the Alternating Gradient Synchrotron at Brookhaven National Laboratory and a similar apparatus near Geneva, Switzerland, controlled by CERN, the European Organization for Nuclear Research.

In the early 1980s, the two largest proton synchrotrons were a 500 GeV apparatus at CERN and a similar one at the Fermi National Accelerator Laboratory (Fermilab), located near Batavia in the United States. The capacity of the latter, called a Tevatron, was increased to a potential limit of 1 TeV (one teraelectronvolt, or TeV, equals one trillion volts) in 1983 by installing superconducting magnets, making it the most powerful accelerator in the world. In 1989, the Large Electron-Positron Collider (LEP), a 27 km ring that can accelerate electrons and positrons to an energy of 50 GeV, began operating at CERN (Jayakumar, 2012).

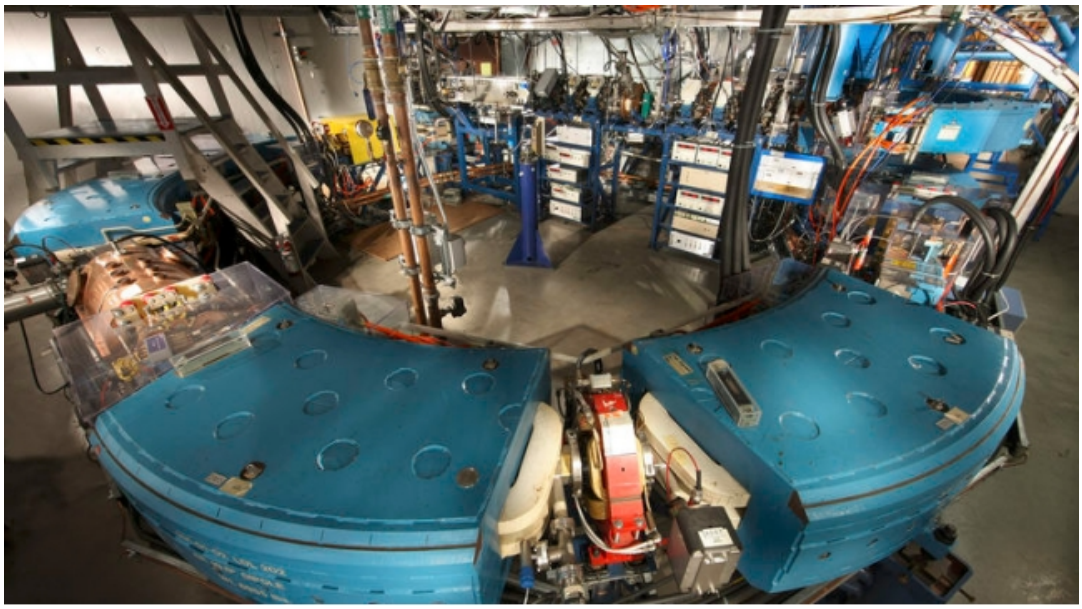

FIGURE 1.13: Synchrotron installed at Loma Linda Medical Center in California (United States). Picture taken from (LLUH, 2023-02-25).

The synchrotron is the newest and most powerful member of the family of accelerators. It is formed by a tube in the form of a large ring through which the particles move. The tube is surrounded by magnets that cause the particles to move through the center of the tube. The particles enter the tube after being accelerated to several million electron volts by, typically, a LINAC (linear accelerator). In the ring, they are accelerated at one or more points each time they describe a complete circle around the accelerator. The intensities of the ring magnets are increased as the particles gain energy to keep them in a constant orbit. Within a couple of seconds, the particles reach energies greater than 1 GeV and are ejected, either for direct experimental analysis or to launch at targets that produce various elementary particles when hit by the accelerated particles. Therefore, the main difference with respect to the

cyclotron is that in a synchrotron both the magnetic field and the electric field frequency are varied. In a synchrotron, the particles are accelerated in cycles, the so-called spills. First, the accelerator is filled with a certain number of protons of several MeV. In the acceleration stage, the protons are accelerated to the desired energy, typically between 60 to 250 MeV, and then slowly extracted into the beam line. Finally, the unused protons are decelerated and dumped at low energy.

The first synchrotron to be used in a hospital-based proton therapy center was at Loma Linda Medical Center in California (United States), which was built by Fermilab and started its operation in 1992 (Paganetti, 2018). It is a very compact accelerator with a diameter of about 610 cm (see Fig. 1.13). The system accelerates protons to a minimum energy of 70 MeV in 0.25 s and to a maximum energy of 250 MeV in 0.5 s.

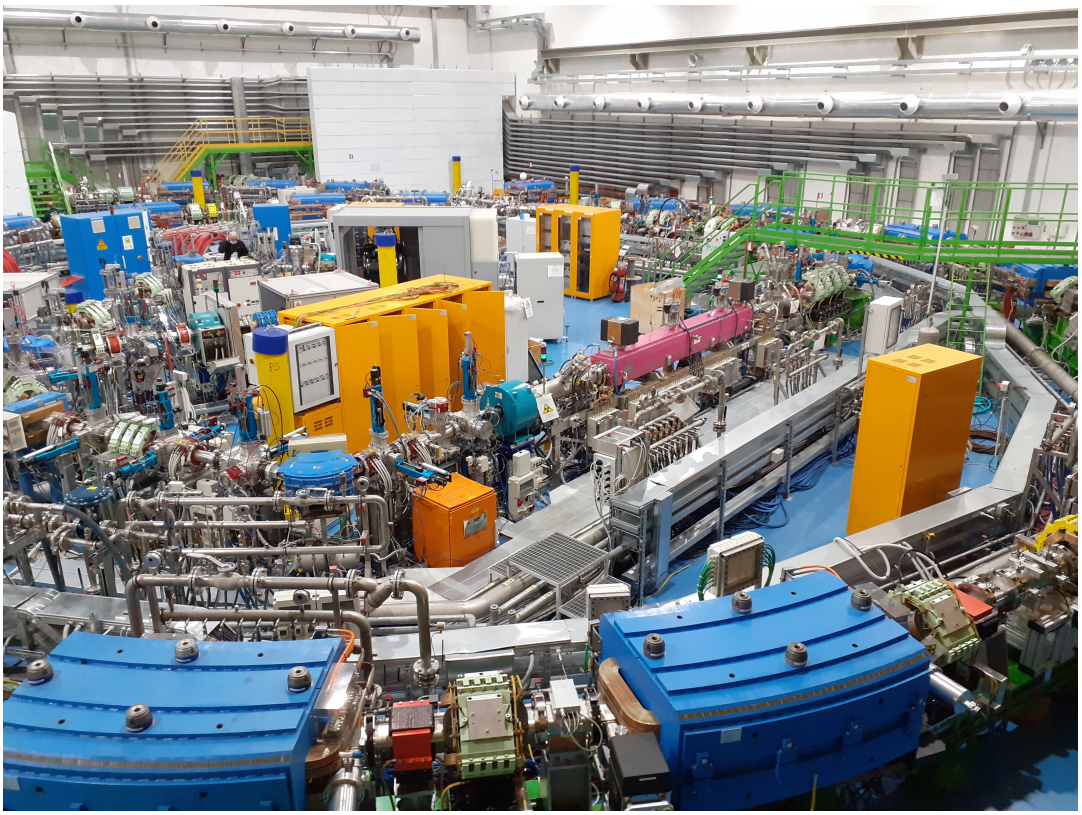

FIGURE 1.14: Synchrotron installed at the National Centre for Oncological Hadrontherapy (CNAO, Pavia, Italy).

Both synchrotrons and cyclotrons are being used for proton therapy, but for heavy-ion therapy; the synchrotrons are currently the only machines in operation in the world (Paganetti, 2018). Synchrotrons have several advantages compared to their competitors (the cyclotron) for proton therapy. The first is

that the particles can be accelerated to the desired energy, with almost no radioactivity due to beam losses. Also, the lower energy proton beam has the same intensity as the higher energy beam because there is no transmission losses due to the degrader.

The synchrotron within a 1600 m^2 bunker located in the National Centre for Oncological Hadrontherapy (CNAO, Pavia, Italy) has a diameter of 25 m and 80 m of circumference ring, as shown in Fig. 1.14. The bunker is isolated from the rest of the center by reinforced concrete with a thickness between 2 and 6 m (CNAO, 2023-02-25). An important characteristic of this center is that it can accelerate protons and carbon ions. The commissioned energies for protons beam range between 62.73 to 228.57 MeV and for carbon ions between 115.23 to 398.84 MeV/u (Mirandola et al., 2015). The beam can be modulated in four discrete level of beam intensity which are: 100%, 50%, 20%, and 10% of I_{max} which is $3x10^9$ and $6x10^7$ for protons and carbon ions, respectively.

Chapter 2

Characterization of thin sensors designed for beam monitoring

2.1 Introduction

The University and INFN of Turin are developing beam monitors for particle therapy based on segmented LGAD technology (Vignati et al., 2017; Sacchi et al., 2020; Marti Villarreal et al., 2021; Vignati et al., 2020a). Nowadays, the monitoring of clinical beams employs, to a greater extent, gas-filled ionization chambers, which offer several advantages in terms of robustness, transparency to the beam, large sensitive area, and good radiation resistance. However, the slow charge collection time and the sensitivity restricted to thousands of particles limit their use in the forthcoming advanced delivery techniques, such as fast scanning modalities (Giordanengo and Palmans, 2018). Solid-state detectors could be an ideal alternative for the new generation of beam monitors because they feature a fast signal (ns), good time resolution (< 100 ps), and the sensitivity to detect single protons. However, radiation damage and signal pile-up are serious concerns for their use on high fluxes of therapeutic beams.
Among the solid-state detectors, the Ultra-Fast Silicon Detectors (UFSD) (Ferrero et al., 2021), based on the LGAD (Pellegrini et al., 2014) technology, were selected, within the INFN MoVe-IT [1] project, to develop two prototypes. The first one is a proton counter to be used as an online monitor of the fluence rate of clinical proton beams (Vignati et al., 2017; Sacchi et al., 2020; Fausti et al., 2021) and the second is a device able to measure the beam energy using Time-of-Flight technique (Marti Villarreal et al., 2021; Vignati et al., 2020a).

[1] https://www.tifpa.infn.it/projects/move-it/

The sensors used represents an evolution of the n-on-p planar silicon sensor where a thin (1 micrometer) p^+ gain layer is implanted under the n^{++} cathode, as explained in Chapter 1. As a result of the doping profile, characterized by a large doping concentration at the n^{++}/p^+ junction, a local increase of electrical field up to 300 kV/cm creates a controlled moderate electron/hole avalanche multiplication without a complete breakdown. This effect leads to a proportional signal enhancement with a noise level similar to that of a traditional silicon sensor of the same geometry (Sadrozinski et al., 2013; Ferrero et al., 2021; Sola et al., 2019).
In 2020 we designed several sensors with diverse characteristics tailored to the needs of the two devices developed within the MoVe-IT project. The production is called MoVe-IT-2020. They are segmented into strips to reduce the particle rate per channel and minimize the signal pile-up. This chapter will described the laboratory characterization of all the sensors used in this thesis. Also, briefly will be presented the signals obtained in a preliminary test with proton beams at the National Centre for Oncological Hadrontherapy (CNAO, Pavia, Italy) using a sensor with a large area from the MoVe-IT-2020 production.

2.2 Sensor design and production

For this production, the design of the sensors was based on previously optimized parameters, determined in the second production of UFSD at the Fondazione Bruno Kessler (FBK, Trento, Italy) (Ferrero et al., 2017). In each strip, a p^+ gain layer was added by implanting boron below the n^{++} electrode with a doping concentration of $\sim 10^{16}/cm^3$ and a thickness of ~ 1 μm. This p^+ layer generates an electric field large enough to activate charge multiplication (Sadrozinski et al., 2013). In the region between two neighboring strips, two highly doped p-type implants (p-stops) are used to isolate the two strips. In addition, the Junction Termination Extension (JTE, also called n-deep) surrounds the gain layer of each strip, collects the $e-h$ pairs generated in the inter-strip region, and controls the electric field at the strip edge (Paternoster et al., 2021). Assuming ideal isolation, the inter-strip geometrical distance of the two gain layers would correspond to a dead region from which the released charges are not multiplied by crossing the gain layer.
The sensor dedicated to the counter prototype consists in a sensitive area of 2.6x2.6 cm^2 (Fig. 2.1a) intended to cover the entire clinical beam spot at the isocenter (for example, in the tratment rooms of CNAO, the proton beam

FWHM ranges between 0.7 and 2.2 cm in the clinical energy range (Mirandola et al., 2015)). It is segmented into 146 strips (Fig. 2.1a) with a pitch of 180 μm, an inter-strip of 66 μm, and each strip has an active area of 114 x 26214 μm^2 . For testing purposes, two strips (strips 1 and 2) were manufactured without the gain layer implant and thus behaved like conventional PiN diodes.

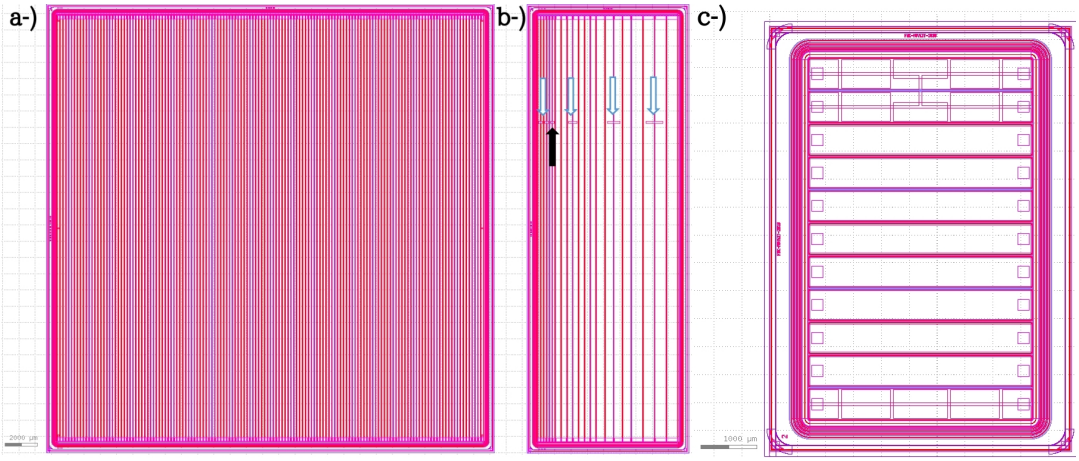

FIGURE 2.1: Layout of a sensor type A. (b) Layout of a sensor type E. The arrows point to the optical windows present in the sensor. The black-filled arrow indicates the optical window used, which has 100x237 μm^2. (c) Layaout of a sensor type T.

Eight big area sensors were positioned on each wafer (see Fig. 2.2), named type A, where the additional subscript identifies the position of the sensor in the wafer. They have identical geometry and underwent a similar processing described above except for the sensor A_3, where the gain layer was not implanted in any strips.
Other four additional sensor geometries are also present (see Fig. 2.2). Sensors B, E, and F, featuring different strip pitches and 1/3 of the surface area of type A, were designed for laboratory testing. In particular, small apertures on the strip metallization (optical windows), orthogonal to the LGAD strips and extending over the inter-strip region, are present in the sensors type E as shown in Fig. 2.1b. It allows injecting an infrared laser beam to study the sensor response as a function of the position in the inter-strip region. The smaller detectors labeled T (Fig. 2.1c) were designed for timing applications (Marti Villarreal et al., 2021; Vignati et al., 2020a). They are segmented into 11 strips (10 with gain, 1 without gain), each one characterized by a sensitive area of 2.2 mm^2 (4 mm x 0.55 mm), an interstrip pith of 0.591 mm, and a inter-strip distance of 51 μm. Is important to remark that in sensors T_1, T_8, and T_{10} the gain layer was not implanted in any strips.

In this work, only sensors type A, T, and E were tested. The entire production, performed at the FBK, includes 14 wafers subdivided into three groups based on wafer substrate and gain implant dose, as summarized in Table 2.1.

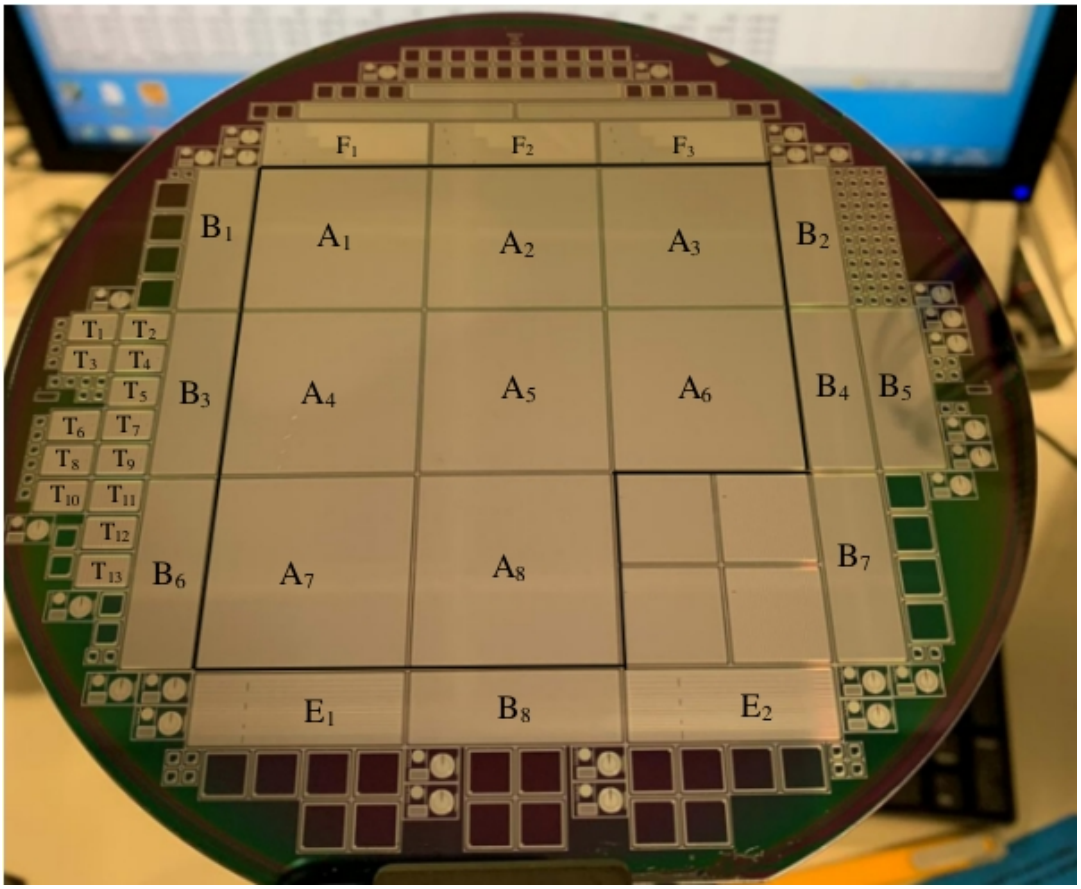

FIGURE 2.2: Picture of a wafer, the capital letter A, B, T, E and F indicate different sensor geometries.

The acceptor dopant used for the gain layer implant was boron, processed with a low-diffusion thermal cycle and enriched with a dose of carbon in order to maximize the radiation resistance (Ferrero et al., 2021; Sola et al., 2019). It was shown that using this manufacturing process, 80 % of the active fraction of the gain layer is preserved up to a fluence of 1.5x10^{15} n_{eq}/cm^2 (Ferrero et al., 2021), which corresponds approximately to one year of clinical proton irradiation in a single treatment line (Vignati et al., 2020a).
Two different silicon substrates were used, both exploiting a low resistivity silicon back handling support: epitaxial grown silicon layer (Epi) with a resistivity larger than 200 Ωcm, with an active thickness of 45 μm, and a high resistivity (>3000 Ωcm) glued silicon layer (Si-Si) with an active thickness of 60 μm . Additionally, two doses of boron in the gain layer implant were

Group	Wafer n.	Substrate	Dose P_{GAIN} (a.u)	Thickness(μm)
I	1,2,14	Epi	0.96	45
II	3,4,5,6,7	Si-Si	0.96	60
III	8,9,10,11,12,13	Si-Si	0.98	60

TABLE 2.1: Summary of MoVe-IT 2020 FBK's production. The processing dose of the gain implant is expressed in arbitrary units.

used, as shown in Table 2.1. More information about the fabrication of silicon LGAD sensors are described in (Giacomini, 2021).

2.3 Laboratory characterization

Measurements were performed at the Physics Department of the University of Turin (UNITO, 2023-02-26) and at FBK (FBK, 2023-02-26). The experimental setups used for the tests are described in the following subsections.

2.3.1 Static characterization (I-V curves)

The sensors were tested by measuring the leakage current in the strips and the total leakage current flowing through the device as a function of the reverse bias voltage (I-V curves). The results were used to search for abnormal behaviors both in individual channels and in the entire device under test (DUT). For the sensor type A due to its big sensitive area and the large number of strips two different experimental setups, based on a probe station connected to a power device analyzer, were used for the measurements. The first setup used a dedicated probe card, and the second one used a conductive polymer (elastomer). The main benefit of the first experimental setup is the ability to measure the behavior of a single strip. However, the limited number of needles on the probe card makes measurements time-consuming, especially for large area sensors. Indeed, in the case of our large sensor it was impossible to contact all strips and a large number of strips were left floating during each measurement. This could result in an anomalous behavior in a sensor, as explained by (Ferrero et al., 2021). On the other hand, the use of an elastomer allows faster measurements, since it is possible to contact all the strips at the same time, although sacrificing the information of a single strip, which is the main drawback. For the sensor type T, only the setup explained in subsection 2.3.1(a) was used. More details on both experimental setups are given in the next subsection.

(a) Switching matrix and probe card

The schematic setup shown in Fig. 2.3 was used to test each of the strips of the sensor individually. It is based on a Power Device Analyzer (Keysight B1505A) and a custom probe card designed and produced by Technoprobe[2]. Two probe card were used. For testing the sensor type A, a probe card with 40 needles for contacting 40 neighboring strips and an additional needle for grounding the inner Guard Ring (GR) was used. Instead for testing the sensor type T, a probe card with 11 needles and 2 additional needles for grounding the inner Guard Ring was used. In both cases, the sensor was placed on top of the chuck, in electrical contact with it, and was held in position through a vacuum pump. The chuck was connected to the Power Device Analyzer through the High Level (-V) output of the High Voltage Source Monitor Unit B1513C (HV-SMU). The Low Level (0 V) output of this module was connected to the GR using the corresponding needle of the probe card (see Fig. 2.3).

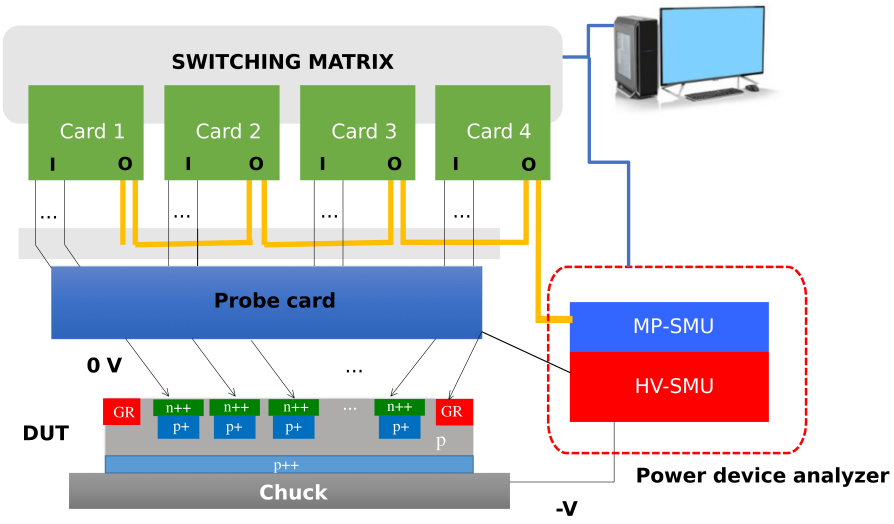

FIGURE 2.3: Schematic of the experimental setup that makes use of a switching matrix and a custom probe card.

In this arrangement, the HV-SMU polarizes the sensor inversely, thus defining the working voltage of the sensor and measuring the total current flowing on the backplane of the device. A compliance current (typically set to 100 μA but in some cases increased to 400 μA for the sensor type A; instead for the sensor type T, 50 μA was used) was set through the analyzer to prevent the

[2]https://www.technoprobe.com/

over-exponential growth of the leakage current at large reverse polarization voltages, thus protecting the DUT. A Keithley 7002 Switch System equipped with four Keithley 7058 low current scanner cards was used to connect the Medium Power Source Unit B1511B (MP-SMU) of the analyzer to the needles of the probe card, allowing to automatically select the strip being measured while grounding all the remaining. A program was configured to iteratively measure the leakage current flowing in each strip through the MP-SMU unit by varying the polarization voltage of the sensor in steps.
In this setup, 40 strips could be contacted simultaneously for sensor type A (24 strips being measured and the remaining 16 strips being grounded). After each measurement, the needles of the probe card were moved to the next 24 strips until all the 146 strips of the sensor were tested. A similar system was used for the measurements carried out at FBK for sensor type A, although using a probe card with 24 needles. For the sensor type T, the probe card used can contact the 11 strips plus the GR at the same time.

(b) Conductive polymer

The second setup consists in a elastomer that allows measuring the sum of the currents flowing in all strips and the GR at once. Referring to Fig. 2.4, a thin elastomer strip was cut and positioned (a) on top of the sensor, covering the strip contact pads and the GR. (b,c) A mask and a cap with the same detector dimensions, designed using 3D AutoCAD[3] 2020, were created with a 3D printer (ORIGINAL PRUSA i3 MK3)[4]. The mask featured a small aperture which, when the mask was positioned above the sensor, exposed the upper surface of the elastomer. The cap was designed with an insert facing the mask aperture, which was covered by a conductive copper tape. (d) The cap was placed on top of the mask, letting the copper contact the elastomer, and a crocodile clip was used to contact the conductive tape. (e) Finally, a block of lead was put on the top of the cap in order to ensure good contact between the conductive tape, the elastomer, the sensor strips, and the GR. In this setup, the detector was biased through the chuck, similarly to the setup described earlier, whereas the Low Level (0 V) output of the MP-SMU was used to read the current flowing in the elastomer.

[3]https://www.autodesk.it/
[4]https://www.prusa3d.com/category/original-prusa-i3-mk3s/

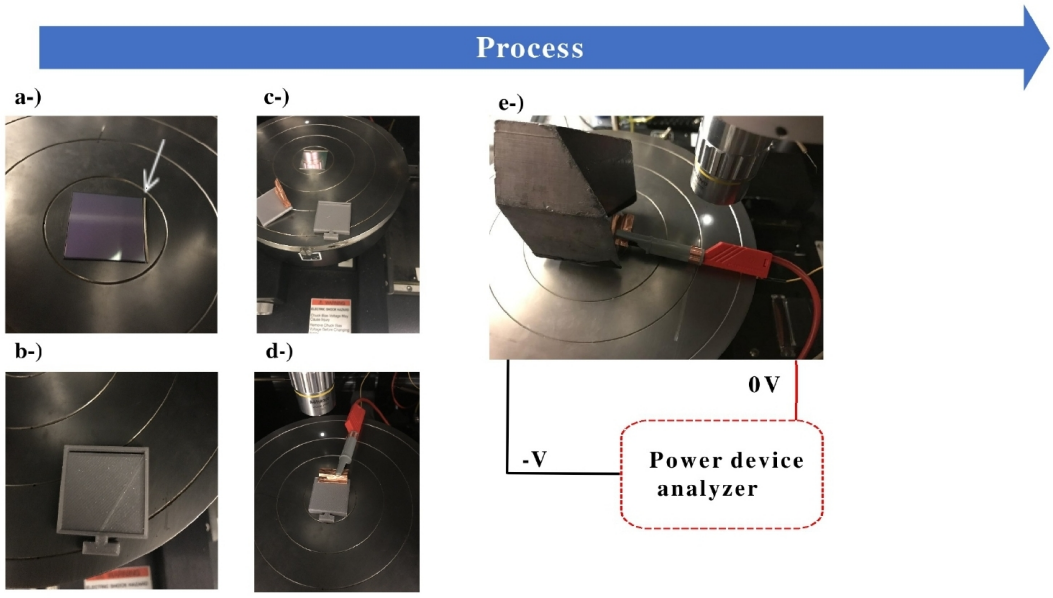

FIGURE 2.4: Steps of the experimental procedure for using the elastomer. The white arrow indicates the elastomer positioned on top of the sensor.

2.3.2 I-V curve analysis

The I-V measurement was performed by setting up the analyzer to automatically increase the sensor's reverse bias voltage in small steps and measuring the sensor's total current and the connected strip's current for each voltage value. For example, Fig 2.5a shows the I-V curves measured at room temperature using the experimental setup described in 2.3.1a for the 144 LGAD strips of sensor type A, and Fig. 2.5b the corresponding total current. Three main regions can be distinguished in Fig. 2.5a with increasing the reverse voltage. The region identified as (1) corresponds to the partial depletion of the sensor. In region (2), the sensor is fully depleted, and the slow exponential increase of the current is a consequence of the increase of the electric field, which induces charge multiplication in the gain layer. In region (3), the sudden over-exponential current increase indicates the onset of the sensor breakdown. In this example, the sensor cannot be operated at reverse bias voltages above 200 V, where the breakdown region starts.
An automatic algorithm, based on the numerical first derivative $\Delta I/\Delta V$, after smoothing the curves with a moving average[5], was implemented in Matlab[6]

[5]https://it.mathworks.com/help/curvefit/smooth.html
[6]https://it.mathworks.com/

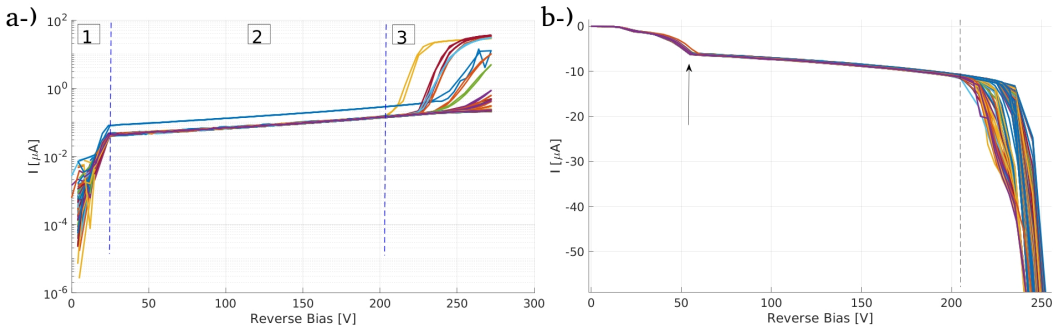

FIGURE 2.5: Leakage current as a function of the reverse bias voltage in each strip, where the three regions of the sensor: depletion (1), full depletion (2) and breakdown (3) are indicated. (b) Corresponding total leakage current of the sensor. The vertical line corresponds to the maximum reverse bias voltage at which the sensor can be operated and the black arrow indicates the depletion voltage of the GR. These data refer to the 144 LGAD strips on sensor A_2, wafer 3.

to extract from the I-V curves of Fig. 2.5 the parameters of interest. It is important to note that this method was also applied when measurements were made with the experimental setup described in 2.3.1b.

The full depletion voltage (V_{FD}) of a channel is defined as the bias voltage measurement point after the first minimum of the second derivative of the curve of Fig. 2.5a. A similar method is applied to determine the depletion voltage of the GR (V_{GR}) using the absolute value of the current shown in Fig. 2.5b and considering the second minimum of the second derivative. The resolution on these two quantities is given by the voltage step set up for the measurements, typically 2 to 4 V.

The breakdown voltage (V_{BR}) of the sensor is defined as the minimum of the breakdown voltages determined using each of the curves of Fig. 2.5b separately. First, the slow increase of the absolute value of the current I, after the depletion voltage of the GR (the black arrow in Fig. 2.5b) is fitted recursively with an exponential function by adding measurement points at increasing voltage. This allows to identify the bias voltage above which the fit starts to fail with a coefficient of determination $R^2 < 0.97$, indicating the onset of the over-exponential growth. Considering the measurements in this region, the breakdown voltage is defined, according to (Bacchetta et al., 2001; Fernandez, 2021), either as the maximum voltage at which the quantity K(I,V)= ΔI/ΔV • V/I < 8 or the voltage at which the current I overcomes the compliance set up in the analyzer, whichever occurs first.

2.4 Static characterization (C-f and C-V curves)

Fig. 2.6 illustrates the experimental setup used to measure the capacitance-frequency (C-f) and capacitance-voltage (C-V) curves. The sensor was placed over the chuck, connected through the bias tee to the High Level (-V) output of the HV-SMU unit of the analyzer, thus providing the reverse bias voltage through the backplane. The Low Level (0 V) output was applied to the strip being measured using the manipulators of the probe station. The additional Multi-Frequency Capacitance Measurement Unit Module B1520A (MF-CMU) was used to generate an AC signal, which was fed into the DC bias using a bias tee. Finally, the two adjacent strips and the GR were short circuited to the ground using additional manipulators. This arrangement allowed measuring the capacitance of the detector strip and studying its dependence with respect to the reverse bias voltage and the frequency of the AC signal, thus gaining insights on sensors characteristics, as explained in the next section.

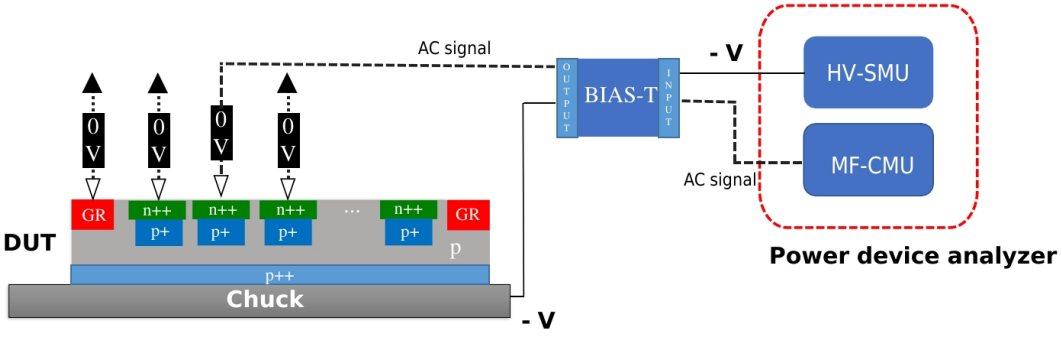

FIGURE 2.6: Schematic representation of the setup using the manipulators to perform the C-f and C-V measurements.

2.4.1 C-V curve analysis

The C-V curve allows to determine separately the depletion voltage of the gain layer (V_{GL}) and the bulk of the sensor. Referring to the C-V curve of a strip shown in Fig. 2.7a (dashed line), when increasing the reverse bias voltage the depletion starts from the n^{++}/p^{+} junction. Due to the large doping concentration of the gain layer, about 20 V are necessary to deplete it. After the knee shown in the curve, the space charge region is extended to the bulk and, due to its large resistivity, only few additional volts are necessary to reach the full depletion of the sensor, where the dashed curve reaches a

constant minimum. The depletion voltage of the bulk (V_{BU}) can thus be obtained as $V_{BU} = V_{FD} - V_{GL}$. To locate the position of the knee, corresponding to V_{GL}, the first minimum of the numerical second derivative (D_2) of the C-V curve, shown in Fig. 2.7b, is used. Similarly, V_{FD} is located by a) identifying the point where second negative minimum in D_2 occurs and b) starting from this position and considering points at increasing voltage, finding the voltage of point where the first occurrence of the condition D_2(i)xD_2(i-1) <=0 is met. It is important to remark that this method has a precision limited by the step of 0.2 V used for the voltage sweep in the measurements.

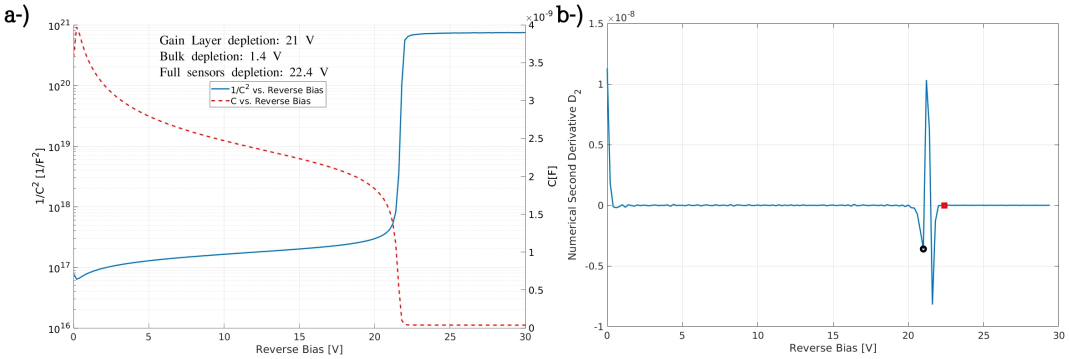

FIGURE 2.7: (a) $1/C^2$ vs. reverse bias voltage (solid line and left vertical axis); C vs. reverse bias voltage (dashed line and right vertical axis). (b) Numerical second derivative of the C-V curve vs. reverse bias voltage. The black circle represents the gain layer depletion voltage. The full depletion voltage is shown as a red square mark.

The $1/C^2$-V curve shown in Fig. 2.7a (solid line) allows to determine the acceptor doping concentration (N) as a function of the depth in the sensor (w) which is given by $\frac{\epsilon_{Si}A^2}{C(V)}$. The relation can be expressed as:

$$N(w) = \frac{2}{e\epsilon_{Si}A}\frac{\Delta V}{\Delta(1/C^2)} \tag{2.1}$$

where:

A : is the sensor area

ϵ_{Si}: is the silicon permitivity

e : is the elementary charge

$\frac{\Delta V}{\Delta(1/C^2)}$: is the numerical derivative

2.5 Measurements of the inter-strip dead region

An infrared picosecond laser[7] with a wavelength of 1064 nm, corresponding to an absorption depth of approximately 1 mm in silicon, was used to reproduce the charge deposition of particles crossing the detector. The laser light was split in two paths, 89.5 % of the yield going to a reference diode to monitor the laser intensity and stability, and the remaining being focused in a spot of about 16 μm diameter on the sensor surface. The amplitude of the signal of the reference diode was calibrated in terms of MIP equivalent signal in the sensor such that, by varying the laser intensity and monitoring the reference diode, a known charge in a range from 2 to 6 $MIPs$ was injected into the sensor.

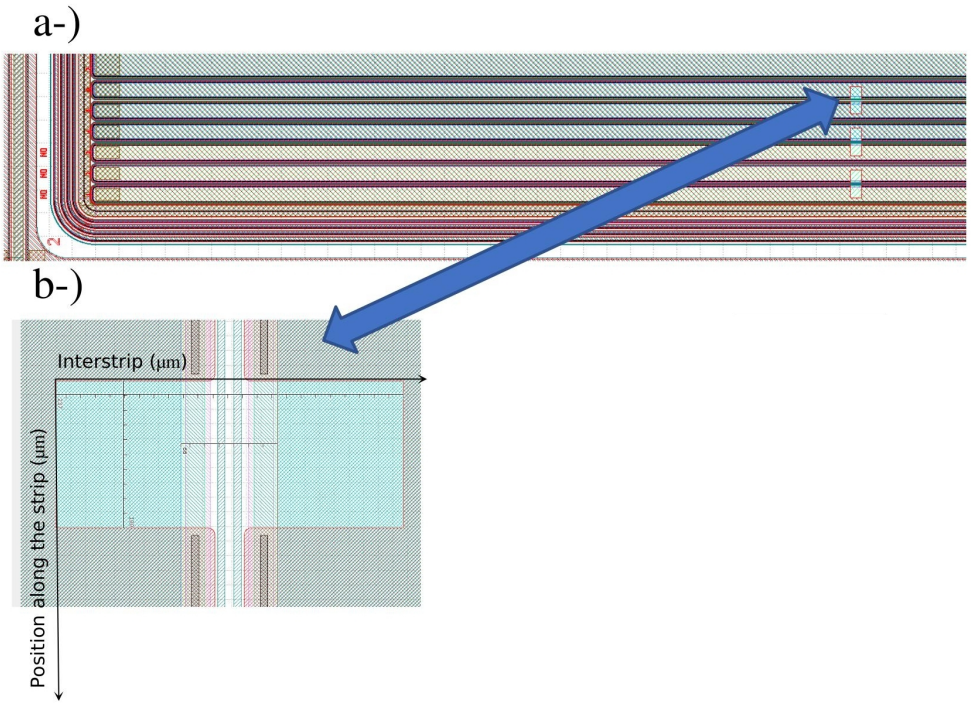

FIGURE 2.8: (a) Zoom of the layout of a sensor type E where can be see the optical windows of 100x237 μm^2. (b) Magnification of the optical window used in this study.

A test sensor type E, which feature an optical windows of 100x237 μm^2 as shown in Fig. 2.1b (Black-filled arrow) and in Fig. 2.8, was glued on a passive PCB board to bias the sensor and extract the signal from two neighboring channels. Two low-noise current amplifiers (CIVIDEC C2[8], 40 dB gain and 2 GHz bandwidth) were used to amplify the signals from the board and

[7] http://www.particulars.si/
[8] https://cividec.at/electronics-C2.html

read them with a Lecroy Oscilloscope (Waverunner 9254M, 40 GSample/s) triggered by the input signal used to activate the laser pulse. A xyz-stage control with sub-μm precision was used to align the sensor vertically and to perform a horizontal scan of the optical window with the laser spot. More details about the calibration curve of the reference diode and the experimental setup, briefly described in this section, can be found in (Ferrero et al., 2021).

2.6 Results and Discussion

2.6.1 Acceptance tests before cutting of sensors type A

The I-V curves of the sensors type A of the entire production, consisting of 112 detectors and 16352 strips, were measured at the FBK company on each wafer before cutting the sensors. The experimental setup was similar to the one described in section 2.3.1(a), and the measurements were performed at room temperature.

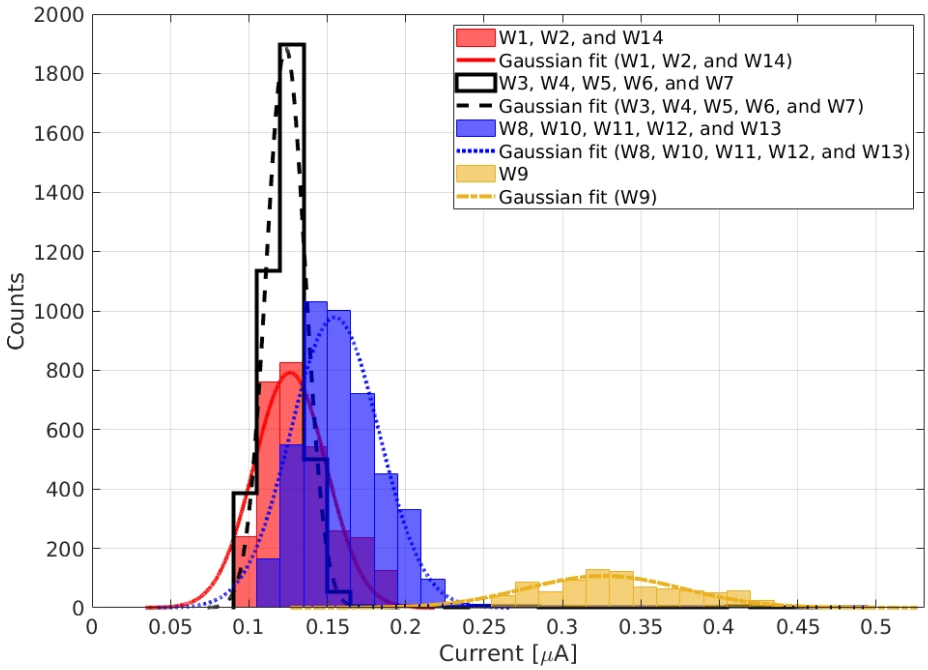

FIGURE 2.9: Current distribution at 160 V for good LGAD strips from different wafers.

It was observed that the non-working strips draw a current higher than 0.5 μA at 160 V. A reference bias voltage of 160 V was chosen, as it allows the saturation of the electrons drift velocity in thin LGAD detectors. Therefore,

Group	Wafer	$\mu(\mu A)$	$\sigma(\mu A)$	R^2	U
I	1,2,14	1.3e-01	3.3e-02	0.95	1.62
II	3,4,5,6,7	1.2e-01	1.8e-02	0.99	1.30
III	9	3.3e-01	7.1e-02	0.85	1.46
III	8,10,11,12,13	1.5e-01	4.0e-02	0.97	1.55

TABLE 2.2: Parameters obtained from the Gaussian fit and the ratio between the 90th and the 10th percentiles for the leakage current at 160 V for good LGAD strips, grouped by wafers with similar characteristics as shown in Table 2.1.

Sensors (with gain)						
Group	**Total strips**	**Good strips**	**Good strips (%)**	**Total sensors**	**Validated Sensors**	**Validated sensors (%)**
I	3066	3048	99.41	21	14	66.67
II	5110	4086	79.96	35	11	31.43
III	6132	5352	87.28	42	14	33.33
Total	14308	12486	87.27	98	39	39.80
Sensors (No gain)						
Group	**Total strips**	**Good strips**	**Good strips (%)**	**Total sensors**	**Validated Sensors**	**Validated sensors (%)**
I	438	436	99.54	3	2	66.67
II	730	728	99.73	5	4	80.00
III	876	876	100.00	6	6	100.00
Total	2044	2040	99.80	14	12	85.71

TABLE 2.3: Summary of the yield of the entire sensor production.

a strip is marked as bad if the current at the reference voltage exceeds 0.5 μA or if it cannot reach that value of reverse bias voltage. A sensor is validated if all the strips fulfill that tolerance. The leakage currents distribution at 160 V for good LGAD strips is shown in Fig 2.9.

As can be seen, three different groups are observed, each of which corresponds to different wafer characteristics (see Table 2.1). Only wafer 9 showed a different behavior than the other wafers of Group III and was fitted separately, resulting in a mean leakage current over two times larger than the other similar wafers. A possible reason for this behavior is a different temperature during the measurements, as the leakage current strongly depends on the temperature. Further investigation, described in the following sections, was carried out in Group III to understand the difference.

The distributions of good LGAD strip of Fig. 2.9 were fitted with a Gaussian

separately for each group, and the corresponding Gaussian parameters (average and standard deviation) from the fit are reported in Table 2.2. In order to evaluate the uniformity, the ratio (U) between the 90th and the 10th percentiles (90/10) was also included in the table. A value of U lower than 1.62 for all the cases was found, showing good uniformity.
Table 2.3 summarizes the percentage of good strips and validated sensors for the whole production, separately for sensors with internal gain (LGAD) and for the sensors A_3 without gain (PiN). In total, the percentage of working strips is 87.3% (LGAD) and 99.8% (PiN) while the percentage of validated sensors is 39.80% (LGAD) and 85.71% (PiN). Additionally, wafer 4 and wafer 12 each had 7 non-validated LGAD sensors, which worsened the performance of the entire production. It is important to remark that the relatively low yield of type "A" LGAD sensors is not completely unexpected considering the large area and the large number of channels in each sensors.

2.6.2 Full Depletion Voltage, Breakdown Voltage and Acceptance tests after cutting of sensors type A

After cutting the wafers, the sensors were delivered to the Physics Department of the University of Turin and the I-V measurements were repeated using the experimental setup and the methods described in section 2.3. Wafers 2, 4, and 12 were not analyzed after cutting. Fig. 2.10 a reports the full depletion voltage for all the sensors selected. For the sensors of Group I it was calculated as the average measured in each strip while for the sensors of Groups II and III the analysis was performed on the cumulated current measured simultaneously in all the strips and the GR with the elastomer.
For all the measurements, the uncertainty is assumed to corresponds to the voltage step of 4V (Group I, Wafer 1) and 2V (Group I, Wafer 14, Groups II and III). The median values and the maximum deviations of V_{FD} are 36^{+4}_{-8} V, 22^{+4}_{-0} V, and 24^{+0}_{-2} V for the sensors of Group I, Group II, and Group III respectively. The small difference observed in V_{FD} between sensors of groups II and III is mainly due to the difference in the acceptor concentration in the gain layer. The larger full depletion voltage for Group I originates from the lower resistivity of the epitaxial substrate, which translates into additional bias voltage needed to deplete the bulk than for the Si-Si wafer. This difference is confirmed by comparing the depletion voltage of PiN strips from wafer 1 and wafer 5 using capacitance measurements as described in section 2.4. It was found that 8 V are necessary to deplete a PiN strip from the

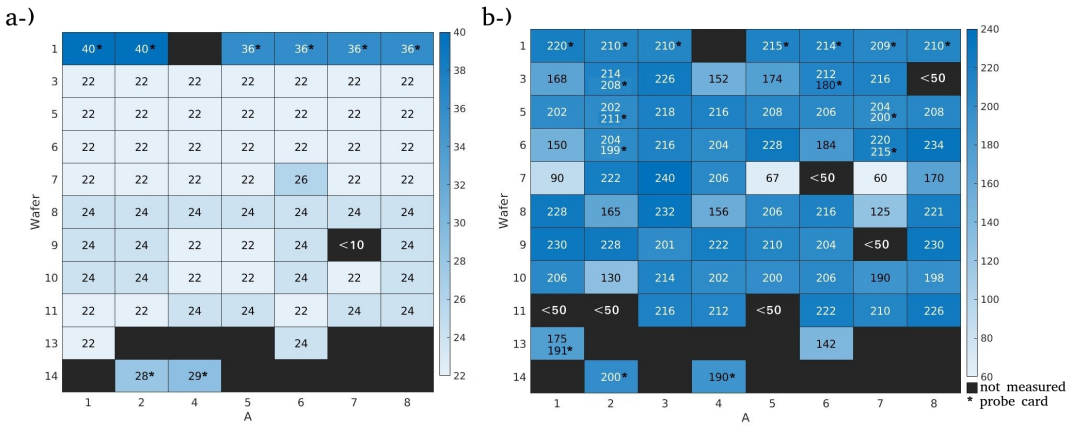

FIGURE 2.10: (a) Full depletion voltage obtained from the I-V curves. (b) Breakdown voltage in volts obtained from the I-V curves. The column 3 (A_3) refers to sensors without gain. The asterisks refer to measurements taken with the probe card while the unmarked ones to measurements with the elastomer.

wafer 1 (Epi) compared to 1 V for wafer 5 (Si-Si). The breakdown voltages are shown in Fig. 2.10b. A mean value of 209 $\pm$ 10 V and 202 $\pm$ 13 V were found for validated LGAD sensors of Group I and Group II, respectively, using the probe card. Instead, in the measurements with the elastomer an average value of 205 $\pm$ 17 V (Group II) and 214 $\pm$ 11 V (Group III) were obtained. For seven sensors, V_{BR} was measured with both the elastomer and the probe card. The values found with the two methods are consistent, with a larger value found using the elastomer in five of them, the difference being of a few % except for sensor A_6 of wafer 3 where the difference amounts to 15 %. It should be observed that, due to the limited number of strips grounded during the measurements with the probe card, floating strips create a large electric field between themselves and the surrounding strips, mainly at the inversion layer/p-stop junction, producing an earlier breakdown (Ferrero et al., 2021). Therefore, the values reported for Group I for the breakdown voltage of sensors "A" are underrated, and larger values are expected when all the channels of these sensors will be properly connected to the front end electronics.

In order to verify the effect of the cutting of the sensors, the selection criteria applied at FBK were applied again to a group of 16 sensors, randomly selected among validated and non-validated. Out of 2336 strips, only the strip number 82 of sensor A_5, wafer 1, formerly classified as bad, passes the criteria, thus confirming that the cut did not affect the yield of the production. To further investigate, Fig. 2.11 compares the I-V curves of the strips 81, 82, and

83 of this sensor measured at FBK and at UNITO, respectively before and after the cut. The slightly larger currents measured before the cut are probably related to the different number of strips contacted by the probe cards (40 at UNITO; 24 at FBK).

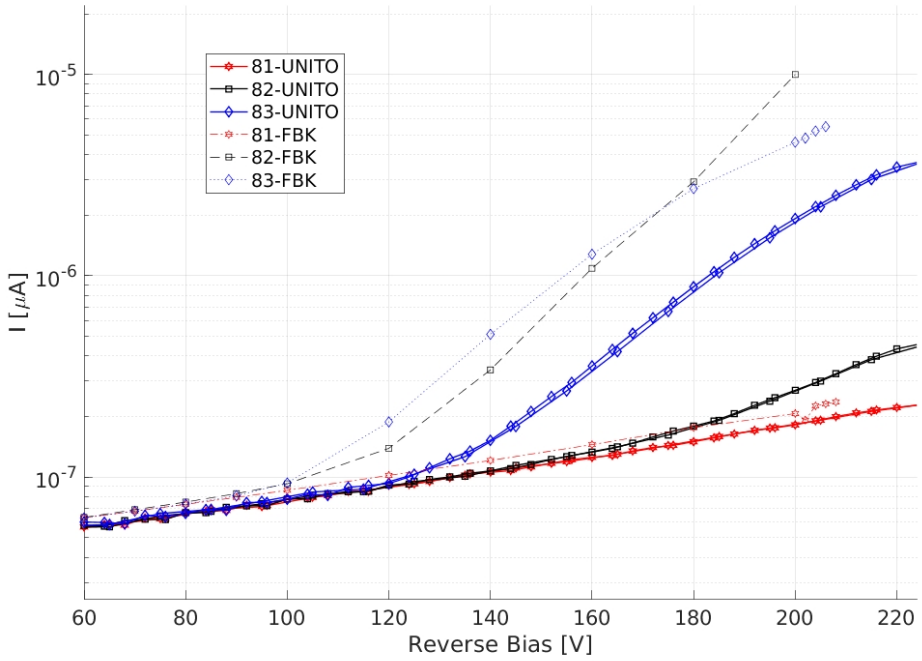

FIGURE 2.11: Leakage current vs. bias voltage for strips 81, 82, and 83 of sensor A_5 of the wafer 1 measured at FBK and at UNITO.

2.6.3 Breakdown Voltage and Acceptance tests after cutting of sensors type T

The I-V measurements of sensors type T were performed at the University of Turin after cutting the wafers. It was used the experimental setup described in section 2.3.1a, using a probe card with 11 needles for contacting the 11 strips plus two additional needles to contact the Guard Ring. The breakdown voltage and the number of good strips for the LGAD sensor number 2, 3, 4, 5, 6, 7, 11, and 13 of wafers 1, 3, and 8 were measured.

As we can appreciate in Fig. 2.12a, the breakdown voltage was for wafers 1,3 and 8 for validated sensor higher than 250, 190, and 229 V, respectively. Comparing the values of Fig. 2.12a with the breakdown voltage measured for sensor type A, larger values were observed for sensor type T. A possible explanation of this contrast is given for the different geometry of both types

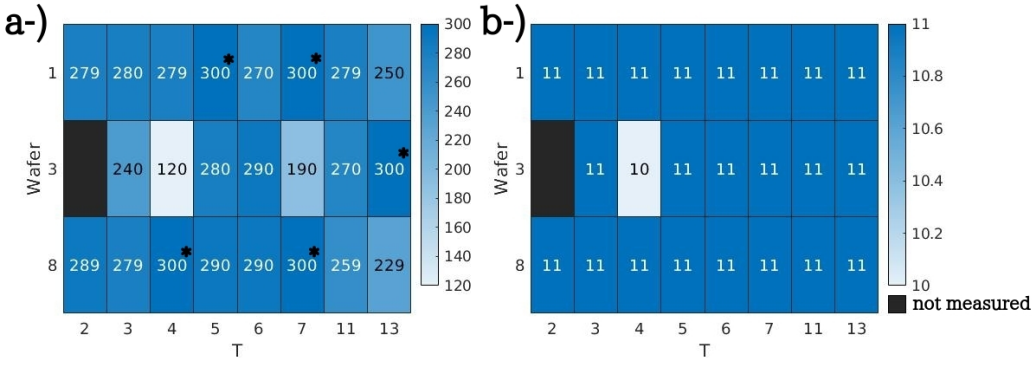

FIGURE 2.12: (a) Breakdown voltage in volts obtained from the I-V curves. (b) Good strips, the total number of strips of each sensor is 11. The asterix refer to a sensor in which the breakdown were not archieved; Therefore, 300 V refers to the maximum voltage set during the measurements at UNITO.

of sensors and the total number of strips. The breakdown voltage is measured on the backplane from each of the curves of Fig. 2.5b separately. Then, it is expected that a detector with more strips will have more bad strips that can worsen the breakdown voltage. Only one strip of 253 measured did not reach 160 V (see Fig. 2.12b), then was labeled as a bad strip. Therefore, 99.6% of the strips tested were good strip, representing the 96% of validated sensors.

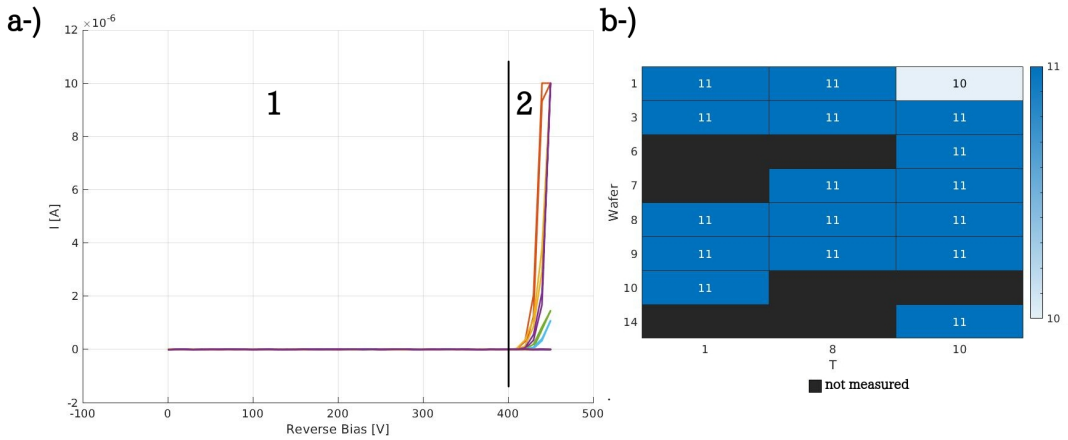

FIGURE 2.13: (a) Leakage current as a function of the reverse bias voltage in each strip for a PiN sensor (Wafer 10, T_1), where two regions of the sensor are distinguished: (1) saturation current of the Shockley equation and (2) junction breakdown or breakdown voltage. The vertical line corresponds to the maximum reverse bias voltage at which the sensor can be operated. (b) Good strips, the total number of strips of each sensor is 11.

As detailed previously, in each wafer, there are three sensors (T_1, T_8, and

T_{10}) type T, without the implantation of the gain layer in any of the 11 strips. Those sensors are the ones produced for testing with carbon ions and for FLASH-RT. It was selected a group of those detectors to measured the I-V in each of the 11 strips in order to check the behavior of the entire sensor before testing with carbon ions or/and for FLASH studies. A simple I-V of a PiN sensor (Wafer 10, T_1) is shown in Fig. 2.13a. Two different zones are distinguished in Fig. 2.13a, the region 1, in which the leakage current after the depletion of the sensor (in this case is necessary only 1 V to fully depleted the sensor) oscillate around the saturation current of the Shockley equation, as explained in Chapter 1. The value depends on doping concentration, diffusion constant, and depletion width. Additionally, the reverse saturation current is strongly affected by impurities and defects, which can increase it by orders of magnitude. In region number 2, the internal electric field inside of the detector is high enough that start an uncontrolled avalanche process (breakdown). Only one strip of 187 measured did not reach 160 V (see Fig. 2.13b), then was labeled as a bad strip. Therefore, 99.5% of the strips tested were good strip, representing the 94% of validated sensors.

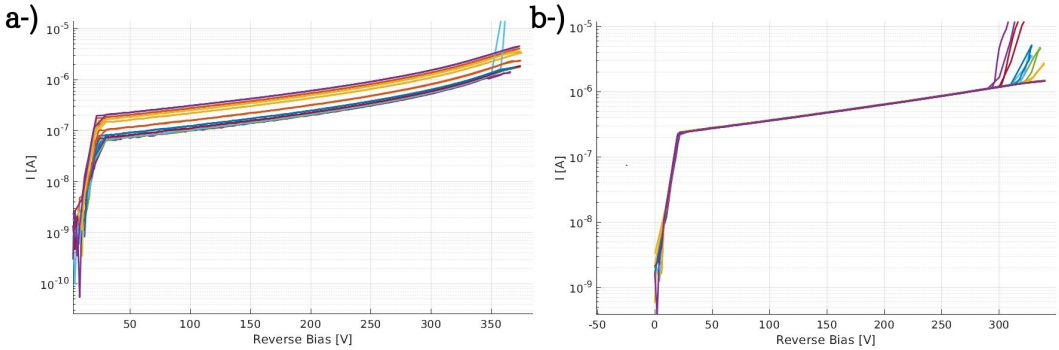

FIGURE 2.14: (a) Leakage current as a function of the reverse bias voltage in each LGAD strip of sensor 5-18 of wafer 4 (p-gain dose: 0.96 (a.u), Carbon Dose: A (a.u), total thickness: 70 μm). (b) Leakage current as a function of the reverse bias voltage in each LGAD strip of sensor 5-18 of wafer 7 (p-gain dose: 0.98 (a.u), Carbon Dose: B(a.u), total thickness: 70 μm; In both detectors the active thickness is 55 μm. These sensors belong to the UFSD3 production. More details can easly found in (Ferrero et al., 2021).

The results reported until now are from the sensor production MoVe-IT 2020. In the following Chapters, some results will be presented in which it was used two sensors from a previous production called UFSD3 (Ferrero et al., 2021). In general, the sensor's total thickness, considering the handle wafer, is about 600 μm, which can produce some beam perturbation. Therefore,

some sensors from the production UFSD3 were thinned to 70 μm to reduce the multiple scattering effects. This total thickness allows a tiny beam perturbation comparable to 250 μm water equivalent thickness when two sensors are placed in a telescope mode. The I-V carried out using the experimental setup described in section 2.3.1a in the two sensors used during this thesis is shown in Fig. 2.14. The breakdown voltage measured was 340 V and 280 V for sensors 5.18 of wafer 4 and wafer 7, respectively.

2.6.4 Capacitance measurements and evaluation of the acceptor doping profile of sensor type E

The measurements of the capacitance as a function of the bias voltage allows to evaluate the acceptor doping profile of the sensor.

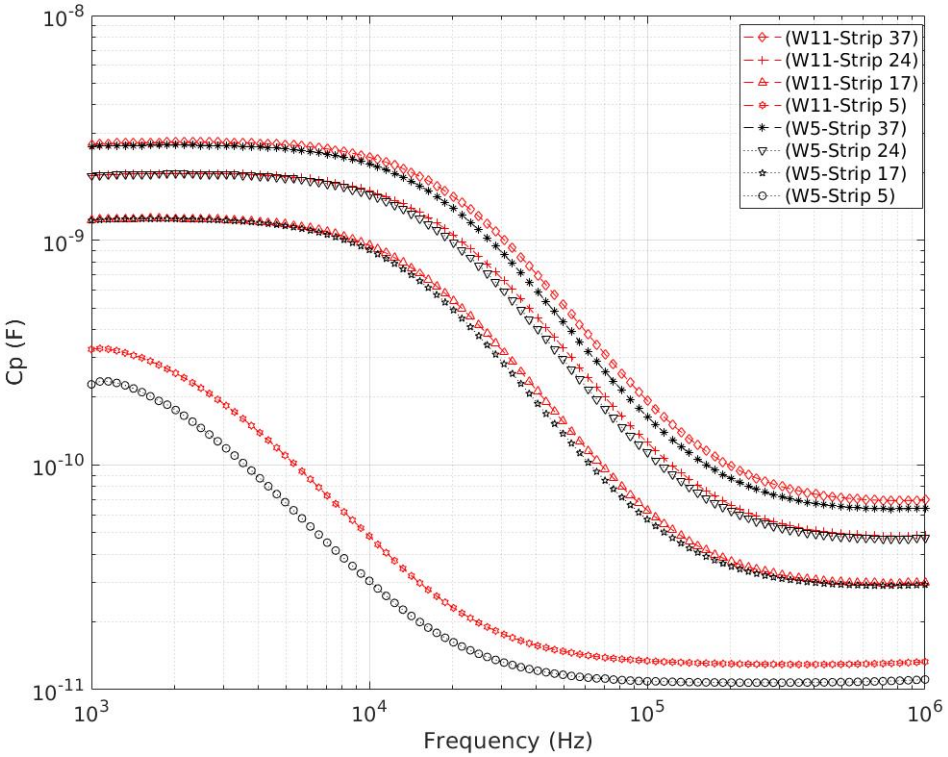

FIGURE 2.15: Capacitance vs. Frequency for wafer 5 and wafer 11 for strips with different dimension.

These measurements were performed using the setup and the methods described in section 2.4 and the test sensors type E (see Fig. 2.1b and Fig. 2.2) which contains strips of the same length as those in sensor type A but with different widths. In order to select the optimal frequency for the capacitance

Strip(Wafer)	Metal dimension (μm^2)	Capacitance fall-off (Frequency (Hz))
5 (W11,W5)	160x26260	1080, 1070
17 (W11,W5)	340x26260	1747, 1629
24 (W11,W5)	520x26260	2154, 2009
37 (W11,W5)	700x26260	2310, 1873

TABLE 2.4: Dimension of the strips of the sensor type E together with the value of the cut-off frequency. The two values of frequency reported for the same strip correspond to the wafers 11 and 5.

measurements, a scan of the capacitance as a function of the frequency of the AC signal was performed for four strips of different widths, as reported in Table 2.4, for two sensors from wafers 5 and 11 partially depleted with a reverse bias voltage of 10 V. The results are shown in Fig. 2.15. The fall-off in the capacitance with the frequency is due to the low-pass filter behavior of the strip, which can be modeled as a series cells made of a capacitor for the depleted region and a resistor for the strip metallization.
The cut-off frequency, defined as the minimum frequency when the numerical first derivative of the C-f curve is less than zero, is reported in Table 2.4 for strips of different widths. It shows lower values for strips with smaller width, as expected due to the increased resistance of the metal path where the AC signal propagates. For the following measurements, the minimum frequency value selectable in MF-CMU unit of 1 kHz was chosen, corresponding to the plateau region of the C-f curve for all the strips except for the strip 5, with the smallest width, which was not considered further, due to it was not possible to choose the proper frequency. Once the optimal frequency was fixed, the capacitance was measured as a function of the reverse bias voltage for strips: 17, 24, and 37. The results are shown in Fig. 2.16 for three wafers of group II and four wafers of group III. Increasing the reverse bias voltage, a slow drop in capacitance is seen which corresponds to the depletion of the gain layer, followed by a fast depletion of the bulk and a constant capacitance when the sensor is fully depleted. The capacitance is directly proportional to the active area of the strip and this explains the three different families of curves in Fig. 2.16, corresponding to the larger area (strips 37) in the upper curves and the lower area (strips 17) in the lower curves. The full depletion voltage and the bulk depletion voltage were determined using the procedure described in 2.4.1 and the average values are reported in Table 2.5 separately

for sensors of Group II and III. The V_{FD} values determined with the I-V measurements are also added for comparison, showing a good correspondence. As expected, V_{FD} for Group III is about 1 V larger than for Group II because of the doping concentration of the gain layer being about 2% higher. The V_{BU} is similar for both groups because of the same resistivity of the bulk. From the C-V curves, one can extract the acceptor doping concentration as a function of depth, as explained in (Sola et al., 2019). The results for strip 37 of the test sensors are shown in Figure 2.17, showing a very good uniformity between different wafers of the same group. The origin of the x-axis corresponds to the n^{++}/p^{+} junction where the depletion starts. The peaks, which are found at a depth of 0.5-1 μm , represent the gain layer implanted below the n^{++} electrode. The bulk is the nearly flat region and the sharp increase in doping concentration on the right is the p^{++} electrode.

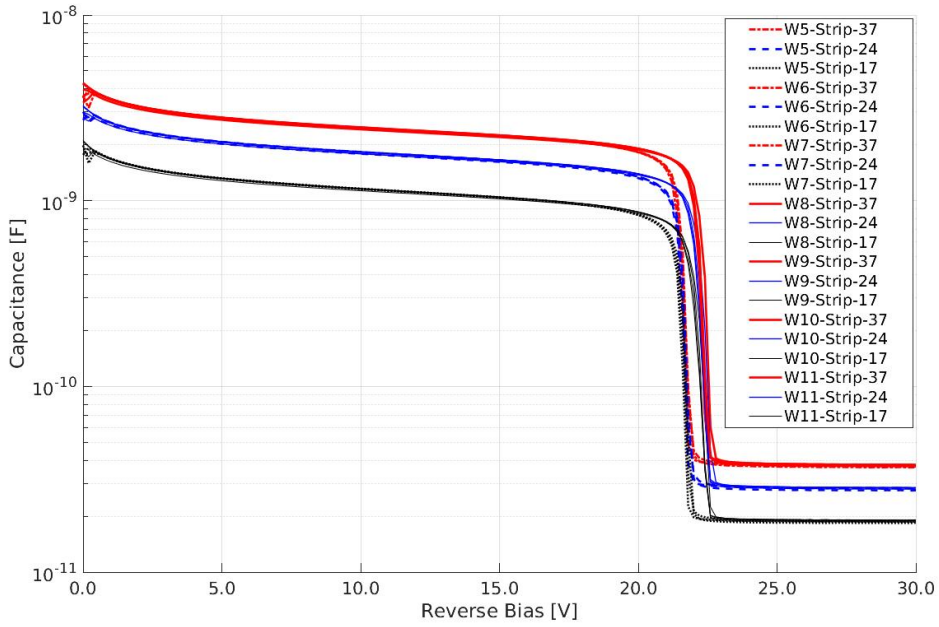

FIGURE 2.16: Capacitance vs. reverse bias voltage for different wafers and strips with different dimensions in semi-logarithmic scale. The dashed lines represent the strips from the wafers of Group II, while the solid lines are for Group III.

Interestingly, wafer 9 shows slightly deeper (0.03 μm) gain layer implant with respect to the gain implant of wafers of the same group (8, 10, and 11). This can explain the behavior observed before in Fig. 2.9, where the leakage current for the wafer 9 was over 2 times larger than the wafers in the same group. The shift in the peak depth may be due to a fluctuation of the implantation energy or to a variation in the dose of the n^{++} electrode. This results in a

Wafer	Bulk depletion voltage (V)	Full depletion voltage from C-V (I-V) curves
Group II	1.5 ± 0.3	22.4 ± 0.3 (22^{+4}_{-0})
Group III	1.6 ± 0.4	23.0 ± 0.4 (24^{+0}_{-2})

TABLE 2.5: Average bulk depletion and full depletion voltage measured from the C-V curves. Results from I-V curves are added for comparison.

slightly shallower and less doped layer, which produces a more significant depleted distance increasing the gain and shifting the peak of the doping curve deeper in the device.

2.6.5 Measurements of the inter-strip dead region of sensor type E

The measurements were performed as described in section 2.5. An example of signal amplitudes in two adjacent strips (arbitrarily named as "V" and "W") as a function of the position of the laser spot is shown in Fig. 2.18a. The inter-strip distance is defined as the distance between the 50% of the maximum of two S-curves which interpolate the data. This quantity was measured for three different bias voltages below the sensor breakdown and 4 different laser intensities to reproduce the energy released by the proton beams with clinical energies. The results are reported in Fig. 2.18b. The mean inter-strip distance, equal to 80.8 μm, is 22% larger than the nominal distance between the gain layers of the two strips (66 μm). This originates from the non-complete charge collection in the transition region between the periphery of the gain layer and the adjacent JTE implant (Paternoster et al., 2021). Finally, a small decrease of the inter-strip distance with the increase of the laser intensity, 3 % at most, was found for the three bias voltages used, as shown in Fig. 2.18b.

2.6.6 Beam test

A validated sensor from wafer 1 was tested with clinical proton beam at CNAO (Pavia, Italy). The sensor was glued on a PCB designed for housing the digital front-end readout (Fausti et al., 2021). However, the board allows acquiring the two analog signals from the strip 1 (PiN) and the strip 146 (LGAD), located at the opposite edges of the sensor at a distance of 2.6

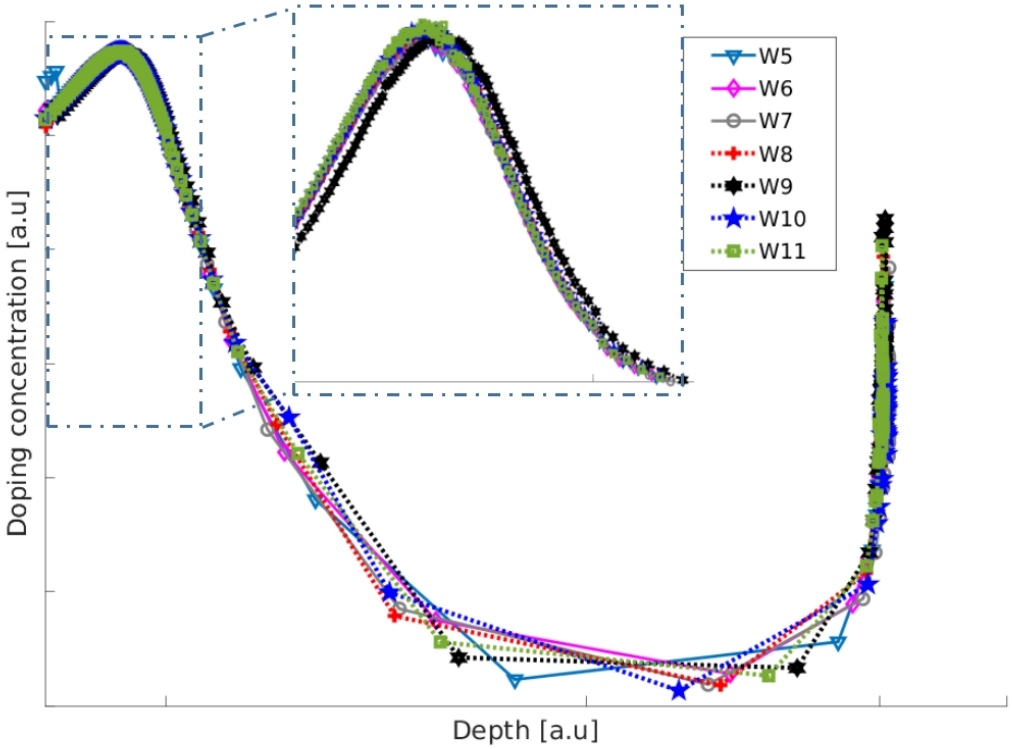

FIGURE 2.17: Doping concentration as a function of depth in logarithmic scale. The insert, corresponding to a magnified portion of the curve around the peaks, shows the tiny deviation of the doping profile of wafer 9.

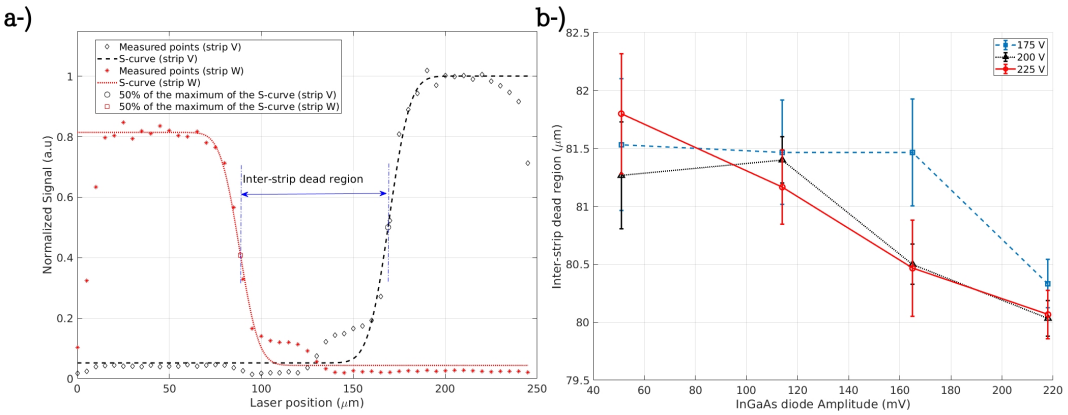

FIGURE 2.18: (a) Example of the normalized signal (in arbitrary units) for different laser position along the strip. (b) Measured inter-strip distance for different laser intensities, ranging from 2 to 6 MIPs, and bias voltages.

cm, thus allowing to perform studies of the signal shape. The sensor was aligned to the beam and the two signals were fed to two independent low-noise current amplifiers (CIVIDEC C2, 40 dB gain and 2 GHz bandwidth) which outputs were acquired by a 5GS/s digitizer CAEN DT5742 [9], featuring 12 bits resolution with 1 ADC corresponding to 0.24 mV. Each acquisition event consisted in a waveform of 1024 samples for a total duration of 204.8 ns. A PC connected to the digitizer through a 80 MB/s optical link was used to control the acquisition, collect the waveforms for the offline analysis and generate an asynchronous software trigger when the previous event was stored in memory.

The analog signal shape was studied for a nominal beam flux (although it should be taken into account that the sensor was centered to the beam, but the reported measurements are related to strips at the edge of the sensor) with the lowest beam energy of 62.28 MeV provided by the facility. The reason for this choice was to maximize the rate of protons hitting the two strips by selecting the beam energy providing the maximum pencil beam FWHM, 2.2 cm in air at the isocenter (Mirandola et al., 2015)

Fig. 2.19a shows an example of the signal measured in the two strips by 62.28 MeV protons using a reverse bias voltage of the sensor of 180 V in a time window of 410 ns, representing two waveforms acquired by the digitizer. Sharp peaks with a signal duration of approximately 3 ns, well separated from a constant baseline, can be observed in the LGAD strips, whereas the peak separation is much less pronounced in the PiN strip. The peak amplitude distribution, after subtraction of the baseline, is shown in Fig. 2.19b for the two strips. The good separation between signal and noise achieved in the LGAD strip allows counting the protons by selecting the optimal signal threshold while for the strip without gain the signal cannot be efficiently separated from the noise. The data for the LGAD strip was fitted using a convolution between a Gaussian and Landau distribution (The langaus distribution, see Chapter 1). The Most Probable Value (MPV) obtained from the fit is 379.5 ADC, corresponding to an amplitude of 91.08 mV. In addition, the noise standard deviation was 22.9 ADC (5.50 mV), which implies a signal-to-noise ratio of around 17.

Fig. 2.19b shows the results for 62.28 MeV protons with the highest possible Linear energy transfer (LET) for the clinical scenario. Assuming Pencil Beam Scanning (PBS) for 230 MeV, the signal's amplitude is expected to be about 2.5 times lower than for 62.28 MeV. Therefore, if we observed Fig. 2.19b, when

[9] https://www.caen.it/products/dt5742/

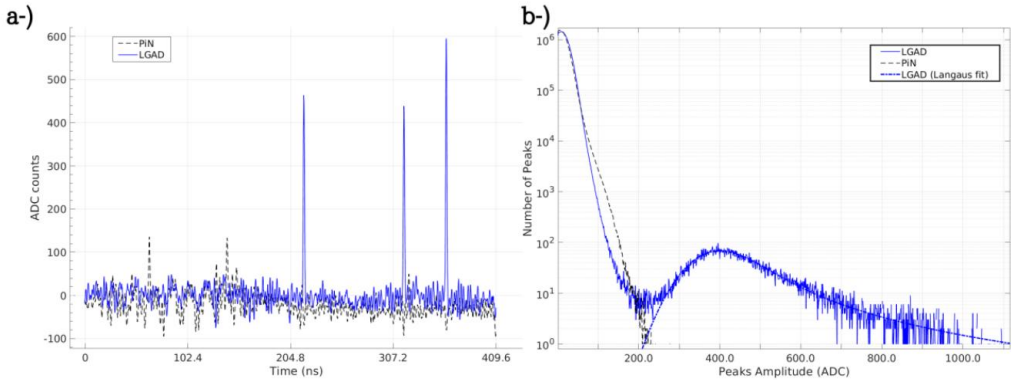

FIGURE 2.19: (a) Signals produced by 62.28 MeV protons in 45 thick strips silicon detector. (b) Number of peaks vs. peaks amplitude for protons with an energy of 62.28 MeV and using a reverse bias voltage of 180 V.

the MPV is 379.5 ADC (91.08 mV) for 62.28 MeV, the hypothetical MPV for 230 MeV is 153 ADC (36.72 mV). Accordingly, in the present configuration, the MPV of the Landau distribution is superimposed on the noise, being possible to see only the tail of the Landau.

It is crucial to note that the reverse bias voltage used during the measurements was 180 V, which allowed a sensor gain of approximately 6. The sensor gain increases exponentially with reverse bias voltage. Therefore, by increasing the reverse bias voltage (considering that "shot noise" does not worsen the SNR), we can enhance the protons signals and thus discriminate them. Finally, the sensor used during the beam test has the lowest gain of our production; a shift in the MPV of the Landau distribution (Fig. 2.19b) to the right is expected when testing a sensor, for example, from Group III.

As observed in Fig. 2.19b, with a thin PiN diode is not possible to detect the protons properly due to the small amplitude of the signals. Therefore, those detectors are not suitable for counting and timing applications in proton therapy. It is straightforward the benefits of using LGAD technology in proton applications, which has improved in the last few years (Arcidiacono et al., 2020). First, the signal is fast (order of fews ns) and large enough, allowing single proton detection capabilities in the clinical range. Those signals permit obtaining a time resolution of tens of ps, consequently optimal for energy measurement using ToF technique as reported by (Marti Villarreal et al., 2021; Vignati et al., 2020a).

Chapter 3

Direct energy measurements of particle beams using ToF

3.1 Introduction

Nowadays, the accuracy of the extracted beam energy in proton therapy treatments is guaranteed by safe checks of the accelerator settings and routine quality assurance measurements. However, none of the current technologies allows measuring the beam's energy during treatment (Giordanengo and Palmans, 2018). The energy of the beam determines the depth of penetration in the tissue. Therefore, the benefit of a detector that can assess the beam's energy during irradiation is straightforward. This chapter will describe the telescope system proposed by the University of Turin and the National Institute of Nuclear Physics (Turin Section)(Vignati et al., 2020a). It exploits the high time resolution of the Ultra-Fast Silicon Detectors (UFSD) technology to measure the energy of clinical proton beams in a few seconds using a system made of a telescope configuration aligned with the beam at a fixed distance. It is important to clarify that UFSD is a Low Gain Avalanche Detector (LGAD) optimized to achieve excellent temporal resolution. Therefore, in this thesis we refer to LGAD and UFSD as the same. The proposed system has been tested in the Trento Proton Therapy Center (cyclotron) and in the CNAO (synchrotron) and the results will be presented and discussed as well.

3.2 Energy measurement using Time of Flight technique

The methodology used to measure the time of protons crossing the known distance (x) in the air is described in detail in (Galeone, 2019; Vignati et

al., 2020a), and summarized in this section. Fig. 3.1 shows the simplified schematic of the telescope structure made by S_1 and S_2 with a thickness (t) placed at a known distance (x).

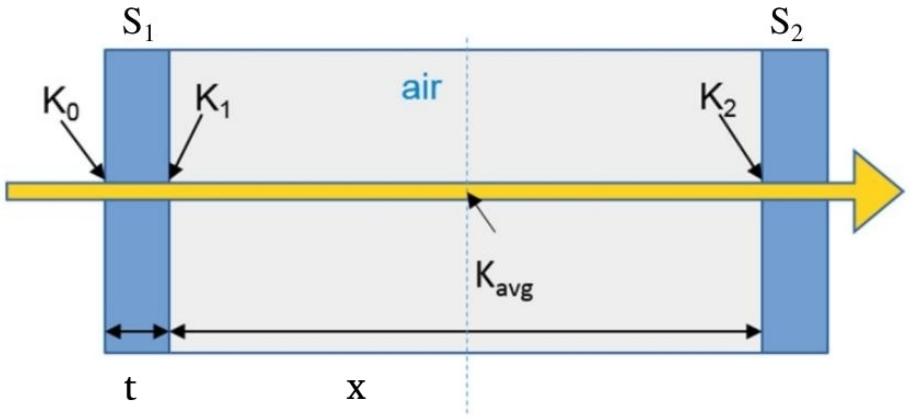

FIGURE 3.1: Schematic representation of two UFSD sensors (with thickness t) in a telescope configuration placed at a known distance x. Pictures adapted from (Galeone, 2019).

The time of arrival (dt) of each proton in S_1 and S_2 is measured using constant fraction discriminator (CFD) algorithm in order to reduced time walk effect. This method set the arrival time in a fixed fraction of the maximum signal amplitude, in our case it was used 80% to allow the time calculation even in the case of pile-up signals. The basis of our approach is based on coincidence signals, which are the signals generated by the same proton when passed through S_1 and S_2 as shown in Fig. 3.2. For example, to determine a probable coincidence signal, a peak higher than a threshold (green dash-line in Fig. 3.2) in S_1 needs to be identified, consecutive to that a search time window (yellow band in Fig. 3.2) is open for several nanoseconds in S_2. All the peaks higher than a predefined threshold within the search time window found in S_2 are considered as a coincidence and its corresponding time difference, obtained using CFD, is reported in a histogram. An example of the histogram of the reported time difference of the identified coincidence is depicted in Fig. 3.3 for the case of the proton beam at CNAO. Two different types of coincidences are appreciated in Fig. 3.3, and they are called: true coincidence and false coincidence. The true coincidence follows a Gaussian distribution and is generated by the same proton. This distribution is overlapped with a practically flat distribution which represents false coincidences and increases quadratically with the beam flux. The latter depends on the beam temporal structure (continuous or bunched) and is caused by

coincident signals which actually were not generated by the same proton. A fit of the sum of two Gaussian distributions is performed to the histogram (blue curve in Fig. 3.3), resulting in a Gaussian curve for the true coincidences (green curve in Fig. 3.3) and a second Gaussian curve for the false coincidences (purple curve in Fig. 3.3).

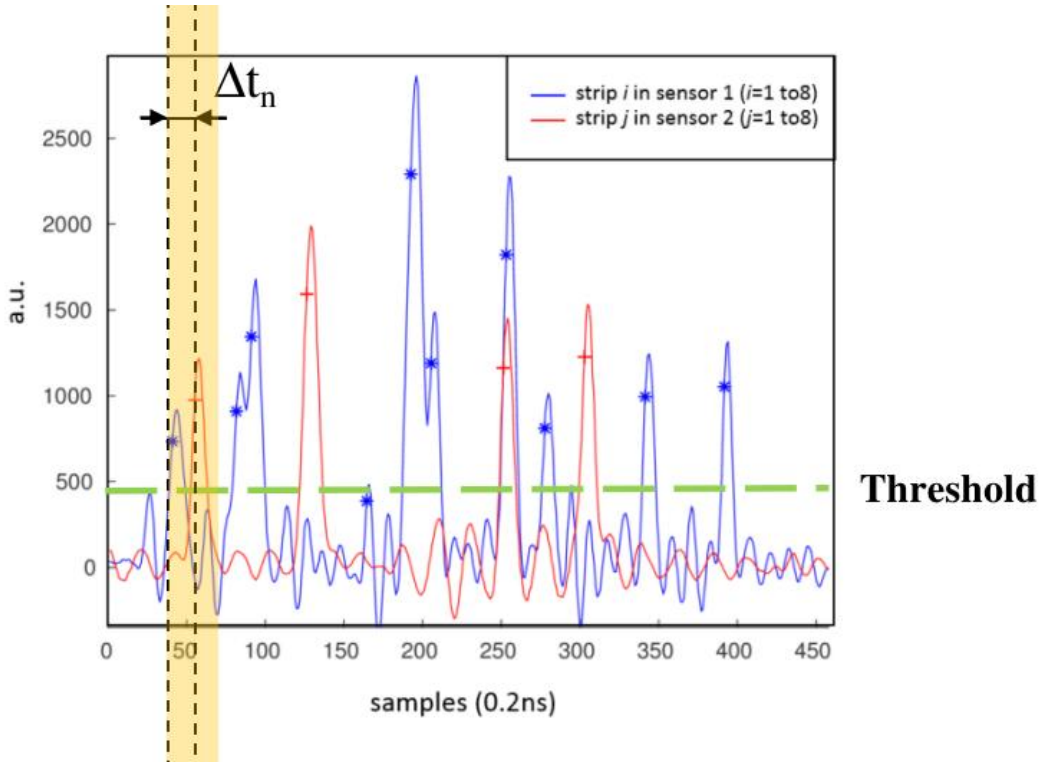

FIGURE 3.2: An example of an acquired waveform with the digitizer when can be observed the coincidence signals with their respective time difference using CFD. The green dashed line is the threshold. The yellow band is the search time window.

Finally, a second fit is performed to the histogram using a single Gaussian distribution to refine the final Δt_{mean}. It is applied only in the region near to the mean value extracted from the previous fit within two standard deviations of the true coincidence. All of this is performed after removing the combinatorial background (red curve in Fig. 3.3, using the previous fit. Therefore, knowing the mean time difference between the coincidence signals, with the procedure described before, the Time of Flight (ToF) of the protons for a specific energy is:

$$ToF = \Delta t_{mean} - t_{offset} \tag{3.1}$$

Where: t_{offset} is the time offset given by the electronic chain. The time offset is obtained by using a proper calibration (Vignati et al., 2020a). Because of the

systematic errors of the experimental setup (mainly due to the uncertainty on the distance between the sensors and the time offset given by the electronic chain), a calibration procedure is required.

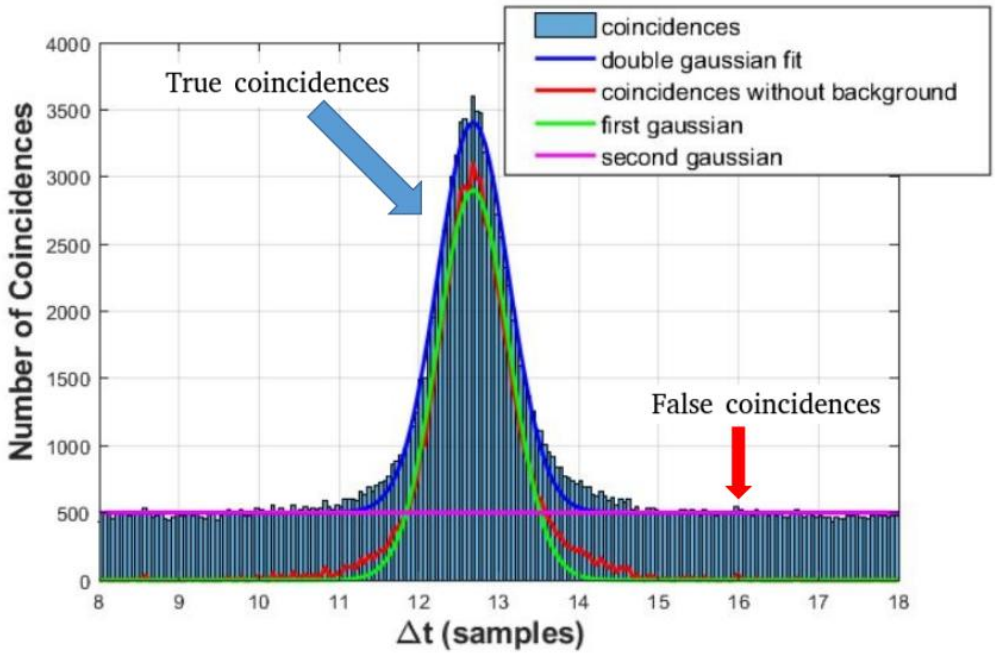

FIGURE 3.3: Example of Δt distribution for a proton beam of 182.75 MeV and 40 cm between sensors.

To that aim, two methods were developed to calibrate the system. The first one is based on a Chi-square minimization procedure (see Eq. 3.2, (Vignati et al., 2020a)) and it was used to calibrate the system in the beam test performed at Trento Proton Therapy Center (PTC), in terms of time offset and distance between the sensors (free parameters), starting from a priori knowledge of several values of beam energies and taking into account the energy loss in the first sensor and in air.

$$\chi^2(t_{offset}, d_j) = \sum_i \sum_j \left(\frac{(\Delta t^{i,j}_{mean} - t_{offset}) - ToF(K_i, d_j)}{\sigma_{i,j}}\right)^2 \tag{3.2}$$

Where: the subscript i, j are the number of distances and energies used respectively for the calibration and the variance $\sigma^2_{i,j}$ is given by the addition in quadrature of the statistical error on $\Delta t^{i,j}_{mean}$ and the uncertainty on $ToF(K_i, d_j)$.

$\Delta t_{mean,ij} - t_{offset}$ is the measured ToF (see Eq. 3.1) and $ToF(K_i, d_j)$ is the expected time of flight, which is given by:

$$ToF(K_i, d_j) = \frac{(K_i + E_0)d_j}{c\sqrt{(K_i + E_0)^2 + E_0^2}} \tag{3.3}$$

Where: d_j, c, and E_0 are the known distance between the two sensors S_1 and S_2, the speed of light in vacuum, and the proton mass energy at rest, respectively. In Equation 3.3, K_i is the nominal beam kinetic energy which is corrected for the energy loss in the first detector and in air. As can be appreciated, the weakness of this method lies in a priori knowledge of the nominal energy, and in the hypothetical use of this device as a commissioning of a new proton therapy center, where nothing is known about the energy of the beam is a problem its fidelity.
It is well known that the average proton velocity (v), in the traverse distance x between the two detectors is given by:

$$v_{avg} = \frac{x}{ToF} \tag{3.4}$$

Thus, the protons average kinetic energy K_{avg} from which is obtained the mean velocity v_{avg}, is located in the middle point between both sensors (see Fig. 3.1) under the assumption of constant air stopping power between them. It is important to point out that the dependence between the velocity and kinetic energy is not linear. However, due to the energy lost by the proton it is very small compared to the beam energy in the clinical range, the approximation is very accurate in the clinical range (Galeone, 2019). In fact, it was verified through Monte Carlo simulation that for the lowest energy used in clinics (about 60 MeV, the extreme case), the energy lost in a 1-meter distance between sensors is around 1 MeV. Then, K_{avg} is determined using the following equation:

$$K_{avg} \approx E_0 \times \left(\frac{1}{\sqrt{1 - \frac{{v_{avg}}^2}{c}}} - 1\right) \tag{3.5}$$

And K_0 (see Fig. 3.1) which is the energy at the isocenter is obtained as:

$$K_0 \approx K_{avg} + \left(\frac{S}{\rho}\right)_{air} \cdot \rho_{air} \cdot \frac{x}{2} + \left(\frac{S}{\rho}\right)_{Si} \cdot \rho_{Si} \cdot t \tag{3.6}$$

Where: ρ_{air} and $\rho_{silicon}$ are the densities of air and silicon, respectively, t is the thickness of S_1, x is the distance between S_1 and S_2. $(\frac{S}{\rho})_{Si}$ is the mass stopping

Material	y	A	q
Silicon	0.9438	265.1	0.8669
Air	1.060	316.5	0.8847

TABLE 3.1: Values of the parameters of Eq. 3.7 for air and silicon estimated from the exponential fitting of empirical data.

power in silicon at the energy K_1, which is expressed as $K_{avg} + (\frac{S}{\rho})_{air} \cdot \rho_{air} \cdot \frac{x}{2}$. The $(\frac{S}{\rho})_{air}$ is the mass stopping power in air at the energy K_{avg}. It was used the PSTAR[1] dataset for determining $(\frac{S}{\rho})_{Si}$ and $(\frac{S}{\rho})_{air}$.

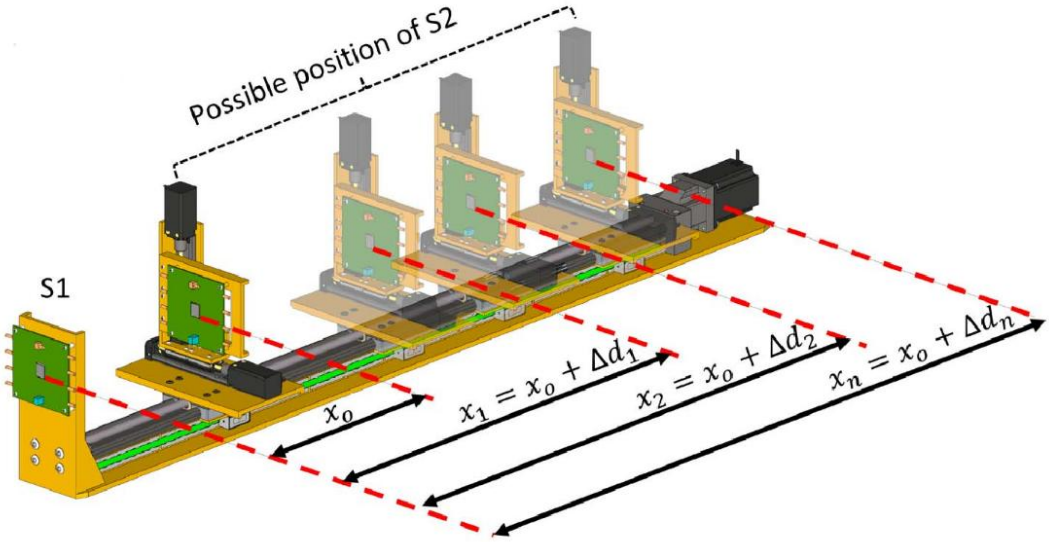

FIGURE 3.4: Schematic representation of the mechanical system where S_2 may be placed at variable distances x_i, ranging from 300 to 950 mm, with respect to S_1 (kept fixed at the isocenter). The first distance x_0 between sensors is affected by a significant uncertainty due to possible positioning errors and possible tilts of the different components while the relative displacements along the longitudinal axis are measured with an optical encoder. Picture taken from (Shakarami, 2021).

In addition, for obtaining the mass stopping power in air and silicon for all the kinetic energies, the following empirical parametrization was employed:

$$(\frac{S}{\rho}) = y + A \cdot K^{-q} \tag{3.7}$$

The values for y, A, and q used can be found in Table 3.1.
The second method developed to calibrate the system, which is under patent

[1] http://physics.nist.gov/PhysRefData/Star/Text/PSTAR.html

process (no further information can be disclosed) at the time of writing this thesis, it is based in the relative displacement (Δd_i) of S_2 with respect S_1, which is kept fixed at the isocenter as shown in Fig. 3.4. This method, called self-calibration approach, is independent from any priori knowledge of the values of nominal energy provided by the clinical facility. The latter method was the one used in this thesis to calibrate the system in the beam test at CNAO. Basically, the system used allows measures the position of S_2 with an uncertainty of 0.1 μm, thanks to an optical encoder. Consequently, the developed approach uses the Δt_{mean} extracted for different proton energies and positioning of S_2, therefore at different distances between the sensors. Then, it finds the best values for the position of the first sensor (x_0) and offset performing a minimization of the square deviation between the calculated and measured S_2 positions, where calculated ones are obtained by multiplying the average velocity and the ToF for a specific S_2 position and the measured ones are the S_2 positions obtained by summing x_0 to the specific relative displacement.

3.3 Materials & Methods

3.3.1 Silicon sensors & acquisition electronic chain

FBK manufactured dedicated sensors for ToF measurements (Type T) (see Fig. 2.1). The sensors tested at CNAO and PTC were the ones explained in section 2.6.3, and the I-V curves carried out to test the correct working of these sensors is shown in Fig. 2.14.

The selected sensors were wire-bonded to an 8-channel custom front-end board (see Fig. 3.5) for the measurements performed at CNAO. As can be seen, only strips 3 through 10 were limited to one of the eight channels of the custom front-end board. Whereas, the first two strips and the last one were grounded, because they were designed with an optical window for laboratory tests with a picosecond infrared laser, so they were not used in this study. From now on, to simplify the understanding of the results presented, the bonded strips will be referenced with the numbers from 1 to 8, which do not correspond to the actual numbering of the strips in the sensor.

The 8-channels of the custom front-end board are identical, each based on two stages of amplification using two Heterojunction Bipolar Junction Transistors (HBJT). The first stage (preamplification) is configured as collector

feedback biasing, extracting the current signals from the detector and converting them to voltage signals, the so-called trans-impedance amplifiers. In the second stage, the HBJT is configured with a fixed base, which further amplifies and shapes the voltage signal obtained from the previous stage to a voltage signal with a nominal gain of 100. It is important to point out that the signal is inverted in each stage of amplification (Royon and Minafra, 2021).

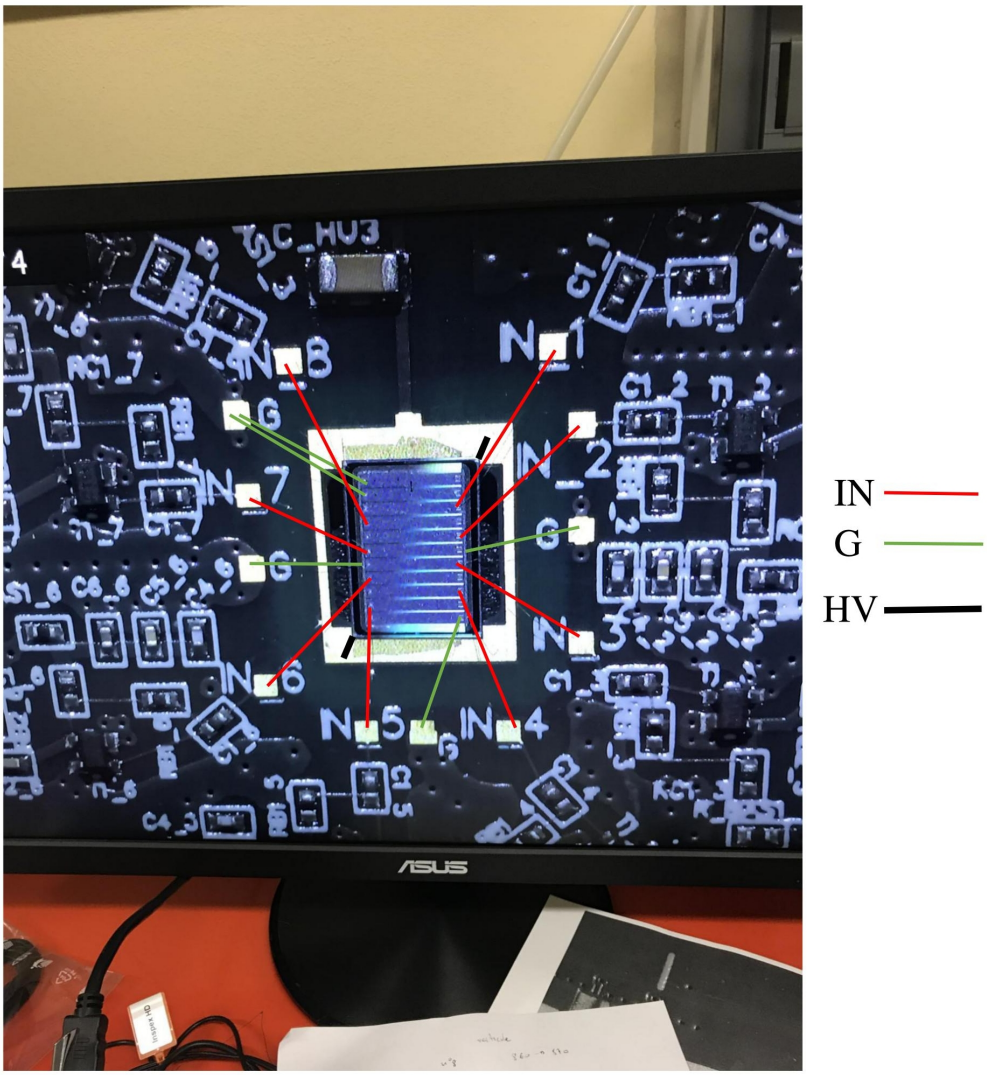

FIGURE 3.5: Picture of the wire-bonding of the front-end board with a sensor type T.

Instead, for the measurements performed at PTC the sensors were glued on high voltage (HV) distribution boards. The signals were amplified by a low-noise CIVIDEC 40 dB current amplifier. The outputs of the boards in both beam tests and in most of the acquisitions carried out in this thesis were acquired through the high rate CAEN digitizer model DT5742 (see Fig. 3.6). It

is based in the DRS4 chip (Domino Ring Sampler) designed at Paul Scherrer Institute (PSI, Switerland). The DRS4[2] chip contains a switched capacitor array (SCA) with 1024 cells (analog memory) which is capable of sampling 9 input analog channels continuously in a circular fashion with high speed (750 MS/s to 5 GS/s, which can be programmed to the desired sampling frequency). For instance, fixing a sampling rate in 5GS/s, the acquisition windows is 204.8 ns.

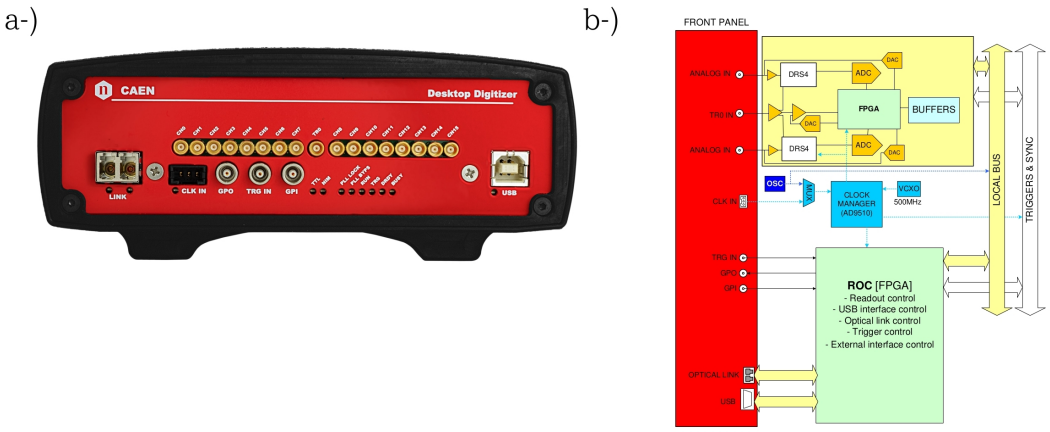

FIGURE 3.6: (a) Front panel view of the CAEN Digitizer model DT5742. (b) Block Diagram. Pictures taken from (DT5742, 2023-02-26).

As can be observed in Fig. 3.6a, the digitizer has in total 16 analog input channels on MCX coaxial connectors with an input impedance of 50 Ohms and a dynamic range of 1 Vpp (DC coupled) with a 16-bit DAC on each channel to control de DC Offset with a range of ± 1 V. The digitizer has two groups, named Group 0, from ch0 to ch7 and Group 1, from ch8 to ch15. Since the DRS4 can deal up to 9 channels, each group is sampled by a different DRS4 as despicted in Fig. 3.6b. It is important to note that the 12-bit ADC stage starts when the trigger condition is met. In this period, the trigger stops the DRS4 chip sampling, so the analog memory buffer is frozen, introducing an unavoidable dead-time. The dead-time is 110 μs if only the analog input is digitized and 181 μs when the fast trigger is digitized.
There are four types of triggers modes available in this digitizer:
-*Software trigger* : internally produced via software, common to all enable groups.
-*External trigger* : can be a TTL or NIM external signal (see Fig. 3.6a and Fig. 3.6b, labeled as TRG IN in the front panel connector). The motherboard

[2]https://www.psi.ch/en/drs

processes the trigger signal before sending it to DRS4 with a clock of about 58 MHz. This step introduces a latency of about 115 ns with a jitter of about 17 ns, making it impossible to use at 5 GHz.
-*Fast trigger* : the signal of this trigger is common for all the enable groups, is labeled as TR0 in the front panel connector (see Fig. 3.6a and Fig. 3.6b). It has a low latency (about 42 ns with a jitter of about 8.5 ns) compared with the external trigger. As can be seen in Fig. 3.6b, the TR0 signal is sent to a comparator with a programmable threshold that defines when the signal is sent to the DRS4 chips. This step has no motherboard processing and the output is sampled at 117 MHz. It is important to point out that the TR0 is split into the two DRS4 with two different paths as shown in Fig. 3.6b, introducing a small difference in the sampling time between the two groups.
-*Self trigger* : the signal of this trigger is common to all enabled groups. For each group it is possible to select combination of channels (logic OR) that provide a trigger whenever the input crosses the threshold. In this mode, 5GHz cannot be used due to the trigger latency which is about 250 ns. This model of digitizer has the possibility of using USB and Optical Link communication interfaces (see Fig. 3.6). In order to maximize the data transfer rate, the Optical link must be used over the USB 2.0 because it can reach 80 MB/s compared to 30 MB/s of the USB 2.0.

3.3.2 Measurements of the delay time between channels

Our telescope faces several challenges in measuring each proton's arrival time, mainly limited to the maximum error allowed on the ToF to obtain an energy error corresponding to 1 mm error on the depth in water. In each sensor, eight strips are read out with the front-end board (one channel per strip), which is connected to a digitizer model DT5742. This introduces an unavoidable time offset between channels affecting the assessing time of arrival of the protons. Therefore, it is essential to test the entire electronic chain before a beam test. An experimental setup, mainly consisting of an infrared picosecond laser with a wavelength of 1060 nm and a spot size with a diameter of about 1 mm, was used to assess the inter-channel delay, as shown in Fig. 3.7. In this configuration, simultaneously, the laser hit three neighboring strips at the same time, inducing a signal that is used to estimate the delay with respect the laser trigger. The laser trigger was fed into a PM5786B pulse generator, which later fed the fast trigger (TR0) in the digitizer. It is important to remark that the same electronic configuration was used later during

the beam test.

As explained previously, the fast trigger is divided into two paths inside the digitizer, introducing a slight difference ($\sim 600ps$) in the sampling time between the TR_{00} and TR_{01} triggers, which correspond to the two groups of the digitizer (see Fig. 3.8).

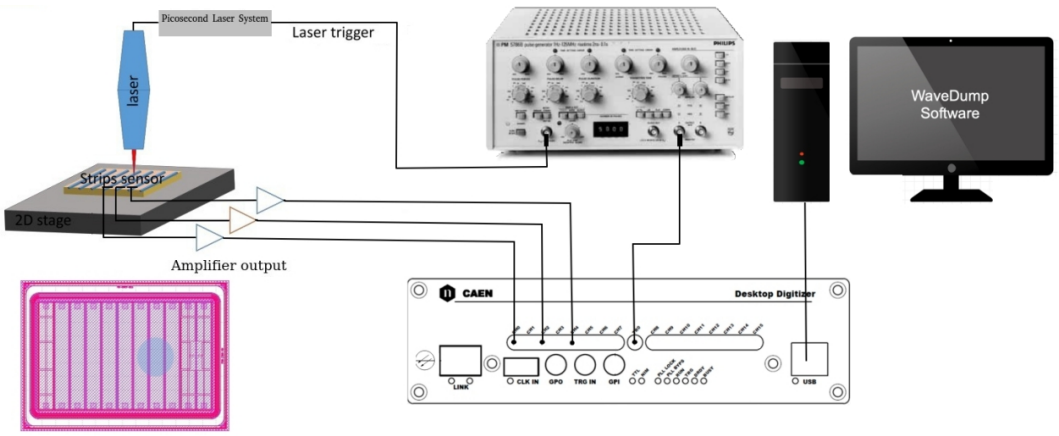

FIGURE 3.7: Experimental setup used to measure the delay between channels using an infrared laser.

The delay between channels was estimated as shown in Fig. 3.8, i.e., considering the time difference between the corresponding trigger (TR_{00} or TR_{01}) and the induced signals in the respective channels.

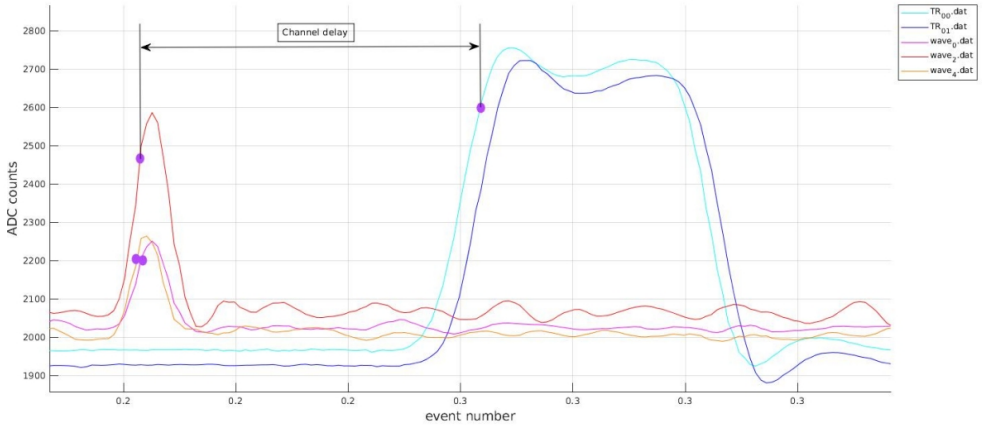

FIGURE 3.8: Signal output from the digitizer as a result of the laser input signal injected simultaneously on strip 1,2 and 3 in S_1. It shows also the shift between TR_{00} and TR_{01}. The signal induced in $wave_0$, $wave_2$, and $wave_4$, corresponds to strips 1, 2, and 3, respectively. The laser was focused on the strip 2.

For instance, for the digitizer channels: 0, 1, 2, 3, 4, 5, 6, and 7, Group 0, the

corresponding trigger was TR_{00}. Conversely, for digitizer channels: 8, 9, 10, 11, 12, 13, 14, and 15, Group 1, the corresponding trigger was TR_{01}. The time of the induced signals on each sensor and the trigger is determined using a constant fraction discriminator algorithm (CFD) at 0.80 of the maximum amplitude. The estimated Δt is obtained from a Gaussian fit time difference between the corresponding trigger and the channel. Fig. 3.9 exhibits the case when the laser hits strips 1, 2, and 3 simultaneously. It shows the number of coincidences versus the time difference in ns. As can be noticed, a 200 ps delay was observed between the strips 1 and 2 with the strip 3.

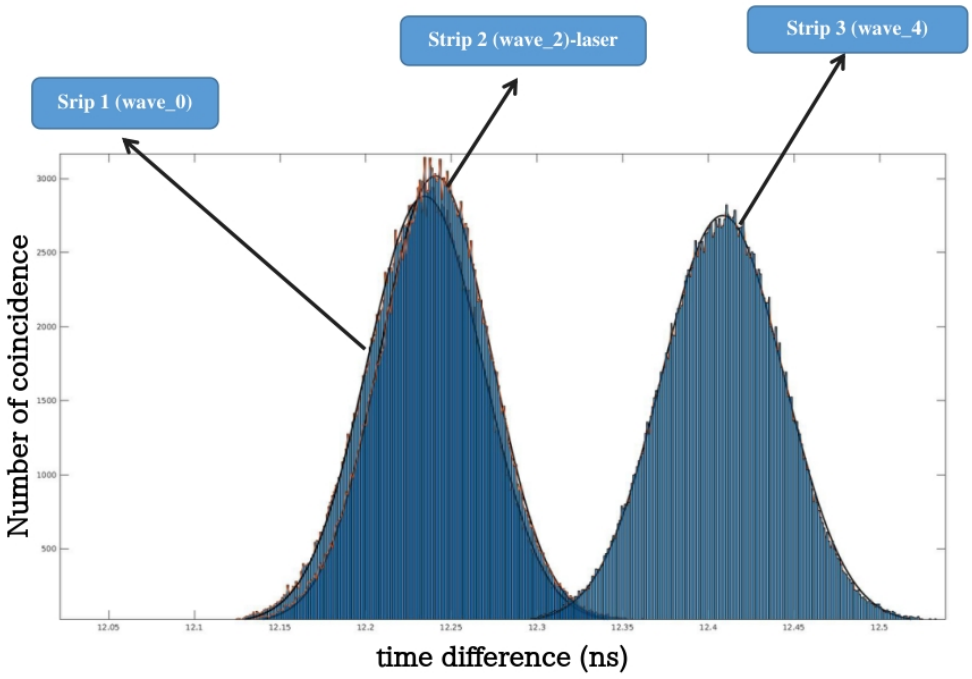

FIGURE 3.9: Number of coincidence as a function of time difference for strips 1, 2, and 3. The laser was focused on the strip 2.

The delay found for each channel of the two boards is shown in Tables 3.2 and 3.3 for boards 2 and 1, respectively. The data reported in those tables are extracted using the approach explained before and are shown in Fig. 3.10. Interestingly, both boards show the same trend, although there is a clear shift. The cables used in the acquisition were made in-house with a maximum difference between the same signal injected into two cables of about 30 ps. The values reported in Fig. 3.10 are affected by the wire-bond+front-end board channel+cables length+the digitizer channel. However, the main contribution to the reported values is the path travel by the signals in the front-end

Strip(Ch(B))	Ch(D)	G(D)	Δt_1	Δt_2	Δt_3	Δt_4	Δt_5	Δt_6	Δt_{mean}
1(1)	0	0	12.234						12.234
2(8)	2	0	12.241	12.287					12.264
3(2)	4	0	12.408	12.400	12.418				12.409
4(7)	6	0		12.435	12.423	12.455			12.437
5(3)	8	1			12.312	12.302	12.294		12.303
6(6)	10	1				12.319	12.314	12.292	12.308
7(4)	12	1					12.279	12.287	12.283
8(5)	14	1						12.215	12.215

TABLE 3.2: Measured $\Delta t(ns)$ for S_1-Board 2. It is calculated as $\Delta t_{trigger} - \Delta t_{channel}$.

Strip(Ch(B))	Ch(D)	G(D)	Δt_1	Δt_2	Δt_3	Δt_4	Δt_5	Δt_6	Δt_{mean}
1(1)	1	0	12.017						12.017
2(8)	3	0	12.140	12.173					12.156
3(2)	5	0	12.281	12.285	12.287				12.284
4(7)	7	0		12.317	12.284	12.318			12.306
5(3)	9	1			12.211	12.178	12.175		12.188
6(6)	11	1				12.206	12.181	12.177	12.188
7(4)	13	1					12.147	12.140	12.143
8(5)	15	1						12.068	12.068

TABLE 3.3: Measured $\Delta t(ns)$ for S_2-Board 1. It is calculated as $\Delta t_{trigger} - \Delta t_{channel}$.

board (see Fig. 3.5). Finally, the delay between each channel's combination is reported in Table 3.4. The number reported in each cell is calculated as the $\Delta t_{mean,strip,Board2} - \Delta t_{mean,strip,Board1}$. Those values were inserted in the analysis software[3].

Fig. 3.11a shows the Number of coincidences versus time difference (ns) without applying any correction factor to the signal acquired at CNAO for 400 cm between sensors and 68.74 MeV at the isocenter using the 32 combinations of strips shown in Table 3.4. As explained in (Vignati et al., 2020a), a Gaussian distribution for the true coincidence is expected. However, as can be noticed in Fig. 3.11a, the difference between channels leads to a deformed Gaussian distribution, which affects the measurement of the mean time difference and finally, the ToF calculation. On the other hand, when the correction factors of Table 3.4 are applied to the acquired data, a perfect Gaussian shape is obtained, showing that the correction factors obtained in the laboratory with an infrared laser are correct.

The reason for choosing 32 combinations between strips is to measure the

[3]https://github.com/omarti2504/ToF

	Board 2							
Board 1	**1**	**2**	**3**	**4**	**5**	**6**	**7**	**8**
1	0.217	0.247	0.392	0.420				
2	0.078	0.108	0.252	0.281				
3	-0.050	-0.020	0.125	0.153				
4	-0.072	-0.042	0.102	0.131				
5					0.115	0.120	0.095	0.027
6					0.114	0.120	0.095	0.027
7					0.159	0.165	0.140	0.072
8					0.235	0.241	0.215	0.148

TABLE 3.4: Delay between channels measured with an infrared laser. The number reported in each cell is calculated as the $\Delta t_{mean,strip,Board2} - \Delta t_{mean,strip,Board1}$.

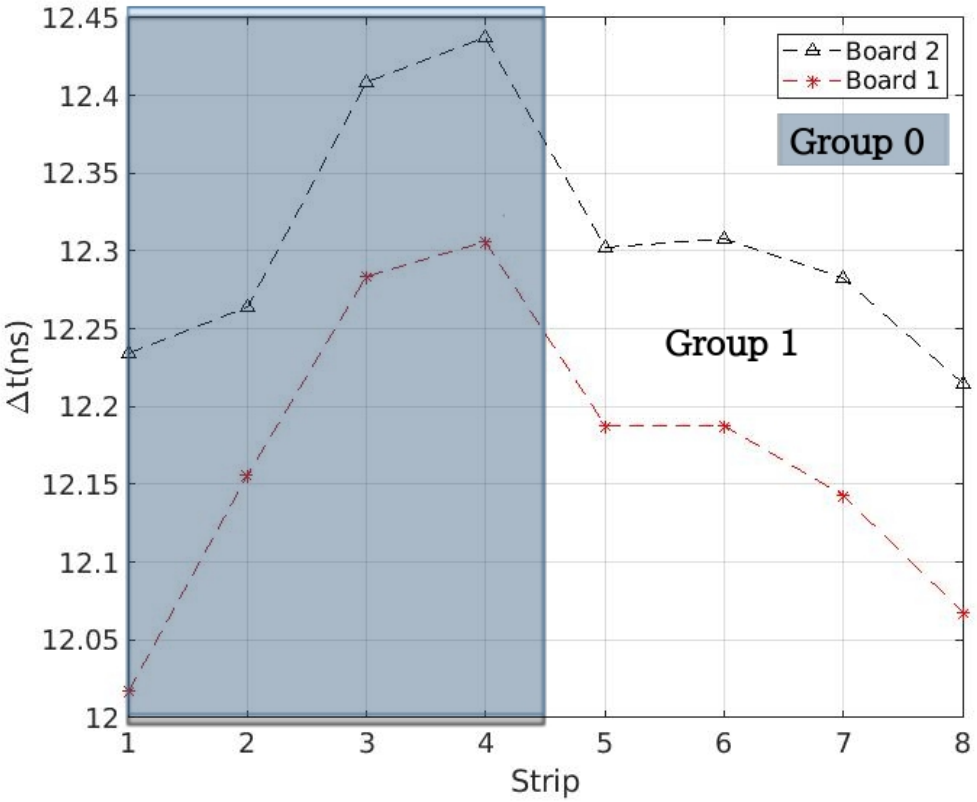

FIGURE 3.10: Δt_{mean} from Table 3.2 and Table 3.3 as function of the strips for the two sensors. S_2 was mounted in the Board 1 and S_1 in Board 2.

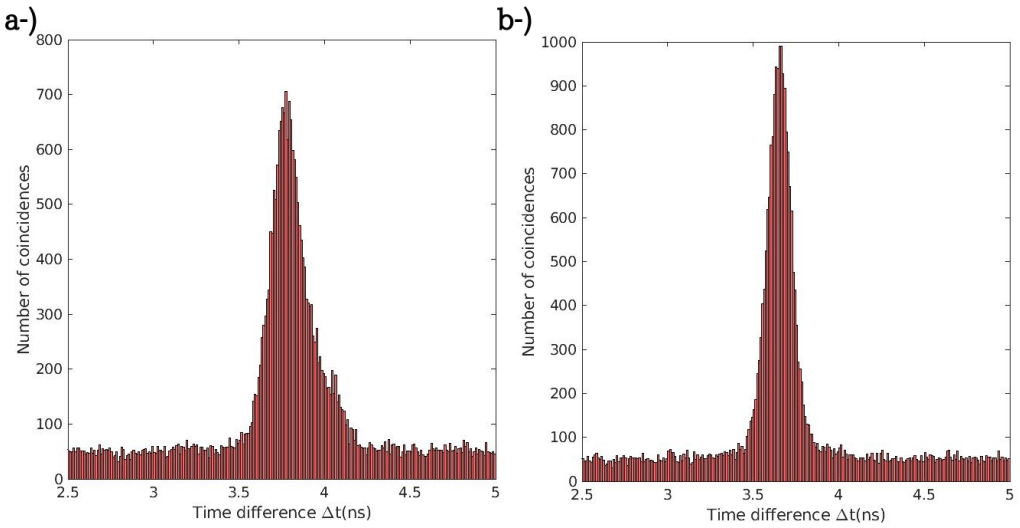

FIGURE 3.11: Example of the application of the time delay obtained in the laboratory with an infrared laser to the signal acquired at CNAO for 68.74 MeV at 40 cm between sensors. (a) No correction factor. (b) Correction factor of Table 3.4.

Δt using the same Group of the digitizer, avoiding using different groups where a correction factor is more complex because it is necessary to consider also a shift in time between TR_{00} and TR_{01}. Although the application of approximately 600 ps between the two groups will result in a wider Gaussian distribution which will degrade the time resolution of our system, which is not desirable.

3.4 Beam test at Trento Proton Therapy Center (PTC)

The beam test at PTC precedes in time the measurement performed at CNAO (reported in the next section). They were performed using the physics line of the experimental room in that facility, as shown in Fig. 3.12a. As described in section 1.3.1, the Trento proton beam is provided by a cyclotron which accelerates the beam to an energy of 228 MeV. Shortly after the cyclotron exit, a rotating degrader of different thicknesses and materials performs a coarse energy selection to reduce the beam energy reaching a minimum value of 70 MeV. The beam intensities at the extraction are ranging between 1 and 320 nA, modulated by a 50 percent duty-cycle square wave, with a 100 ms period.

For these measurements, the timing sensors (Fig. 3.12b, see section 2.6.3 for more details about the characterization in laboratory) were used. For the beam test, two sensors were glued on high voltage (HV) distribution boards

aligned to the beam and positioned at three distances (27, 67, 97 cm $\pm$ 0.1 cm) in a telescope configuration. Only 1 strip per sensor was readout.
For each of these distances, the ToF values were measured at 5-7 different beam energies between 68.3 to 227.3 MeV. These energies, retrieved from the PSTAR dataset according to the water equivalent depths at the isocenter provided by the facility are considered as nominal energies. The detectors' signals were amplified by a low-noise CIVIDEC 40 dB current amplifier, and acquired through the high rate digitizer CAEN DT5742. A PC connected to the digitizer with 80 MB/s optical link was used to control the acquisition, collect the waveforms, and produce an asynchronous software trigger when the previous events were stored in memory.

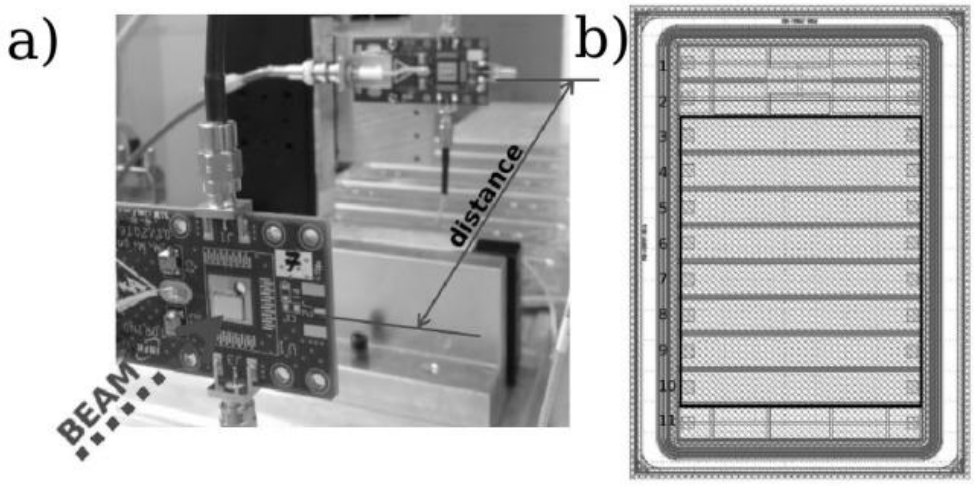

FIGURE 3.12: (a) Telescope of two UFSD strip sensors mounted on 2 channels high voltage (HV) distribution boards fixed in the mechanical support; the distance between the two sensors in the telescope configuration has been changed (27, 67, and 97 cm). (b) Technical drawing of an FBK UFSD segmented in 11 strips.

3.4.1 Energy calculation procedure

The methodology is described in details in (Vignati et al., 2020a) and in section 3.2, and here only briefly summarized. Fig. 3.12a shows the experimental setup used in the beam test. The time of arrival of protons on each sensor is determined using a constant fraction discriminator algorithm (CFD), and the estimated Δt_{mean} is obtained as the average of the differences of the times of arrival of same protons passing through the two sensors. Because of the systematic errors of the experimental setup (mainly due to the uncertainty

on the distance between the sensors and the time offset given by the electronic chain), a proper calibration procedure is required. A Chi-square minimization procedure was used to calibrate the system (Vignati et al., 2020a), in terms of time offset and distance between the sensors (free parameters), starting from a priori knowledge of several values of beam energies and taking into account the energy loss in the first sensor and in air.

3.4.2 Results

The achieved difference between the energy measured with the ToF technique after calibration and the nominal energy is shown in Fig. 3.13, where the large error bars are due to the precision of the water equivalent depth at the isocenter provided by the facility (Tommasino et al., 2017). For the largest distance used (d = 97 cm) and for all considered beam energies in the range 68.3 to 227.3 MeV, a root mean square deviation of 341 keV and a maximum deviation of 402 keV (corresponding to an energy difference within the range uncertainty clinically acceptable of 1 mm) were obtained. For 67 cm, an uncertainty larger than 1 mm was found at the two highest energies, as previously obtained in other measurements (Vignati et al., 2020a).

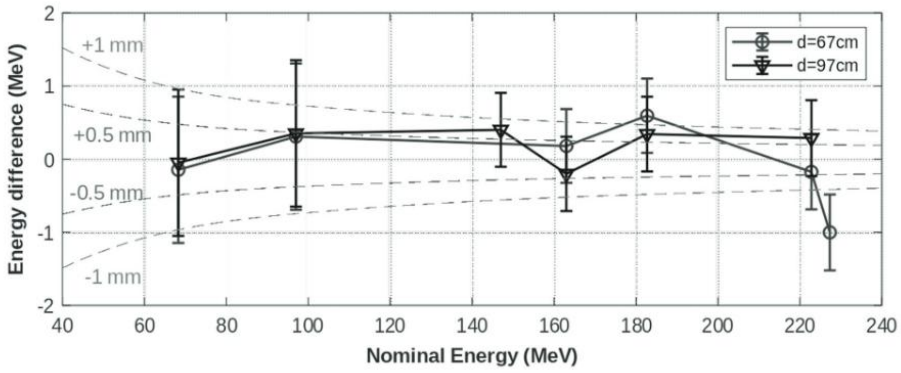

FIGURE 3.13: Deviations between the measured and nominal energy for different nominal energies at 2 distances between the sensors (67 cm (circles) and 97 cm (triangles)). The dashed lines represent the corresponding uncertainties in water range.

These results are well in accordance with the expectations, since for a flight distance of 1 m between the sensors, the maximum error allowed on the ToF to obtain an energy error corresponding to 1 mm in water ranges from 80 ps at 60 MeV to 4 ps at 230 MeV, and these limits are more stringent for reduced distances (Vignati et al., 2020a). The beam test was performed reading

out only 1 strip per sensor. Moreover, the data acquisition were not optimized. Due to the unavoidable digitizer conversion time of 110 μs and the additional dead time due to data transfer and saving ($\approx$ 500 μs), only a small fraction ($\leq$ 1 per mill) of the delivered particles were used for the analysis. Beam irradiation of less than 6 s (at therapeutic fluxes, $\approx$ 228 MeV proton beam energy, and at $\approx$1 m distance between sensors) was enough to collect a significant number of coincidences to keep the error on the ToF below the values needed to obtain the clinically required range uncertainty. Although further implementation (mainly focused on optimizing the acquisition chain) are still needed before application during patient treatments. The use of a larger sensitive area will increase the statistics and will promote rapid technology transfer to a commercial device, useful for beam commissioning and quality control measurements.
Using the detector prototype made of a telescope of two UFSD sensors to measure the beam energy of a therapeutic proton beam with ToF technique, a few hundred of keV of deviation from nominal energies were achieved for all energies for 97 cm distance between the sensors, corresponding to $\leq$ 1 mm range, as clinically required. The promising results demonstrate that UFSD could represent a viable option for new beam energy monitors, potentially able to measure online the beam energy during irradiation. New experimental setup based on the readout of 8 strips to increase the sensitive area together with a new movement stage to increase the positioning precision was tested at CNAO and the result will be presented and discussed in the next section.

3.5 Beam test at National Centre for Oncological Hadrontherapy (CNAO)

3.5.1 Experimental setup

Fig. 3.14 shows the updated version of the telescope system. It is composed by two LGADs placed at a relative distance from each other, hereinafter referred as S_1 and S_2. S_1 is held fixed at the isocenter by using laser pointers located in the treatment room while S_2 is controlled by three independent motors which allow the sensors to move in XYZ-axis. The system has an optical encoder model Renishaw Evolute EL26BBB500F10A which is used to

measure the displacement with a resolution of 0.1 μm of S_2 in the Z-axis. In this direction, S_2 can be moved at a relative distance from S_1 between 300 mm and 950 mm. The reason of the translation of S_2 in the XY plane is to allow the alignment of the system between the strips of S_1 and S_2.

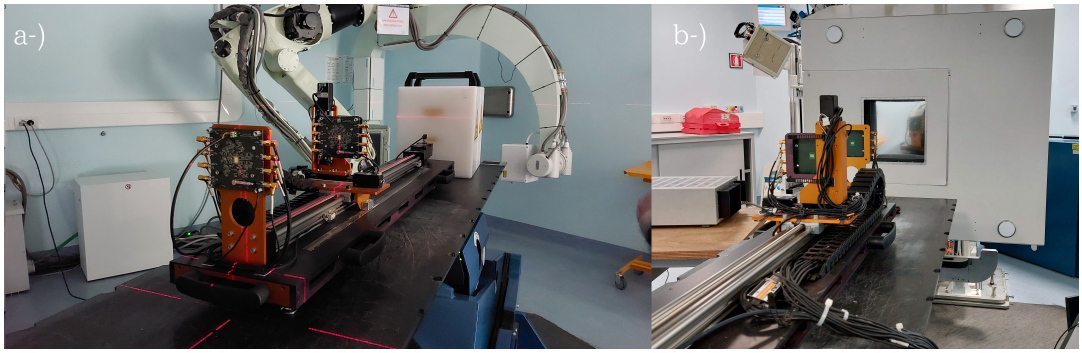

FIGURE 3.14: Experimental setup used at CNAO.

In the beam test performed at CNAO the detectors used were previously tested in the laboratory as explained in chapter 2, in order to guarantee the correct behavior of all the strips before the irradiation at the proton therapy center. It was decided to use two sensors from the production UFSD3 because those sensor were thinned down to 70 μm allowing a reduction of multiple scattering effects. More precisely, the selected sensor are type T and were the ones labeled 5.18 of wafer 4 and wafer 7 with a measured breakdown voltage of 340 V and 280 V, respectively (see section 2.6.3 for more details).
The selected LGAD sensors were wire-bonded to an 8-channel custom front-end board as explained before (see Fig. 3.5). Unlike the PTC beam test, where only one strip per sensor was read, in this case all 8 outputs from each board (16 signals in total) were connected to the high-speed CAEN digitizer (model: DT5742, 5 GS/s, 12 bits resolution, 1 ADC = 0.24mV, acquisition windows of 1024 samples, i.e. 204.8 ns). It was used a TTL signal coming from the accelerator to trigger the acquisition using the fast trigger input.
A PC connected to the digitizer with an 80 MB/s optical link was used to control the acquisition and store the waveforms for the offline analysis. This PC and the CAEN power supply (model: DT1415ET[4]) were controlled remotely using an Ethernet connection from the control room.
In the beam test at CNAO, the measurements were taken in one of the treatment rooms for nine beam energies ranging from 62 MeV to 229 MeV at the extraction of the accelerator with a beam flux of about 10^8 p/s and for four nominal distances (40, 60, 80, and 95 cm). In all measurements, both sensors

[4]https://www.caen.it/products/dt1415et/

were reverse biased at 275 V. The statistical error of the mean time depends on the duration of the beam irradiation time and is strictly related to the acquired number of coincident protons, and then to the relative ToF resolution of the system. As the prototype is done today, the main bottleneck in our system is set by the digitizer dead time with an acquisition efficiency of around 0.01 %. Even though that low efficiency, it was possible to obtain a proper statistic with a minimum of about 5000 coincidences, that can be reached in a few seconds of beam irradiation time. Thus, the irradiation time and the beam intensity have been selected in such a way, that for the lowest energy at the largest distance (the limit case, due to beam divergence, multiple scattering, and possible misalignment), the number of coincidences was about 5000. In total, between 10000 and 80000 waveforms were acquired for each test, depending on the energy corresponding to a number of spills ranging between 15 to 50. The entire electronic chain used at CNAO was the same tested in the laboratory in section 3.3.2.

3.5.2 Results

Fig. 3.15 shows the signal measured in all the strips (8 per sensor) exposed to 62.28 MeV proton beam in a time window of 205 ns. The distance between sensors is approximately 40 cm.

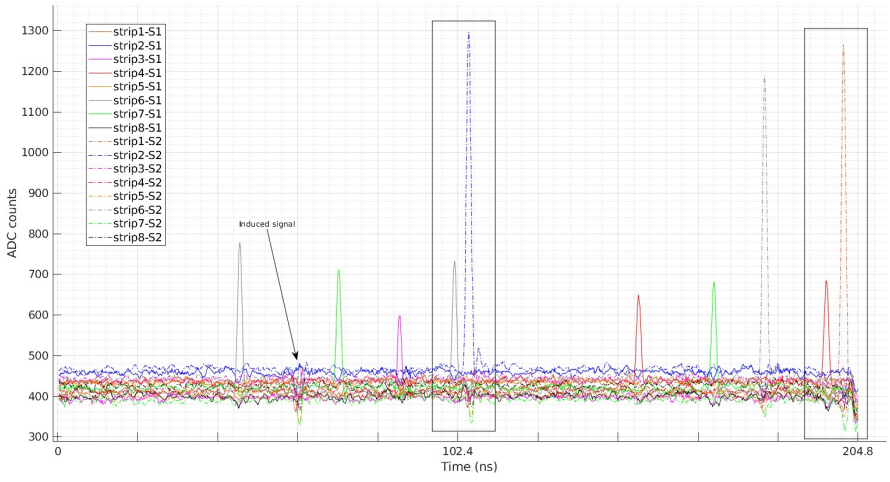

FIGURE 3.15: Example of a waveforms acquired by the digitizer in all the strips (eight per sensor) for the case of 62.28 MeV and 40 cm of distance between the detectors. The arrow points to an induced signal. Possible coincidence signals are marked with a rectangle.

A signal duration of about 2 ns was measured. It has to be noticed that an additional noise was measured during the beam irradiation, which is induced by particles crossing the neighbor strips in the whole sensors. This induced signal features a bipolar shape due to the weighting-field direction changing along the path, from the readout strip to the farthest neighbor strips. Also this effect happens if the strip is not connected to the read out as pointed out with the arrow in Fig. 3.15. The difference in the signals' amplitude for the same sensor is due to the statistical nature of the energy deposition process. Additionally, the bigger signals for S_2 is mainly due to the fact that the sensor has a gain layer 2% more doped with respect S_1. Interesting, in those waveforms it is possible appreciate coincidence signals, which were marked with a rectangle (see Fig. 3.15). As an example, Fig. 3.16a and Fig. 3.16b show the amplitude distribution for sensor S_1 and S_2 from which is possible extract the MPV for each strip of each sensor. The data correspond to the larger energy provided for the facility, which is the case with lower signal amplitude(the limit case). Theoretically, all the strips should have the same amplitude but this is not observed for example in Fig. 3.16b.
The cause of this non-homogeneity is due to the use of different channels on the Front-end board in which the passive components have a certain tolerance given by the manufacturer, causing different gain between channels.
It is important to point out that the internal gain of the strip was not causing this difference since it is reasonable to assume a constant internal gain for the different strips belonging to the same sensor. As explained in Chapter 1, in thinner absorber the Langaus distribution must be considered, in which the MPV no longer correspond to the maximum of the curve to extract the MPV. The extracted values are shown in Fig. 3.17 for different energies.
As can be noticed, by increasing the energy the MPV is reduced. The later effect happens because the energy loss in silicon is lower for larger energies as a consequence of a lower interaction times. Additionally, observing Fig. 3.17, it can be distinguished that the same tendency was maintained in both sensors for all the energies. For instance, in S_1 the strip with the larger amplitude was the number six, the second one was the strip eight, and so on. This behavior confirms the linearity of the front-end board in the range used in this application. This may allow a numerical correction factor to be applied to the data via software to align the thresholds. Furthermore, Fig. 3.18 shows the ratio between the MPV of the values reported in Fig. 3.17 for all the strips of a specific energy and the strip with the the maximum amplitude.

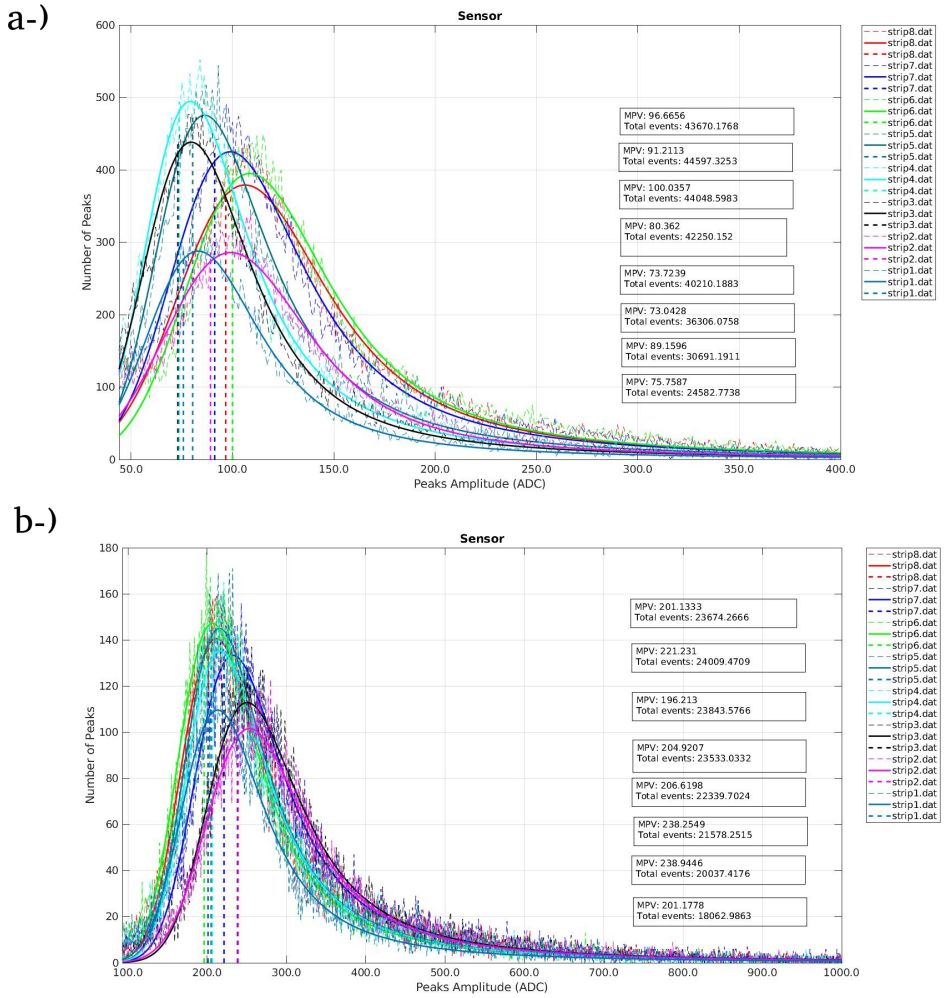

FIGURE 3.16: Langaus fit of the signal amplitude distribution for the case of 40 cm between sensors and 226.9 MeV. The vertical dashed line represents the MPV for each curve. (a) S_1. (b) S_2. The noise was cut to better visualization.

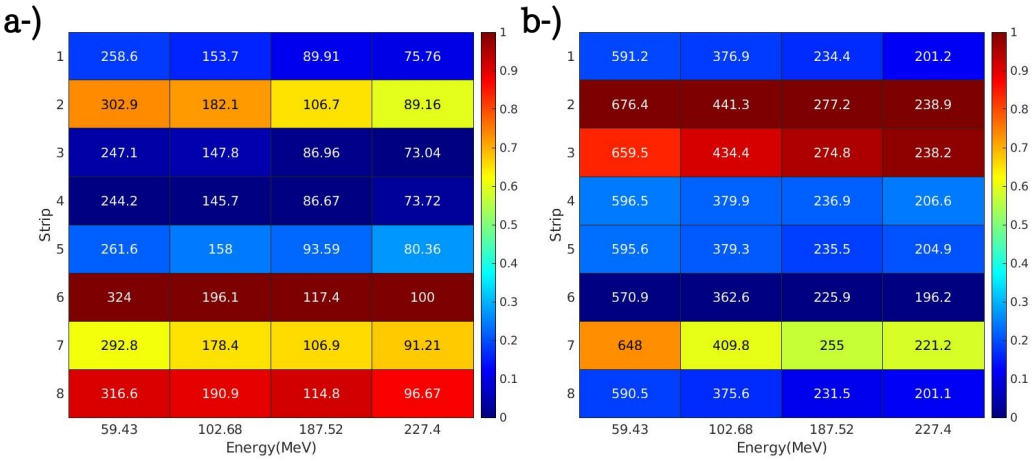

FIGURE 3.17: Extracted MPV (ADC) from the Langaus fit as a function of beam energy for all the strips. (a) S_1. (b) S_2.

strip	S_1	S_2
1	1.29	1.17
2	1.09	1.00
3	1.34	1.01
4	1.35	1.16
5	1.24	1.16
6	1.00	1.21
7	1.10	1.07
8	1.03	1.18

TABLE 3.5: Gain correction factors for each channel of the two sensors. It is calculated for one strip as the ratio between 1 and the average of the values reported in Fig. 3.18.

As observed in Fig. 3.18, the non-uniformity between channels is independent from the beam energy and reaches in the worst scenario up to about 30%.

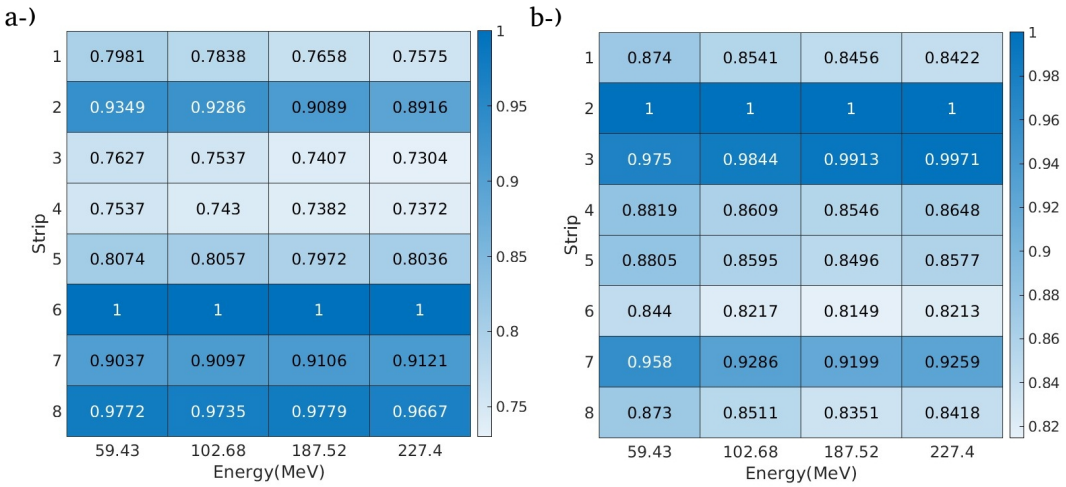

FIGURE 3.18: Ratio between the MPV of the values reported in Fig. 3.17 for all the strips of a specific energy and the strip with the the maximum amplitude (a) S1. (b) S2.

When the gain correction factor of Table 3.5 are applied to the waveforms, it shifts the amplitude of the signals to the strip with the highest gain (strip 6 on S_1 and strip 2 on S_2). This allows the selection of the same threshold for all strips to better separate signal from noise. Fig. 3.19 shows the signal amplitude distribution for all the strips together after applying the correction factor of Table 3.5 for different energies.

As expected, for the lower energy, the signal is higher due to the higher stopping power. On the opposite side, for the largest energy, the signal is lower as explained previously. Then, in the future, this energy will set the limit for our

device for selecting the threshold of the entire system because, as observed in Fig. 3.19, a threshold of about 50 and 100 ADC for S_1 and S_2 can separate the signal of individual protons which is subject to landau fluctuations from the Gaussian noise.

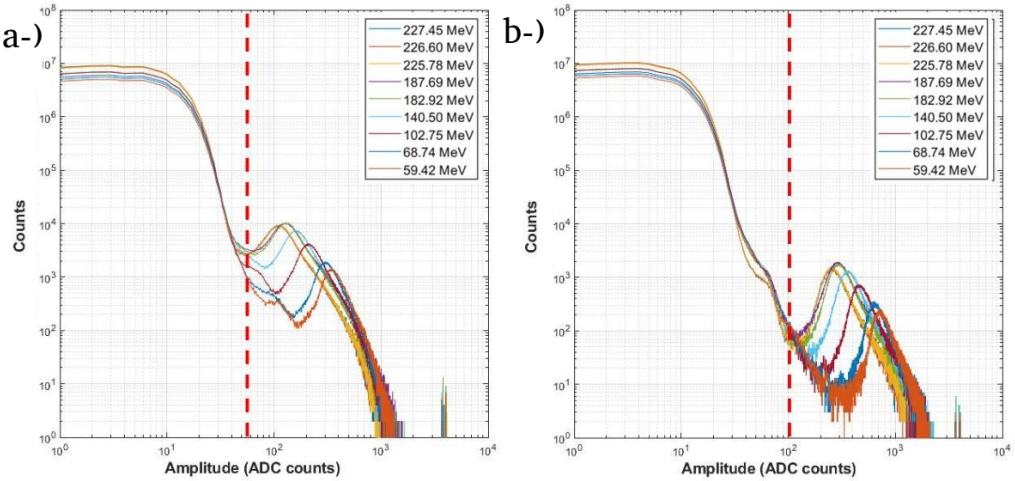

FIGURE 3.19: Amplitude distribution for the CNAO proton beam with energy at the isocenter ranging between 59.43 MeV and 227.4 MeV. The distance between sensor was 95 cm. (a) S1. (b) S2.

Then, proving the single particle detection capability of our system. However, in this thesis, we selected an individual threshold per energy per sensor. The threshold is defined as the inflection point of the distribution (see the red dashed line in Fig. 3.19) and the values were ranging between 53 to 150 ADC for S_1 and between 100 to 300 ADC for S_2, with the lowest threshold for the higher energy.

Energy measurements at the isocenter

Table 3.6 shows the main results of testing our system at CNAO. It followed the procedure explained in detail in section 3.2, and both the correction factor (Table 3.5) and the inter-channel delay were applied to obtain the reported results. The code written in $c++$ used for the analysis can be found in the my github repository[5]. As explained in the experimental setup, the distance between sensors were measured with an optical encoder and the values are reported in the second column. The Peakfinder[6], which has a maximum deviation of 0.15 mm in the water range, was employed at CNAO to measure

[5]https://github.com/omarti2504/ToF
[6]https://www.ptwdosimetry.com/en/products/peakfinder/

the depth-dose profiles. Therefore, conservatively it was assumed a constant uncertainty of 0.1 MeV for all the energies.
Fig. 3.20 shows the time resolution vs. nominal energy for a single crossing, calculated as $\sigma(\Delta t)/\sqrt{2}$. The standard deviation is extracted from the the Gaussian fit of Fig 3.3 for the true coincidences. It was observed a dependence on the energy of the protons and the values are between 43 and 67 ps. The increasing time resolution with the beam energy is due to the lower energy deposition which is translated into lower signal amplitudes. Mainly, the time resolution is strictly related to the amplitude of the signal and the main contribution that can worsen it is the so-called jitter and time walk effect (both inversely proportional to the signal amplitude). It is important to point out that the σ which was used to calculate the time resolution in Fig. 3.20 is not shown in Table 3.6. However, can be easily obtained by multiplying $error_{\Delta t_{mean}}(ns) * \sqrt{(Coincidences)}$.

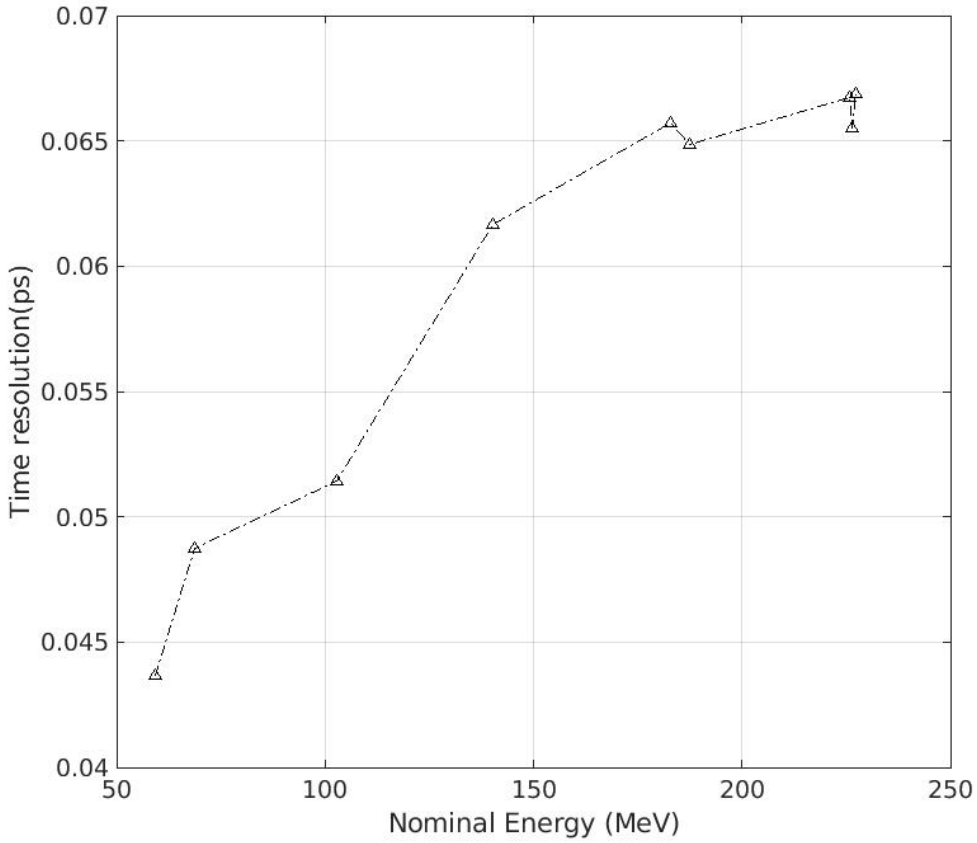

FIGURE 3.20: Time resolution for a single crossing as a function of the beam energy for 40 cm between sensors.

As it was reported in previous publication and was pointed out in this thesis,

Isocenter energy (MeV)	distance (m)	Δt_{mean}(ns)	$error_{\Delta t_{mean}}$(ns)	Coincidences
59.43	0.4003275	3.906	6.16E-04	10070
68.74	0.4003275	3.6539	5.61E-04	15062
102.68	0.4003275	3.0511	4.06E-04	32036
140.37	0.4003275	2.6702	3.97E-04	48271
182.75	0.4003275	2.3974	3.67E-04	64107
187.52	0.4003275	2.3724	3.32E-04	76369
225.73	0.4003275	2.2155	3.77E-04	62534
226.53	0.4003275	2.2106	3.77E-04	60431
227.4	0.4003275	2.2082	3.71E-04	64955
59.43	0.600286	5.8807	6.91E-04	8256
68.74	0.600286	5.4984	5.75E-04	12099
102.68	0.600286	4.596	4.67E-04	26463
140.37	0.600286	4.0232	4.70E-04	40628
182.75	0.600286	3.6176	3.93E-04	60021
187.52	0.600286	3.5798	3.79E-04	61564
225.73	0.600286	3.3417	4.31E-04	53787
226.53	0.600286	3.3372	4.33E-04	51792
227.4	0.600286	3.3332	4.33E-04	54659
59.43	0.800218	7.8585	6.45E-04	9166
68.74	0.800218	7.3474	5.82E-04	13876
102.68	0.800218	6.1422	4.41E-04	29521
140.37	0.800218	5.3814	4.04E-04	45743
182.75	0.800218	4.8368	3.67E-04	67654
187.52	0.800218	4.7879	3.70E-04	62592
225.73	0.800218	4.4665	4.50E-04	50901
226.53	0.800218	4.4613	4.43E-04	51864
227.4	0.800218	4.4543	4.35E-04	52291
59.43	0.9498985	9.3417	8.31E-04	6640
68.74	0.9498985	8.7318	6.75E-04	9535
102.68	0.9498985	7.2978	5.26E-04	21200
140.37	0.9498985	6.3904	4.71E-04	35299
182.75	0.9498985	5.7537	4.42E-04	42694
187.52	0.9498985	5.6955	4.72E-04	42220
225.73	0.9498985	5.3127	5.31E-04	33402
226.53	0.9498985	5.3062	5.52E-04	33759
227.4	0.9498985	5.2968	5.38E-04	34143

TABLE 3.6: List of the mean time differences with the relative uncertainties for the beam test conducted at CNAO.

our system needs a proper calibration due to systematic error in the experimental setup (mainly due to the uncertainty on the distance between the sensors and the time offset given by the electronic chain). It was used the self-calibration approach to calibrate the system. Basically, only 3 energies (59.43, 182.75, and 227.40 MeV) and 4 distances between sensors were used. The results can be observed in Fig. 3.21 for all the nominal energies. That figure shows the energy difference in MeV which is given by the deviation between the nominal and the measured energy. The dash line in Fig. 3.21 shows the correspondent deviation in water range (within ± 1 mm in red and within ± 0.5 mm in purple).

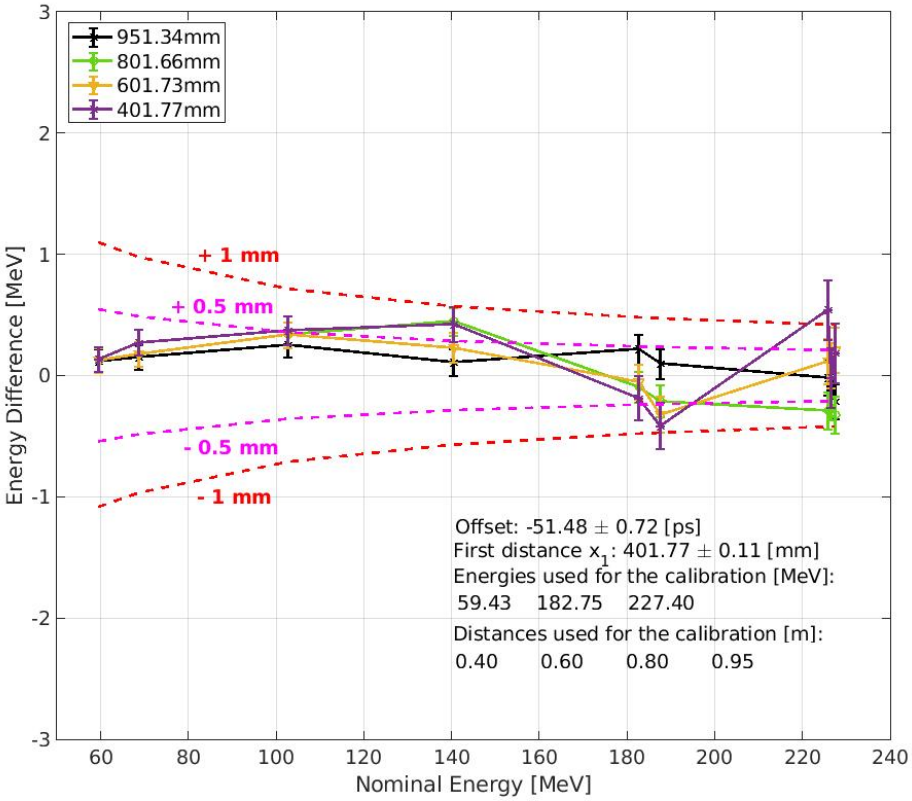

FIGURE 3.21: Deviations between the nominal and the measured energy using 4 distances between the sensors. The dot-lines delineate the correspondent deviations in water range. The energies used for the calibration were: 59.43 MeV, 182 MeV, and 227.4 MeV. The others energies were unknown at the time of the beam test.

The obtained distances after a calibration and the ones from the optical encoder are reported in Table 3.7. The reported deviation between the distance obtained from the optical encoder and the distance from the calibration was

Parameter	$Distance_{Encoder}(mm)$	$Distance_{Calibration}(mm)$	**Distance deviation(mm)**
d_1	400.3275	401.77	1.44
d_2	600.286	601.73	1.44
d_3	800.218	801.66	1.44
d_4	949.8985	951.34	1.44

TABLE 3.7: Comparison between the distance measured with the optical encoder and the distance obtained after the calibration.

fixed, exactly 1.44 mm. The discrepancy can be related due to mechanical setup or possible positioning error of the sensors.

The obtained offset was $-51.48 \pm 0.72ps$. As can be appreciated in Fig. 3.21, for all the energies and distances the error in measured the energy is within $\pm 1mm$ (less than 0.5 MeV) in water range, therefore, within the clinical acceptable accuracy. The most accurate results ($\pm 0.5mm$) were for the largest distance as previously obtained in other study (Vignati et al., 2020a). The others energies reported in Fig. 3.21 (different from those used for calibration) were the test points where the energy was unknown at the time of the beam test. Therefore, the values were retrieved after calibration with a difference in energy within the clinical acceptable error. Finally, even though for the lowest distance it was obtained the largest error, they are within the clinical acceptance margin, thus also can be used to assess the beam energy as well. It was highlighted the lowest distance, once in the future can facilitate the construction of a device of small dimension, that can be very useful and practical in daily Quality Assurance procedures.

Chapter 4

Clinical carbon ion beam measurements with thin silicon sensors

4.1 Introduction

Carbon ion treatment provides several unique physical and radiobiological properties, as they exhibit higher linear energy transfer (LET) than photons and protons (Malouff et al., 2020). This leads to higher relative biological effectiveness (RBE), where damage caused by carbon ions accumulates in DNA, overwhelming cellular repair systems (Mohamad et al., 2017). In addition, due to their physical properties, they are more effective in the treatment of hypoxic tumors and can more effectively eradicate tumors that would have been resistant to photons (Chiblak et al., 2016; Rackwitz and Debus, 2019). By taking advantage of these properties, carbon ion radiation therapy (CIRT) may allow dose escalation to tumors while reducing radiation dose to adjacent normal tissues (Malouff et al., 2020).
Until relatively recently, the ionization chamber has been the reference device adopted as the gold standard for absolute dose dosimetry and beam verification (Debrot et al., 2018). For example, at the National Centre for Oncological Hadrontherapy (CNAO, Pavia, Italy), beam monitoring is performed using transmission ionization chambers with a large sensitive area that allows measurement of the pencil beam in the delivery of a single treatment. Although this technology is very robust and has been shown to have high precision and reproducibility, they have low sensitivity (thousands of particles), slow charge collection times (hundreds of microseconds), and cannot provide the required space-time (Karger et al., 2010). These drawbacks limit the development of fast beam delivery strategies needed to improve accuracy to shorten

treatments and increase patient throughput.
To verify beam characteristics for quality assurance in charged particle therapy, especially with carbon ions, sensors with high spatial and temporal resolutions, capable of resolving steep dose gradients, and suitable for energy verification are needed. These sensors should be able to handle a high instantaneous fluence rate (up to 10^8 carbon/cm^2s) and an energy range of up to 400 MeV/u. In this context, thin silicon sensors represent a suitable technology to build the new generation of online beam monitors for charged particle therapy (Vignati et al., 2017; Sacchi et al., 2020; Marti Villarreal et al., 2021). (Debrot et al., 2018) developed a serial Dose Magnifying Glass (sDMG) detector consisting of two silicon-sensitive 128-volume linear arrays ($2mm$x$50\mu m$x$100\mu m$) fabricated on a p-type substrate with a pitch of 200 μm. This detector was characterized by measuring its response in a broad 290 MeV/u carbon ion beam, and the authors concluded that sDMG was suitable for quality assurance of fast energy and range verification.
In the work presented by (Gehrke et al., 2017), the capability of "Timepix", a pixelated silicon detector, to measure the energy deposition of individual ions in thin layers was investigated. The authors measured the energy deposition distribution of therapeutic proton, helium and carbon ion beams on a 300 μm-thick sensitive silicon layer and compared the results with the expected energy deposition spectra predicted by simulations of Monte Carlo using the FLUKA code. The measurements were in good agreement ($< 7\%$) with the simulation. However, the authors reported that energy deposition above 10 MeV/mm with a fully depleted sensor can suffer from saturation effects and recommended the use of thinner sensors to improve energy deposition measurements on silicon sensors. In a more recent study by the same group (Félix-Bautista et al., 2019) used two synchronized silicon pixel sensors based on Timepix technology to detect and track secondary ions outgoing from a patient-like phantom for the assessment of the lateral pencil beam position in a clinic-like carbon ion treatment fraction. The sensors used had a sensitive area of 1.4 x 1.4 cm^2, a thickness of 300 μm and were divided into 256 x 256 pixels (55 μm pitch). For beam energies greater than 197.58 MeV/u, the precision of the measured positions was less than 2 mm.
An interesting study related to a beam instrumentation device was carried out by (Bal et al., 2021). The authors evaluated "Medipix3", a hybrid pixel detector with a silicon sensor (active thickness: 550 μm and pixel pitch: 55 μm). This device was tested with proton and carbon ions in the range: 62.4 to 800 MeV and 120 to 400 MeV/u, respectively. Measurements included

simultaneous high resolution, beam profile and beam intensity, as well as count rate linearity and radiation damage assessment. The authors observed for 62.4 MeV protons a cluster of approximately 4-5 pixels (charge sharing). As the beam energy increases, the cluster size decreases because less charge was deposited over the depth of the sensor. This effect was also observed for carbon ions, but on a large scale due to the large charge deposited. Likewise, (Wang et al., 2017) reported the results of a beam monitor based on a silicon pixel sensor. In this study, the measurements were made with a carbon ion beam of 80.55 MeV/u at the Heavy Ion Research Facility in Lanzhou (HIRFL) China (Li et al., 2007). The authors showed that this monitor can measure the position and angle of incidence with a resolution better than 20 μm and 0.5 degrees, respectively. Likewise, the statistical accuracy in the beam intensity measurements was better than 2% with only 80.55 MeV/u.
Despite the wide use of silicon sensors in the detection of charged particles, it can be seen that there are not many works that use them for the monitoring of charged particle beams used in radiotherapy. At the same time, there is a consensus among the works consulted that reducing the active thickness of the sensor could further improve its performance and reduce the influence of unwanted effects such as charge sharing. In this context, the importance and benefits of testing thinner silicon sensors to be used as beam instrumentation devices is very clear. That is why the aim of this chapter will be to report the measurements of individual carbon ions in the CNAO clinical beam with 60 μm thick silicon sensors.

4.2 Materials & Methods

4.2.1 Experimental setups

This study used validated type T sensors from the MoVe-IT 2020 production, which are segmented sensors on 11 strips (4 mm x 0.55 mm each) with no gain layer on any strip and active thickness of 60 μm. The selected sensors (W8-T_{11}, W8-T_{10}, and W9-T_{10}) belong to Group III (Si-Si substrate) and were previously measured in the laboratory, as described in Chapter 2. All strips were found to have a breakdown above a reverse bias voltage greater than 300 V, therefore, having a perfect behavior. The selected sensors were wire-bonded to an 8-channel custom front-end board (see Fig. 3.5), as explained in section 3.3.1. Additionally, the notation for the strips used in chapter 3 was adopted, where only strips 3 thorough 10 were limited to one of the eight

channels of the front-end board, and are referenced with the number from 1 to 8.

Fig. 4.1 shows the first experimental setup used to measure the energy released in a thin silicon sensor (W8-T_{11}) by single carbon ions delivered by the CNAO synchrotron. The main objective of these measurements was to analyze the signal shape and the energy released in a thin silicon sensor by a clinical carbon ions beam using different conditions.

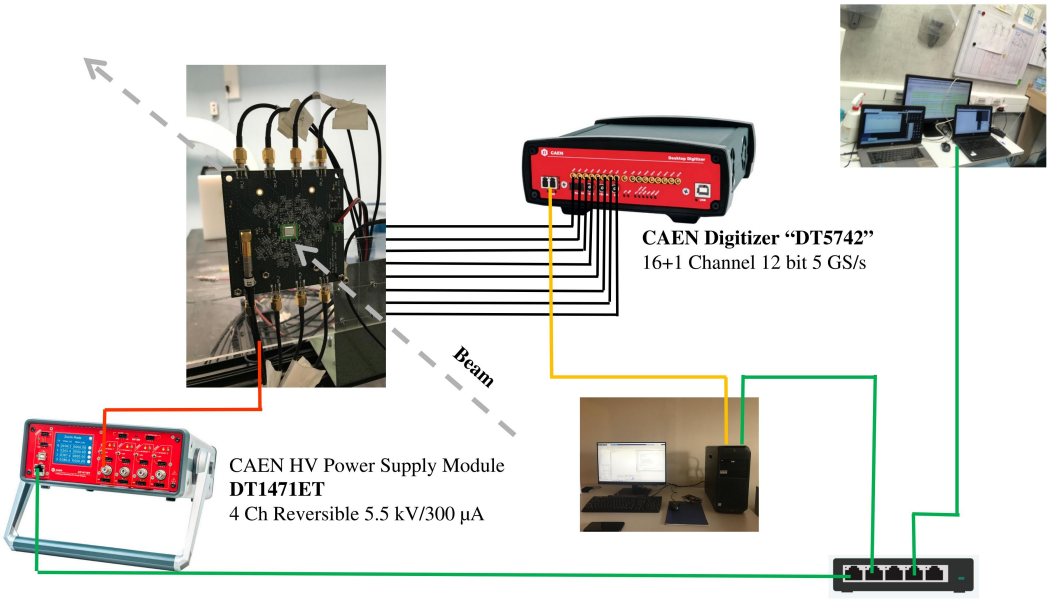

FIGURE 4.1: Experimental setup (1) used at CNAO.

The outputs of the board were connected to the high rate CAEN digitizer (model: DT5742, 5 GS/s, 12 bits resolution, 1 ADC = 0.24mV, acquisition windows of 1024 samples, i.e. 204.8 ns, more information about the DT5742 is given in Chapter 3). A PC connected to the digitizer with an 80 MB/s optical link was used to control the acquisition and store the waveforms for the offline analysis. This PC and the CAEN power supply (model: DT1471ET[1]) were controlled remotely using an Ethernet connection from the control room. In Fig 4.2 two pictures of the experimental setup used in this experiment can be observed.

The measurements were performed with 4 beam energies, representatives of the entire clinical energy range (115.23 MeV/u, 166.41 MeV/u, 268.60 MeV/u, and 398.84 MeV/u). The required number of ions per spill was $8{\times}10^7$ C/spill and nine different reverse bias voltages for the sensor were used (3.8 V, 9.0 V, 18.8 V, 34 V, 49 V, 99 V, 149 V, 199 V, and 299 V). Measurements were taken at room temperature, with the sensitive detector area

[1]https://www.caen.it/products/dt1471et/

a-) b-)

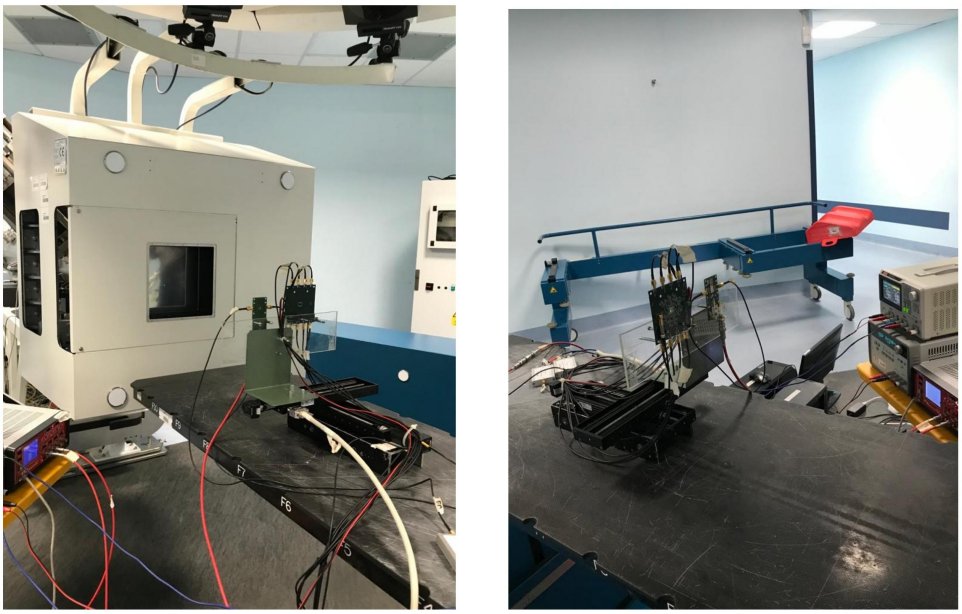

FIGURE 4.2: (a) Picture of the experimental setup (1) used at CNAO in the treatment room in which the detector placed at the isocenter is shown. (b) Picture of the experimental setup (1) used at CNAO in a different view.

perpendicular to the beam direction (1st position) and with a tilt of about 40 degrees with respect to the 1st position (2nd position).
Fig. 4.3 shows the second experimental setup used at CNAO. The main objective was to measure the time resolution obtained using two silicon sensors placed in a telescope configuration. The electronic chain is the same used in section 3.3.1. Two silicon sensors (W8-T_{10} and W9-T_{10}) with similar characteristics to sensor W8-T_{11} were placed in a telescope configuration, as shown in Fig. 4.3. The first sensor was placed at the isocenter, while the second sensor was positioned at a relative distance of about 30 cm from the first sensors. The exact distance between the two detectors was measured using an optical encoder model (Renishaw Evolute EL26BBB500F10A) with a resolution of 0.1 μm. The measurements were taken at two clinical energies (115.23 MeV/u and 398.84 MeV/u) and for three reverse bias voltages (50 V, 100 V, and 200 V).

4.2.2 Offline signal analysis procedure

A Matlab application was written to automatically detect the peaks and their position to perform later the amplitude distribution and the proper fits. It

FIGURE 4.3: Picture of the experimental setup (2) used at CNAO to measure the time resolution for a single crossing. The system is based on a telescope configuration of two silicon sensor.

mainly consists in the predefined custom function Peakseek[2], which detects all the peaks higher than a predefined threshold. It is important to point out that before performing any peak detection in all waveforms were carried out the baseline subtraction using the mode[3]. The initial and end points of the signal generated by the carbon ion is calculated, first selecting a peak higher than a threshold. In order to locate the position of the initial/end points of the signals, the following criteria were followed. It is defined as the first point located at the left/right of the position of the peak lower than 0.05 of the maximum signal's amplitude. The signal duration is the difference in time between the point identified to the right and to the left of the signal's peak. The measured time for each bias voltage follows the Gaussian distribution, then the mean of the Gaussian fit is the measured time duration for each acquisition.
The time resolution for a single crossing is calculated as:

$$\sigma = \frac{\sigma(\Delta t)}{\sqrt{2}} \tag{4.1}$$

The time of arrival of a carbon ion on each sensor is determined using the constant fraction discriminator algorithm (CFD), and the estimated mean

[2]https://it.mathworks.com/matlabcentral/fileexchange/26581-peakseek
[3]https://it.mathworks.com/help/matlab/ref/mode.html

(Δt) is obtained as the average of the difference between the times of arrival of the same carbon passing through the two sensors. Therefore, $\sigma(\Delta t)$ is the width of the peak in the distribution of the time difference values as described in more details in the Chapter 3 or (Vignati et al., 2020a). As a first approximation, the measured deposited charge $Q(fC)$ is calculated as:

$$Q = \frac{\int V(t)dt}{50\,\Omega} \tag{4.2}$$

where: $\int V(t)dt$, is the signal area and $50\,\Omega$ is the input impedance of the digitizer's acquisition instrument used during the measurements. It is important to point out that the gain of the electronic chain is not considered in Eq. 4.2.

4.3 Results & discussion

Fig. 4.4 shows the signal produced, after baseline subtraction, by carbon ions of 398.84 MeV/u in a 30 ns time window using a bias voltage of 149 V.

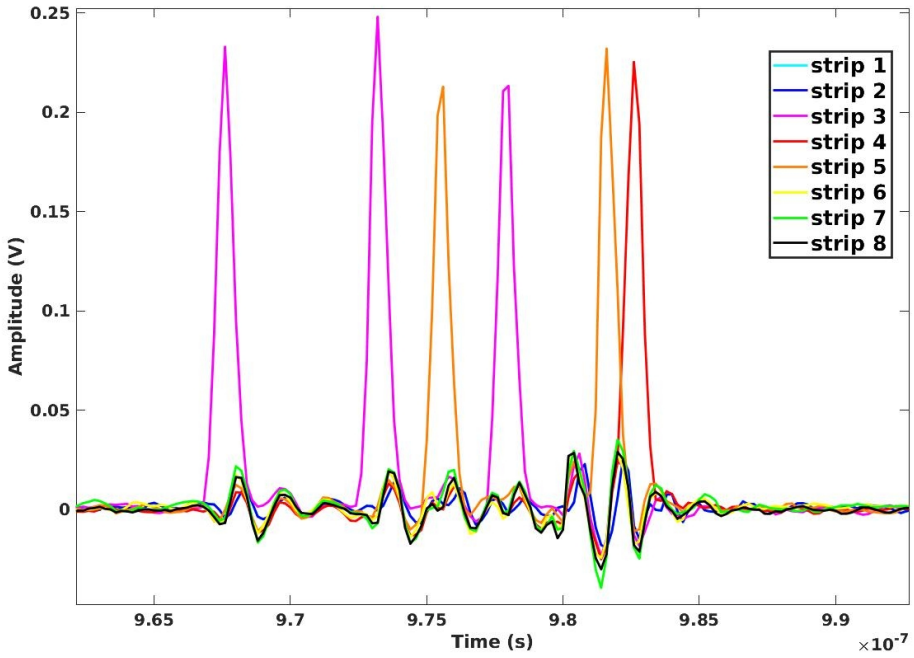

FIGURE 4.4: Signals produced by 398.84 MeV/u carbon ions in a 60 μm thick strip silicon detector using a reverse bias voltage of 149 V.

The sharp peaks in strips: 3 (purple), 4 (red wine), and 6 (yellow) correspond

to the passage of carbon ions. These signals have a duration of about 2ns. As seen in the figure, a bipolar signal was observed in the strips neighboring the strip through which the carbon ion passed. That noise in the form of a bipolar-shaped signal is a consequence of the change in direction of the weighting field along the path, from the reading strip to the farthest neighboring strip. Fig. 4.5 shows the signals produced in a single strip by carbon ions of 398.84 MeV/u but for two different reverse bias voltages: < 10 V (Fig. 4.5a) and 149 V (Fig. 4.5b).

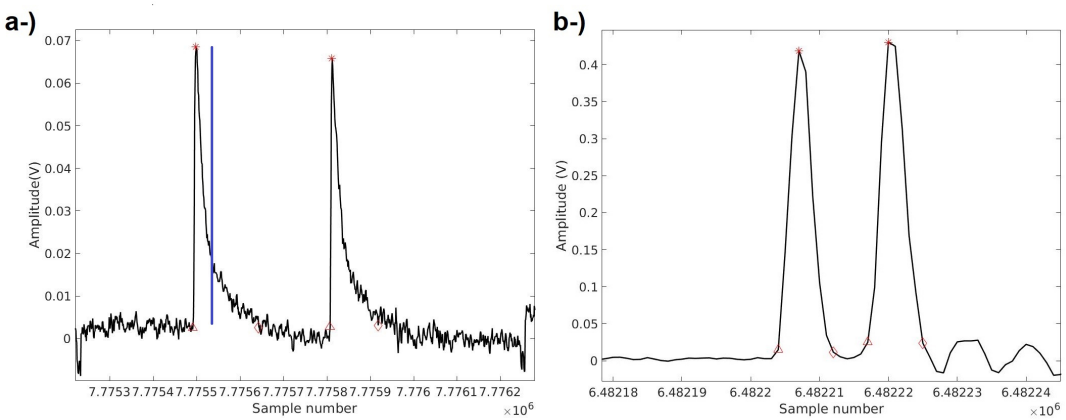

FIGURE 4.5: Example of the signals produced by 398.84 MeV/u carbon ions in a 60 μm thick silicon strips using a reverse bias voltage of (a) < 10 V. The blue line shows an approximate point where all the electrons were collected on the readout electrode. (b) 149 V. The triangle and diamond marks on the waveforms shows the initial and end points of the signal generated by the carbon ion.

In both cases, the signals have almost a null rise time because the signals start developing as soon as the carriers move into the bulk. However, it can be seen that the signals for the lowest voltage have a long tail. The difference observed is related to the electric field inside the silicon, which drifts the electron and holes. The vertical solid blue line in Fig. 4.5a indicates the approximate time in which the electrons are collected at the readout electrode. After that, the observed tails correspond to the collection of holes, which have lower mobility.

Fig. 4.6 shows the signal duration calculated for different bias voltages for 398.84 MeV/u. As illustrated, for bias voltage greater than 150 V, the signal duration reaches a plateau due to electron drift velocity saturation. For these values, the duration of the signal was less than 1.9 ns, decreasing to 1.4 ns at 299 V. On the other hand, at reverse bias voltages lower than 20 V, the duration of the signal is greater than 6 ns, reaching a maximum value of about 23

ns for 9 V. Fig. 4.7 shows the amplitude distribution for the highest carbon ion energy (398.84 MeV/u) in all strips (Fig. 4.7a), and for all four measured energies (115.23, 166.41, 268.60, and 398.84 MeV/u) in a single strip (Fig. 4.7b).

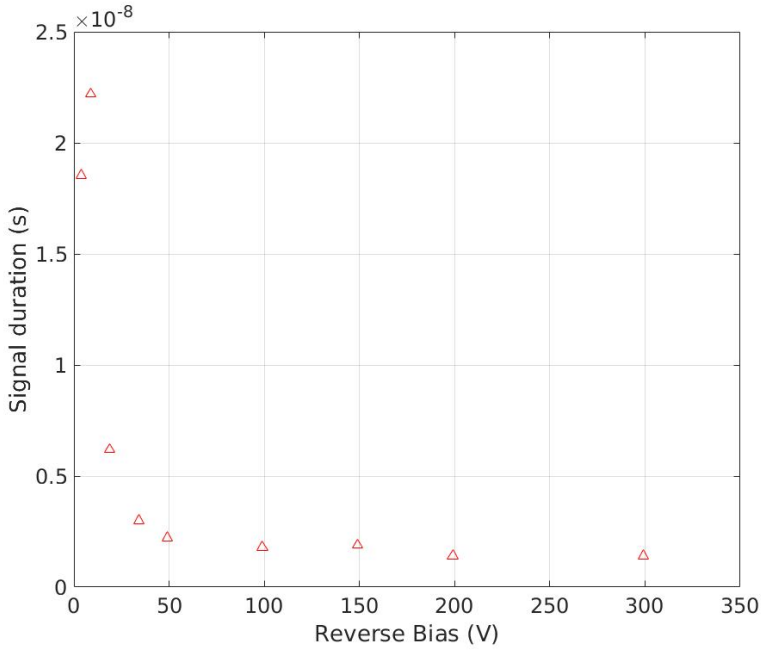

FIGURE 4.6: Signal duration as a function of reverse bias voltage.

As can be seen, in all cases a good separation between signal and noise can be achieved by choosing an appropriate threshold. All the data were fitted using a Langaus distribution, with a coefficient of determination greater than 0.99. In Figure 4.7a the most probable values (MPV), extracted from the fit, ranged between 0.22 - 0.24 V. The difference obtained between strips is related to the tolerance in the passive component in the front-end board for each channel. In Fig. 4.7b, it can be seen how the MVP of the signal amplitude increases with decreasing carbon ion energy beam, as expected. The small hump observed to the left of the distribution, more noticeable for higher energies, indicate the occurrence of charge sharing between adjacent strips. For strip 1, the measured deposited charges (Q), calculated as Eq. 4.2 using a reverse bias voltage of 149 V is shown in Fig. 4.8. Each distribution in Fig. 4.8 was fitted with the Langaus distribution to obtain the MPV of the deposited charge. Considering the landau fluctuations, the charge deposited for all energies covering the clinical range is between 2000 fC and 9000 fC. As explained previously, the electronic chain has a nominal gain of 100, and therefore the deposited charge is between 20 fC and 90 fC.

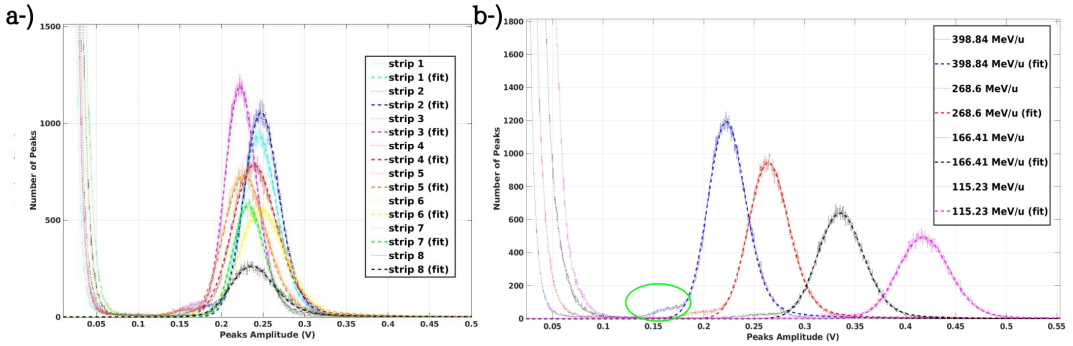

FIGURE 4.7: (a) Number of peaks vs. peaks amplitude for carbon ions with an energy of 398.84 MeV/u and using a bias voltage of 149V. (b) Number of peaks vs. peaks amplitude for carbon ions for four different energies in the strip 3 using a reverse bias of 149 V. The green ellipse marked a region where the charge sharing is observed.

This is an important consideration when designing a board to handle carbon ions in the clinical range. The MPVs of the deposited charge for the four different energies were: 7177 fC, 5626 fC, 4316 fC, and 3542 fC for 115.23 MeV/u, 166.41 MeV/u, 268.6 MeV/u, and 398.84 MeV/u, respectively. Considering the stopping power in silicon for carbon ions, it was possible to estimate the deposited charge released in 60 μm (78.89 fC, 60.93 fC, 45.54 fC, and 37.36 fC for 115.23 MeV/u, 166.41 MeV/u, 268.6 MeV/u, and 398.84 MeV/u, respectively). Accordingly, the amplifier gain is 90.97, 92.34, 94.77, and 94.8.

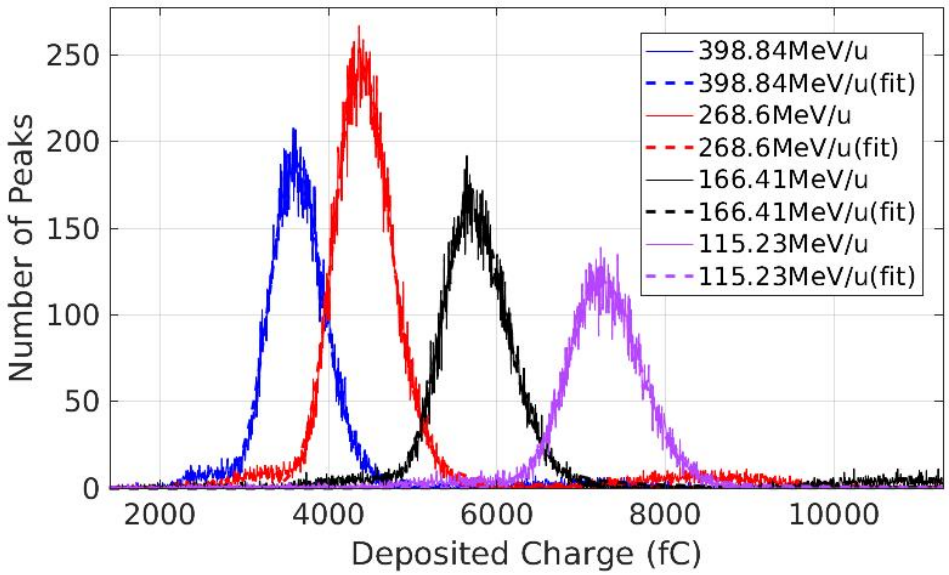

FIGURE 4.8: Charge deposited in a thin silicon sensor by carbon ions for four different energies in the strip 1 using a reverse bias of 149 V.

Fig. 4.9a shows the total number of peaks identified for a reverse bias voltage of 149 V for all the energies in the eight strips of the sensor. As observed, the beam was aligned between strip 2 and 4, where it reached a maximum. The number of peaks was normalized at the maximum, as presented in Fig. 4.9b. The position expressed in mm was calculated considering the dimension of the sensor. Therefore, strip 1 is the reference 0 mm position. Strip 2 is positioned at 0.591 mm (the pitch), strip three at 1.182 mm, and so on until it reach strip 8 (4.728 mm). As observed, the beam for all the energies follows a Gaussian shape. For that reason, all the curves were fitted with the Gaussian function. From the fit, it was obtained the sigma and then the FWHM, which is from the lower energy to the higher: 7.4 mm, 6.9 mm, 6.1 mm, and 4.9 mm. The values agree with what was found by (Mirandola et al., 2015).

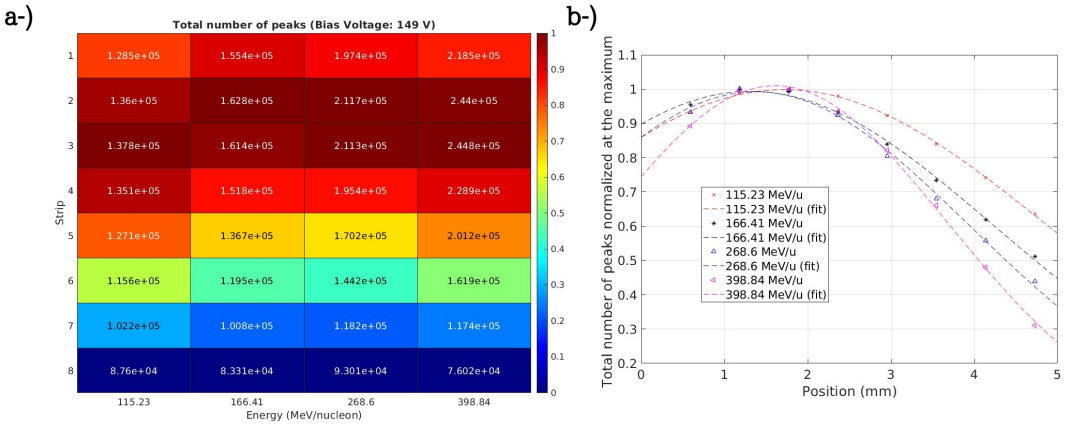

FIGURE 4.9: (a) Heatmap of the total number of peaks using a reverse bias voltage: 149 V for the four energies used. (b) Total number of peaks normalized at the maximum *vs.* position (mm) for 149 V and for the four energies used.

In addition, the MPV of the amplitude distribution for different bias voltages as a function of the energy of the beam was represented for strip 2 (Fig. 4.10). A decreased MPV at lower bias voltages of the same energy was observed due to the no saturation of the drift velocity, mainly for the electrons.
Fig. 4.11 shows the MPV of the amplitude distribution as a function of the bias voltage for strip 1 and 2 with the sensor positioned at two different angles with respect to the beam direction (0 and 40 degrees) for 398.84 MeV/u. As expected, rotating the sensor increases the signal amplitude, reflected in a higher MPV due to the larger path travel for the carbon ions, creating additional electrons and holes. In fact, a fixed ratio between the MPV for the two angles equal to 1.26, was obtained, representing a rotation of approximately 38 degree with respect to the incidence direction of the beam. Furthermore,

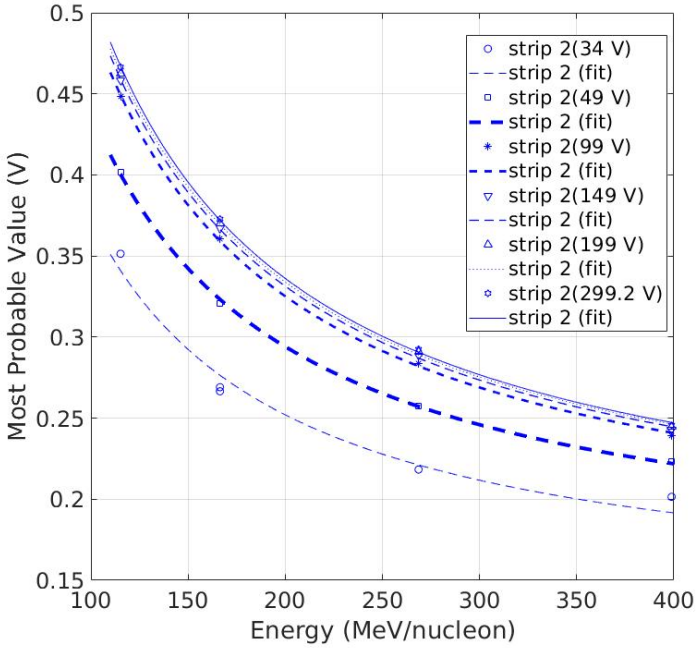

FIGURE 4.10: Most probable value *vs*. Energy (MeV/u) for strip 2 using several bias voltages.

in figure 4.11 it can be seen that for bias voltages greater than 150 V, a plateau in the MPVs is reached for both experiments. This HV value generates an electric field of about 30 kV/cm in the sensor, which at room temperature is the value necessary to saturate the drift velocity of the electrons (Ferrero et al., 2021). However, it is not enough to saturate the drift velocity of holes, which is reached for higher values of the electric field (100 kV/cm) (Ferrero et al., 2021). The difference in mobility between these two charge carriers is the main reason why the observed plateau continues to increase slightly with voltage (see Fig. 4.11).

Using experimental setup 2 (see Fig. 4.3), it was possible to obtain the time resolution for a single crossing for the two extreme beam energies, as shown in Figure 4.12. As expected, increasing the bias voltage improves the temporal resolution, as drift velocity saturation is reached (see Fig. 4.11), mainly for electrons, thus the pulse amplitude increases. The time resolution reached was lower than 30 ps for the two energies and for all the bias voltages. These values are comparable to the temporal resolution obtained with LGAD, for protons, confirming that a thin silicon sensor can be used for carbon ion timing applications due to the large energy deposition in silicon. The time resolution is strictly related to the amplitude of the signal and the main contribution that can worsen it is the so-called jitter and time walk effect (both

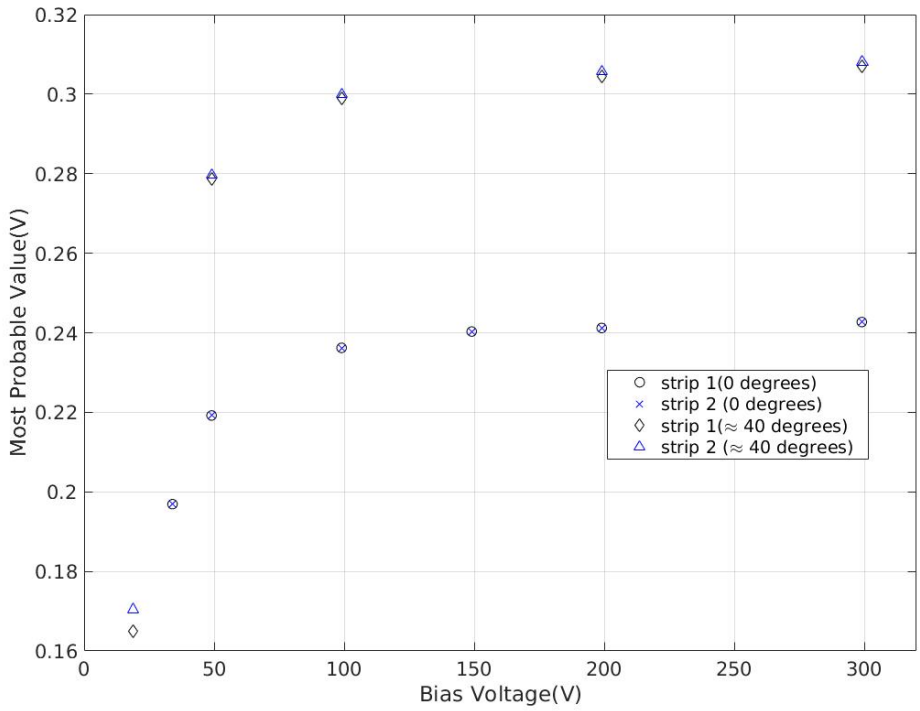

FIGURE 4.11: Most probable value *vs*. bias voltage for strip 1 and strip 2 with the sensor positioned at two different angles with respect the beam direction (0 and 40) for 398.84 MeV/u.

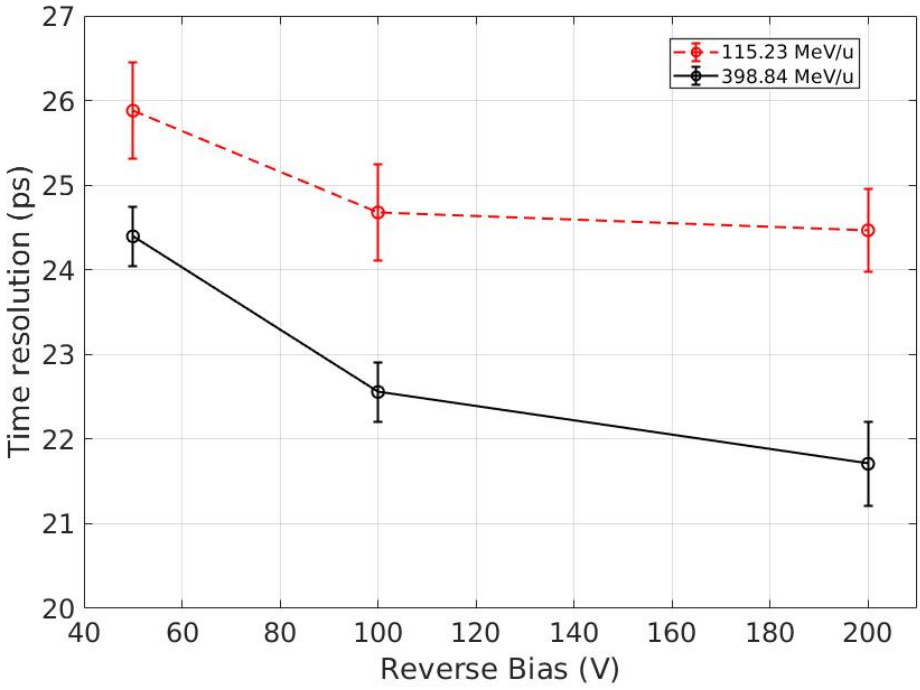

FIGURE 4.12: Time resolution for a single crossing as a function of reverse bias voltage for two carbon ions beam energies.

inversely proportional to the signal amplitude). The unexpected behavior of a large time resolution for the lower energy can be related to low statistics, which may be associated with errors in the Gaussian fit to extract the sigma (see Eq. 4.1), as explained in detail in chapter 3.

Chapter 5

Silicon Devices for Monitoring FLASH beams

5.1 Introduction

Real-time monitoring the dose delivery would be essential to study the parameters triggering the FLASH effect in Ultra High Dose-Rate (UHDR) irradiations. In recent years, the international community has focused on developing an online beam monitor device for real-time dosimetry that can be used in the future clinical implementation of FLASH radiotherapy (FLASH-RT). The main requirements for a real-time beam monitor are high temporal and spatial resolution, beam transparency, large response dynamic range, and radiation hardness.

Most dosimetric studies until now in FLASH-RT employ passive detectors such as alanine, radiochromic films, TLDs, and Methyl viologen(MV). These detectors have some desirable properties like a linear relationship with the dose-rate(dose-rate independent). Also, they are successfully used for small field dosimetry (TLD, films, and alanine). However, passive detectors require a complex and time-consuming evaluation procedure, including post-irradiation processing that requires calibration for each batch, which can be time-consuming. They have significant large uncertainties if the evaluation process is not well established. Some studies have focused on reducing the reading time. (Gondré et al., 2020) reported the procedure for optimizing the alanine measurements for fast and accurate dosimetry in FLASH-RT. Mainly is based on optimizing the number of reading parameters such as the number of scans, microwave power, the amplitude of the magnetic field, etc. It has been demonstrated that doing that optimization, the total reading time of three measurements was 7.8 minutes with $\pm$2% (k=1) uncertainty for doses above 10 Gy, and to measure doses below 5 Gy with an uncertainty below 5%

the reading time increased to 13 minutes. Although those devices are robust and reliable, the lack of real-time information limits their use as future beam monitors in the perspective of a forthcoming clinical translation. The active detectors can fulfill that requirement because they can give information on the dose delivered in real time. Nowadays, some potential active detectors that can satisfy that need can be ionization chambers (IC), diamond detectors, silicon carbide (SiC), and silicon sensors.

The ionization chamber is subject to correction when dealing with ultra-high dose rates due to ion recombination. Mainly the recombination can be summarized as follows:

1. The initial recombination is created along a single charged particle track. It is considered independent of the dose and dose-rate and is more pronounced in highly ionizing particles such as alpha particles.

2. The general recombination occurs between two separate charged particle tracks. It is directly proportional to the charge density (i.e., the number of ions produced per unit volume) and dose rate-dependent.

In summary, general recombination plays a much more significant role in the recombination effect in UHDR pulse beams, therefore this effect has been studied widely (Di Martino et al., 2020). One of the most notable works was published by (Petersson et al., 2017). The authors investigated the ion recombination effect using a parallel plate ionization chamber PTW Advanced Markus with 1 mm electrode separation. The ion collection efficiency as a function of Dose-per-pulse (DPP) showed that the charge collection efficiency is close to unity in the area of conventional dose-rate. However, a significant drop in the efficiency in the ultra-high dose per pulse region was observed, which is related to ion recombination effects. For instance, when this chamber was tested at 10 Gy per pulse, only about 30 % of ion collection efficiency was observed. Additionally, it was proposed in that work a method to correct the efficiency loss using an empirical equation with no physical meaning, based on the fitting of two parameters.

The same effect has been reported by (McManus et al., 2020) using a PTW Ross chamber with a 2 mm gap between the electrodes. It was studied in a 200 MeV electron beam (VHEE beam) with a DPP: 0.03-5.3 Gy/pulse. The reference detector employed in the study was a graphite calorimeter. The collection efficiency was 10% and 25%, when the IC was operated at 200 V (the value recommended by the manufacturer) and 600 V, respectively. The authors highlight that the available analytical ion recombination models can not predict chamber behavior for such a high DPP.

Nowadays, new developments and studies have focused on ionization chambers in ultra-high DPP (Schüller et al., 2020). Mainly (Gómez et al., 2022) carried out a simulation that demonstrated that the ion recombination correction factor (ks) for plane-parallel ionization chambers at 300 V for 5 Gy/pulse is almost 1 when the distance between electrodes is below 0.30 mm. As a result, the authors developed a prototype of an ionization chamber with a 0.27 mm gap between electrodes. The prototype was tested in a real beam in which the measured charge per pulse (nC) showed an excellent linear response as a function of dose-per-pulse, and the results were in agreement with the prediction performed by the simulation.
The diamond detectors are promising for monitoring UHDR beams because they have several advantages concerning the ionization chamber. They do not suffer from ion recombination effects and maintain high water equivalence of the sensitive volume in terms of effective atomic number. Additionally, have good response stability concerning the accumulated dose. Microdiamond has recently been studied in UHDR, for example, the research done by (Kranzer et al., 2022). The authors studied the dose-per-pulse in the microdiamond versus the reference dose-per- pulse for different detector sensitive areas and series resistance. It was observed in the commercially available micro-diamond detector, saturation effect at different dose-per-pulse level. The linear range can be extended to the ultra-high DPP range by reducing sensitivity and series resistance. Furthermore, (Verona Rinati et al., 2022) showed that the flashDiamond (fD) prototype proposed by (Marinelli et al., 2022) has a linear response in the whole investigated DPP range (the DPP was varied in the 1.2–11.9 Gy range, by changing either the beam applicator or the pulse duration from 1 to 4 μs).
Another semiconductor detector that is a promising device for beam monitor is silicon, which is a mature technology (Vignati et al., 2020c). However, to date, the response of these sensors in UHDR beams has not been much explored. Within the FRIDA project, the University and INFN of Turin are studying thin silicon sensors, recently designed and produced for single particle tracking in proton therapy, for electron beam monitoring in high dose-rate regimes. This chapter describes the results of testing thin silicon sensors at UHDR. In addition, the partial results of the first attempt to upgrade the LINAC (Elekta SL 25 MV) installed in the Physics Department at UNITO, dedicated entirely to research, will be presented, which will allow in the near future experiments to study the FLASH effect.

5.2 LINAC Upgrade

5.2.1 ELEKTA/Philips SL 25 LINAC

The Linear Accelerator (Linac Elekta SL 25 MV), entirely dedicated to research, was installed in 2016 at the physics department of the University of Turin (Italy) as shown in Fig. 5.1.

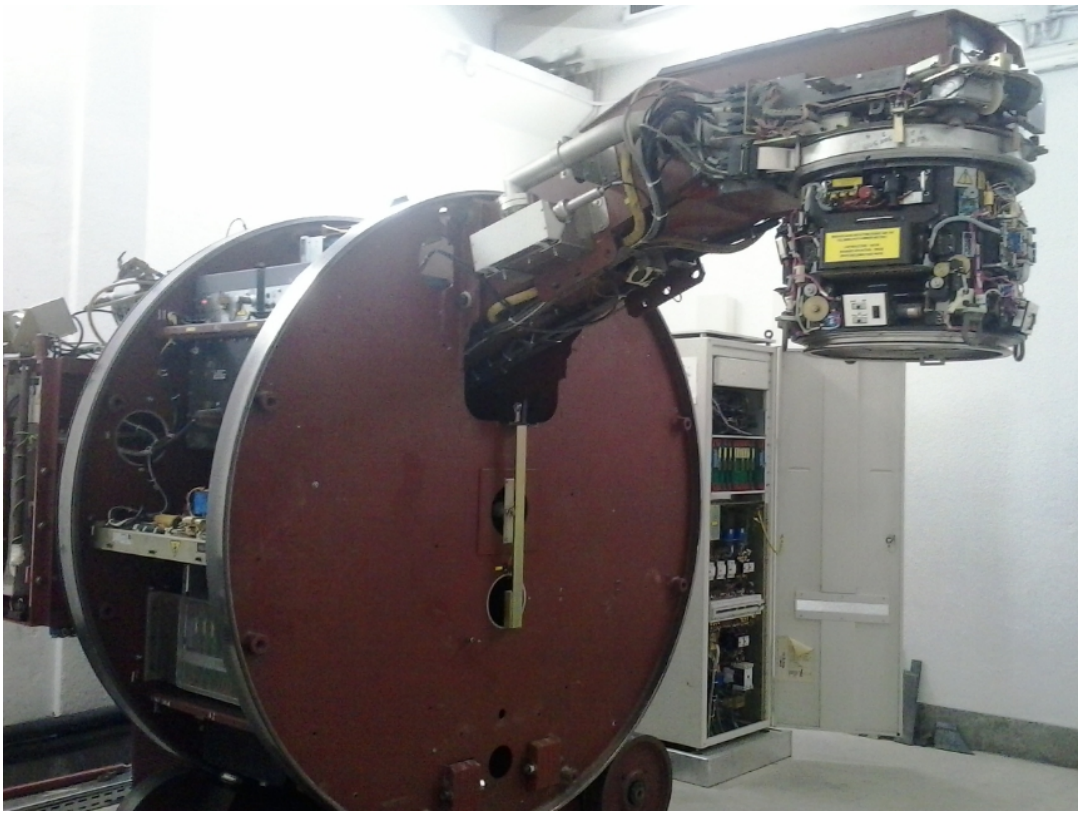

FIGURE 5.1: Linear Accelerator (Linac Elekta SL 25 MV), entirely dedicated to research, located at the physics department of the University of Turin (Italy).

It can accelerate electrons between 4 MeV to 18 MeV using radiofrequency electromagnetic waves, which are pulsed by the magnetron into a linear cylindrical copper waveguide. This structure has copper irises inserted along its length at a certain distance to form a series of cavities. Each cavity has small apertures in which the electrons can pass under vacuum condition (less than 0.0013 Pa) to ensure that other particles do not impede the electrons in their path. This step is synchronized with the injection of electrons into the waveguide by the electron gun, which controls the number of electrons injected by tunning the filament's temperature. The radiofrequency wave accelerates the electrons to the desired kinetic energy by the axial electric field component of the waves. Two sets of quadruple magnets control

the path of the electrons, called steering coils surrounding the waveguide. Two additional sets of focusing coils help define the electron's beam diameter further when it hits the target. At the end of the waveguide, the electrons enter the flight tube. In this part, the beam is redirected and refocused in one *mm* of diameter toward the target using three pairs of magnets on each side of the flight tube. This accelerator can also produce photon beams from the electrons' bremsstrahlung when they hit a tungsten target at the opposite end. These photons are collimated and attenuated in a flattening filter to produce a uniformly distributed clinical photon beam. The dose and beam quality monitoring is performed through two independent ionization chambers, one acting as the primary dosimeter and the second as a backup. Finally, the beam is shaped using an additional collimator called MLC (Multi-leaf-collimator) to ensure that the beam matches the tumor's shape. The entire system is cooled by water.

It is important to point out that this is a conventional LINAC, where the maximum dose-rate that can reach is 0.07 Gy/s, which would be 0.000175 Gy as dose-per-pulse. Therefore, in the present configuration, this accelerator can not be used for FLASH studies.

Fortunately, some changes can be made to this LINAC that can guarantee FLASH beams for electrons, such as the modifications made by (Lempart et al., 2019). The authors reported the modification of a clinical linear accelerator for the delivery of ultra-high dose rate irradiation. These transformations were as follows:

1-) reduced distance with three setup positions

2-) adjusted/optimized gun current, modulator charge rate, and beam steering values for a high dose rate

3-) delivery was controlled with a microcontroller on an electron pulse level

4-) moving the primary and/or secondary scattering foils from the beam path

All these changes made possible a strong increase in dose rate from a few Gy/min to hundreds of Gy/s (dose-per-pulse values from a few 10^{-4} Gy to a few Gy) (Lempart et al., 2019).

In the LINAC located at the University of Turin, following the author's suggestion and guided by ELEKTA technicians, the same modifications were made and at the time of writing this thesis, they are ongoing and will be presented in the following section.

5.2.2 Linac Upgrade "First attempt"

The conversion of the LINAC to produce FLASH electron beams is reversible, and the modifications are straightforward and do not affect the operation of the accelerator. Basically, it was selected 10 MV photon beam energy in the treatment console to deliver electron beams. Thus, the X-ray target was removed from the beam path. Additionally, the secondary filters were also removed, as observed in Fig. 5.2, positioning the carousel on an empty hole. Additionally, the gun current was forced to increase from 5.7 A up to 8.5 A. Finally, an electronic circuit was built to control the number of pulses delivered by the LINAC in each acquisition. This stage will be explained in more detail in the following subsection.

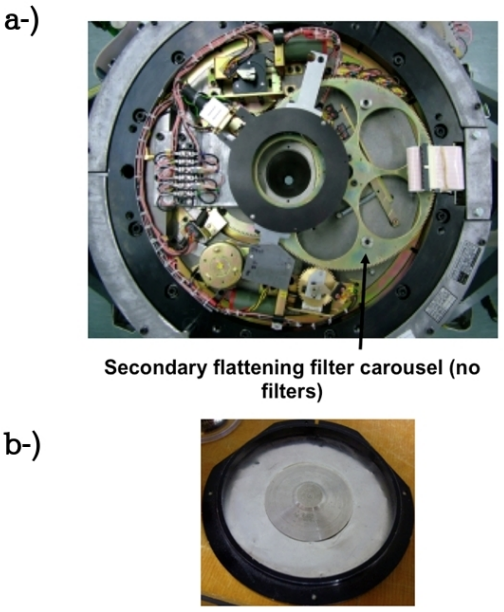

FIGURE 5.2: (a) Collimator assembly looking into the target. (b) Electron secondary scatter filter.

LINAC Pulse counter

Some of the main tasks in the LINAC upgrade is the possibility of controlling the output of the electron beam at the pulse level. Therefore, as shown in Fig. 5.3, the following circuit was simulated, tested, and implemented to perform such a task. The circuit received as the input (see Fig. 5.3, number 1 in red) the current from one strip of a silicon PiN sensor (550 μm width, 4000 μm length, and 60 μm active thickness) without bias voltage. The detector was glued on a PCB, which can bias the detectors with a negative voltage on the

back of the device (in our case, the sensor was not biased). The circuit has three stages of amplification that are between the connector from the label 1 to 3 of Fig. 5.3, using in each one an operational amplifier "TL082CP", in which the first stage works in trans-impedance mode converting the current signal from the sensor into a voltage signal. Its output is followed by a pole-zero cancellation circuit (for baseline restoration). It will then pass through one Sallen-Key filter (In the second stage) in a low pass configuration that filters the high-frequency noise and further shapes the pulse. In the last stage of amplification, a fine tune of the signal amplitude was selected to ensure a proper signal amplitude in the input of the Schmitt trigger (CD74HCT14E). This circuit produces a square pulses of approximately 5 V, which was used as input signals to the interrupt pin D2 of the Arduino NANO board. In the Arduino NANO board, the pulses are counted concurrently with his separations, which can be used as feedback to measured the period between pulses. The connector 2 (in red) can be connected directly to an oscilloscope to observe the pulse shape, as shown in 5.4 for 10 MeV and 400 Hz.

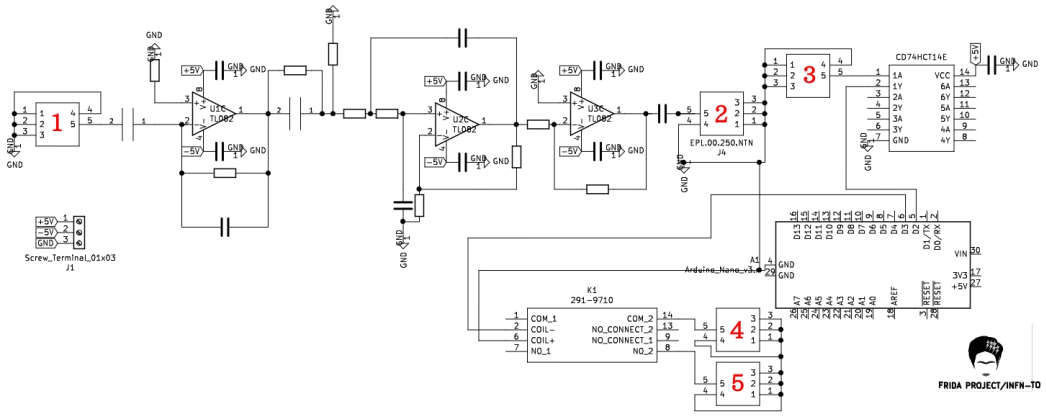

FIGURE 5.3: Schematic representation of the Pulse counter.

In Fig. 5.4 it is possible to appreciate the excellent separation between the signal and the noise, as well the clear space between two consecutive pulses. In that specific case, 2.5 ms between pulses corresponding to 400 Hz was measured, as expected. The Arduino NANO is controlled remotely from the control room using an ethernet connection.

The interface with the LINAC occurs between the connector 4 and 5 (in red, Fig. 5.3) and a relay (291-9710), which works normally open. When the arduino code is open, it sends a digital pulse (HIGH) from pin D3 to the Relay to allow the trigger pulse reach the Linac's thyratron (allowing irradiation). Finally, when a certain amount of pulses is reached (decided by the user),

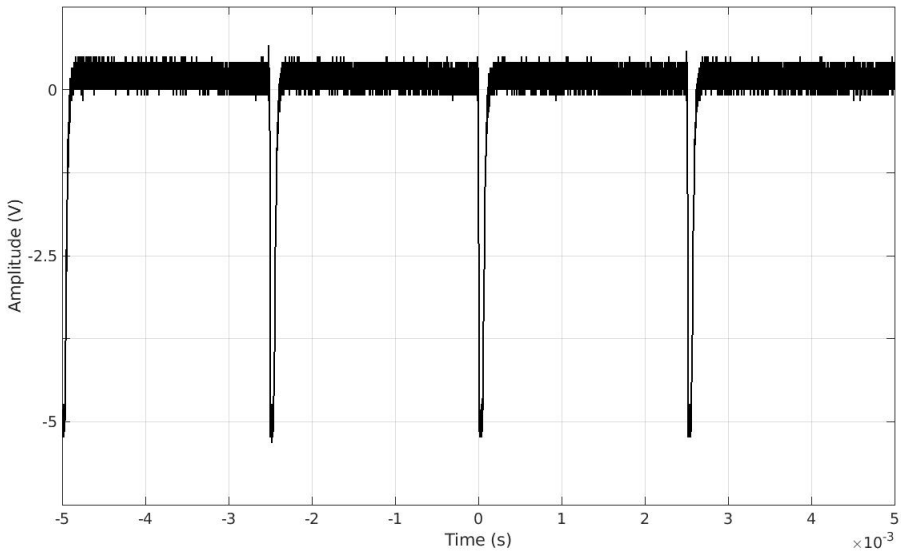

FIGURE 5.4: Example of the pulse counter output using the analog (connector 2 in red in Fig. 5.3) part for 10 MeV and 400 Hz electron beam.

the Arduino write to a digital pin D3, LOW (0 V). Thus, the relay changes its mode to open, preventing any additional trigger pulse reach the Linac's thyratron. In more detail, the pulse counter interrupts the trigger signal coming from the PPG (Programmable pulse generator) board so that it does not reach the thyratron pulser board. The purpose of the PPG board is to generate critical signals that are used to control and synchronize the activities of the HT and RF systems. These connections were done in the connectors J5 and J6 of Fig. 5.5b. The prototype can be visualized in Fig. 5.5a and the PCB already produced by Eurocircuit[1] without the components is presented in Fig. 5.5b.

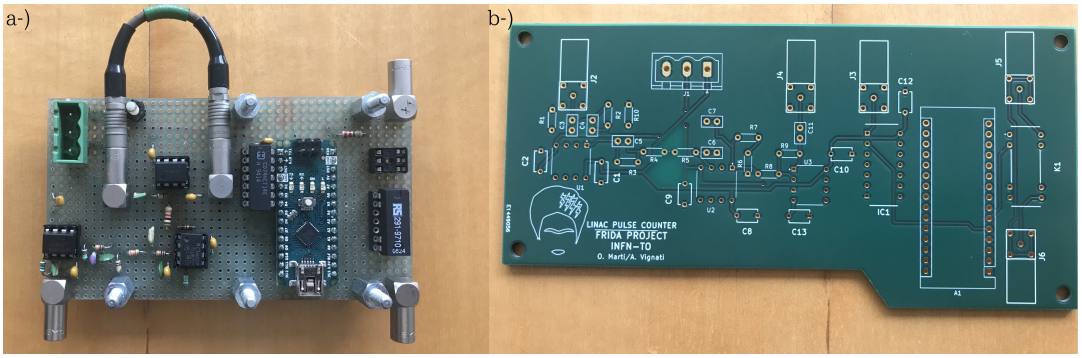

FIGURE 5.5: (a) Pulse counter prototype. (b) PCB of the pulse counter produced by Eurocircuit without the components.

[1]https://www.eurocircuits.com/

Preliminary results of the upgraded LINAC

To test the performance of the LINAC after the upgrade and the pulse counter circuit, the experimental setup shown in Fig. 5.6 was used. Two cylindrical ionization chamber model SNC125c from the Sun Nuclear Corporation[2] for PDD and Dose measurements were also used , however the results are out of the scope of this thesis.

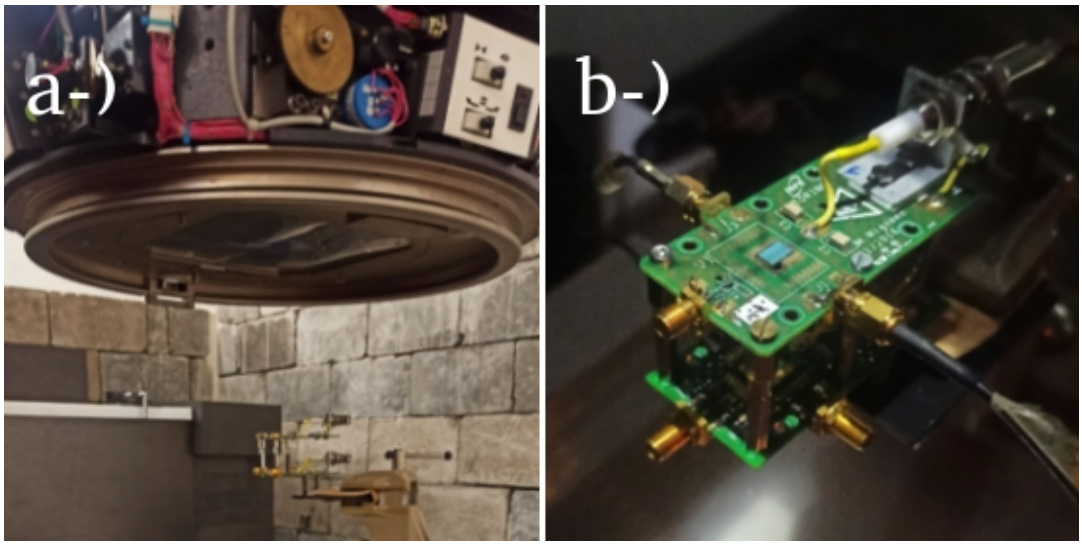

FIGURE 5.6: (a) Experimental setup used during the upgrade. (b) Zoom of Fig. 5.6a. It can be observed the two sensors used, which were placed in a telescope mode at a relatively fixed distance of a few cm between each other.

Two validated T-type sensors from the MoVe-IT 2020 production without implanting the gain layer in any strips were also used in this test. As mentioned in chapter 2, these 11-strip sensors have a breakdown voltage greater than 300 V, making them perfectly suitable for the test.
The two sensors were placed in a telescope mode, at a relatively fixed distance of a few cm between each other. The first sensor was placed at the isocenter (100 cm). A strip from the second sensor (the one furthest from the target) was used as the input for the pulse counter to control the acquisition, as discussed previously. The first sensor was inversely polarized (50 V) and the output of two strips was each read out by a TERA08 chip which is based on the recycling integrator architecture.
The TERA08 chip was initially developed to read out gas monitors in charged particle therapy. It is currently used at CNAO for reading out parallel-plate transmission ionization chambers (Giordanengo et al., 2013). Each TERA08

[2]https://www.sunnuclear.com/

chip hosts 64 identical channels operating in parallel integrated in a 4.5 x 5.4 mm^2 die and is designed in 0.35 μm CMOS technology. Each channel is based on the recycling integrator principle followed by a 32-bit counter with up/down counting capabilities. Therefore it can accept an input current of both polarities. TERA08 operates with a clock frequency of 100 MHz, and to generate a count, five master clock pulses are necessary. For that reason, the maximum conversion frequency is 20 MHz. Using a charge quantum of approximately 200 fC the maximum current that a channel can convert before saturation is about 4 μA. This limit was increased by using a discrete upper-board adapter, which allowed split the input current of the detector into 64 readout channels and then adding up the counts of these channels to reconstruct the input current. It was shown that this method is suitable to increase the maximum input current up to 64 times (256 μA), preserving the good linearity achieved with the individual channels and with a limited increase in the standard deviation of the measurement (Cirio et al., 2015).

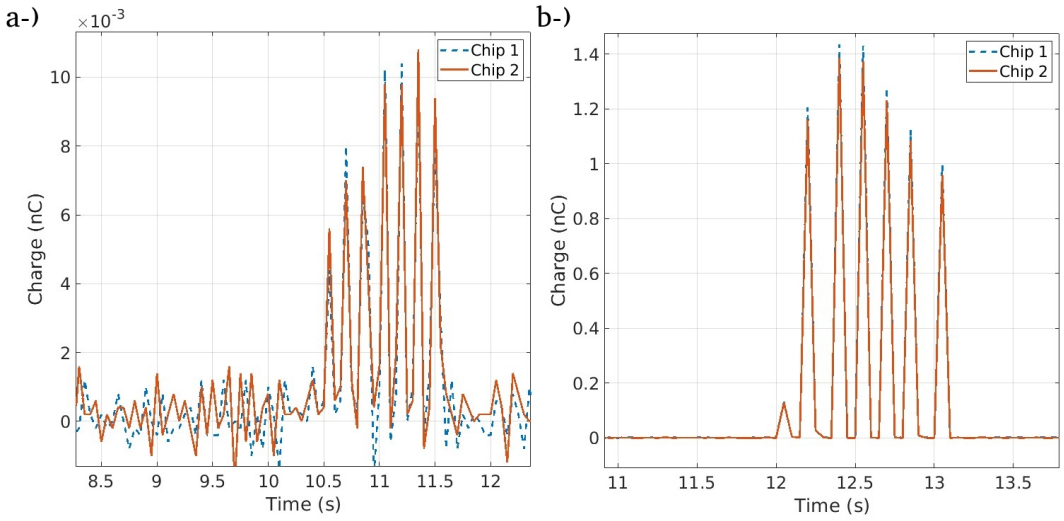

FIGURE 5.7: Example of the output signal (Charge (nC)) after the baseline subtraction of the two TERA08 chips connected to two different strips of the silicon sensor. (a) Conventional irradiation, gun current: 5.7 A, Frequency: 6 Hz. (b) Flash irradiation, gun current: 8.5 A, Frequency: 6 Hz.

The board, hosting two TERA08 chips is controlled by a National Instrument PXI chassis with a 7813R FPGA board, interfaced to the host PC using the LabVIEW FPGA software toolkit. During the beam test after the first attempt of upgrade, it was used the selected electron beam energy for the upgrade (10 MeV) with different pulse frequencies and gun current (5.7 A in normal

Gun current	Mean Charge per pulse(nC)	Max Charge per pulse(nc)	Std	Gain
8.5 A(Flash)	1.244	1.436	0.174	113
8.5 A(Flash)	0.966	1.436	0.314	88
8.5 A(Flash)	0.817	0.973	0.127	74
8.5 A(Flash)	0.641	1.286	0.369	58
8.5 A(Flash)	0.628	1.511	0.502	57
5.7 A(CONV)	0.009	0.011	0.001	–
5.7 A(CONV)	0.011	0.014	0.003	–
5.7 A(CONV)	0.010	0.011	0.001	–
5.7 A(CONV)	0.011	0.013	0.001	–
5.7 A(CONV)	0.012	0.013	0.001	–

TABLE 5.1: Comparison between FLASH and Conventional condition. The reported values are for the chip 1.

mode vs. 8.5 A in flash mode). The objective of this first test was to check the stability of the pulses and the gain in charge per pulse after the modification performed in the accelerator.

An example of the output signal after the baseline subtraction of the two TERA08 chips connected to two different strips of the silicon sensor can be observed in Fig. 5.7. It was fixed to 7 pulses per run by the pulse counter, which anticipates the LINAC interlock. As can be observed in that figure, in both cases, 7 pulses were erogated by the LINAC, as requested. As a first approximation, a gain which is the mean charge per pulse between normal and FLASH condition was about 100. In Table 5.1 the reported values for the chip 1, for the mean charge per pulse, the maximum charge per pulse, and the standard deviation for the last 6 pulses of the seven pulses requested can be seen. It was decided not to use the first pulse, in order to not underestimate the calculation, once in all the tests performed with the FLASH condition, the first pulse always was at least 10 times lower than the next 6 pulses as can be appreciated in Fig. 5.7.

It was observed that for conventional irradiation at 5.7 A the mean charge per pulse was very stable with the values ranging between 0.009 nC to 0.012 nC with a standard deviation about 1 order of magnitude lower. The reported gain in the fifth column is the ratio between the mean charge per pulse (nC) and 0.011 (nC) which was the mean charge per pulse for the 5 test performed at 5.7 A. It was observed a decreased gain in 5 consecutive test for 8.5 A ranging between 113 to 57. This effect was also observed by other authors (Lempart et al., 2019) in which in the first 10 minutes after a warm-up procedure (3000–5000 MU delivery of a 6 MV photon beam), the output (Dose/Charge) was high and stable. After that, the output began to

drop and became more unstable. The reason of this instability, the authors associated it to the dependence upon the temperature and the functionality of some of the linac's components such as the magnetron, the gun, the accelerating waveguide, and beam steering. However, some preliminary results presented by the authors shown that by fine-tuning the resonance frequency of the accelerator can solve those issues without any need of a warm-up procedure. Those suggestions will be considered in the upcoming beam tests.
The preliminary results were for 8.5 A which is the higher gun current available in the accelerator. It was chosen under the hypothesis that higher gun current leads a more intense beam, however, this is not always true as shown by (Lempart et al., 2019). For that reason, a proper scan in gun current vs. charge per pulse, in order to maximize the output is required and will be performed in the future.
Additionally, the pulse stability was checked for various pulse frequencies for 8.5 A. An example of the charge in nC *vs*. time for different frequencies is depicted in Fig. 5.8.

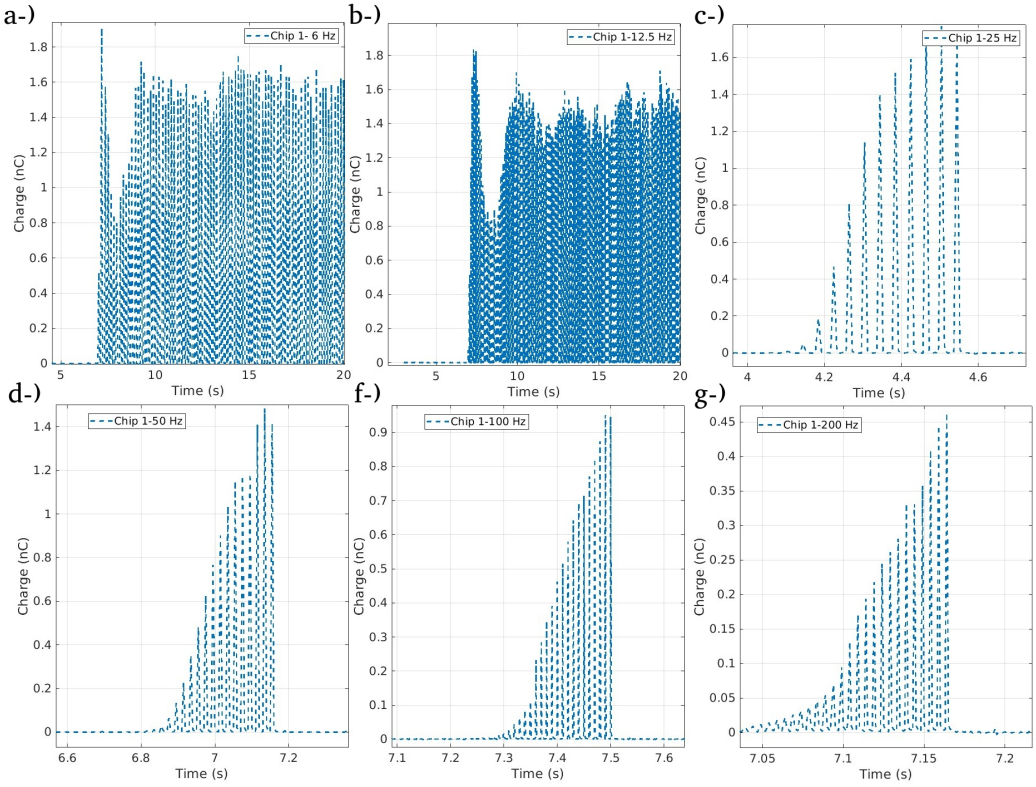

FIGURE 5.8: Charge (nC) *vs*. time (s) for different frequencies: (a) 6 Hz. (b) 12.5 Hz. (c) 25 Hz. (d) 50 Hz. (f) 100 Hz. (g) 200 Hz; Gun current 8.5 A, Chip 1

Curiously, it was observed a pre-saturation peak (The first maximum in Fig.

5.8a and 5.8b). It happens due to the peripheral part of the filament reaches the saturation temperature before the remaining part, creating a momentary maximum. The filament takes some time to reach the working regime, when reaches a homogeneous temperature, the emission current reaches saturation. After that point, a most stable behavior in the emission current is expected, which is translated into a charge per pulse more homogeneous. For instance, a mean charge per pulse (nC) for 10 pulses in the saturation regime of Fig. 5.8a is 1.59 with a standard deviation of 0.08, which is completely different concerning the analysis performed in the first pulses in the pre-saturation regime as shown in Fig. 5.7b and Table 5.1. Unfortunately, due to the time that takes for the filament to reach the working regime, for higher frequencies (Fig. 5.8c-g), it was not possible to observe the saturation regime because of the ionization chamber interlock, which interrupts the acquisition. Nevertheless, it is still feasible to postpone the LINAC interlock via software, in order to conduct measurements with a higher dose-rate. For instance, removing some interlock such as "d1 rst en, d1 relay, d2 rst en, d2 relay, etc", however, by doing that modification the linac still interrupts the delivery between 18-25 pulses (1 Gy/pulse at isocenter) and 200 Hz due to hardwired and cannot be removed through the normal software changes. Therefore, another very risky possibility is to cut the signal from channels 1 and 2 from the monitor chamber. Consequently, the LINAC ionization chamber interlock no longer will tune or stop the delivery.
From that moment, the new device which will be able to stop and control the acquisition will be the pulse counter. In the future, a most extensive testing of the final prototype of the pulse counter is required, after soldering the components (see Fig. 5.5b) to ensure its perfect operation. Importantly, once, we are able to reach a higher dose-rate, after the complete deactivation of the interlocks, the charge per pulse will be always constant, regardless of the dose-rate.

5.3 Beam test at the Centro Pisano Flash Radio-Therapy (CPFR)

5.3.1 From a modified IORT Linac to the ElectronFLASH Linac

Based on the experience of (Lempart et al., 2019), other researchers as (Felici et al., 2020) have also performed a series of modifications to a clinical

accelerator to deliver an ultra-high dose rate, thus transforming an intra-operative radiation therapy (IORT) Linac into a FLASH research machine. The modified accelerator was an IORT NOVAC7 with four nominal electron energies (3, 5, 7, and 9 MeV) that can reach a maximum dose-per-pulse of up to 13cGy/pulse (average dose rate 39 Gy/min) with a pulse length of about 2.5 μs. It is important to highlight that the pulse repetition frequency of this accelerator is relatively low (5 Hz in clinical mode, up to 30 Hz in service mode), and the dosimetric characterization was performed through Gafchromic EBT3 radiochromic films. The transformation of the NOVAC7 accelerator into a FLASH machine is based on the modified collimation system. It comprises passive applicators with different lengths mounted on the accelerator's head, as can be appreciated in Fig. 5.9. The length of the applicator determines the source-to-skin distance (SSD), therefore, a different dose-per-pulse. The applicators consist of polymethylmethacrylate (PMMA) cylinder tubes with 5 mm thick walls each and internal diameters reaching up to 10 cm.

Of the four configurations used in this investigation of SSD for the energy selected (7 MeV e-beam, the most used in the clinical practice): 100 cm, 50 cm, 7 cm, and 1.6 cm, only two showed a dose rate larger than 40 Gy/s. The maximum dose-per-pulse obtained in the four configurations were 0.03, 0.3, 3.9, and 18.2 Gy for an SSD of 100, 50, 7, and 1.6 cm, respectively. In addition, it was measured the depth deposition curve for the two configurations when it reached the FLASH beams (7 cm and 1.6 cm). It was observed a difference in the depth at the build-up in the two configurations due to different electron spectra because the beam exiting the accelerating waveguide has a small but significant low energy tail that not only degrades the beam but also makes it difficult to perform a dosimetric characterization.

After this successful experience, Sordina IORT Technologies S.p.A (S.I.T)[3] developed and built the Electronflash linear accelerators (it works only in electron mode), initially developed without a gun triode. The Electronflash accelerator developed can be installed in a standard radiotherapy bunker thanks to its compact size (1.315 m x 2.131 m). Three versions were designed as follows, with two different electron energies each: 5 & 7 MeV, 7 & 9 MeV, and 10 & 12 MeV. The accelerator has an adjustable radiation field size between 1 and 12 cm in diameter by changing the collimation system mounted on the accelerator's head, the same procedure explained before for the NOVAC7. It can reach a dose rate that can be adjusted between 0.1-1500 Gy/s with a

[3] www.soiort.com

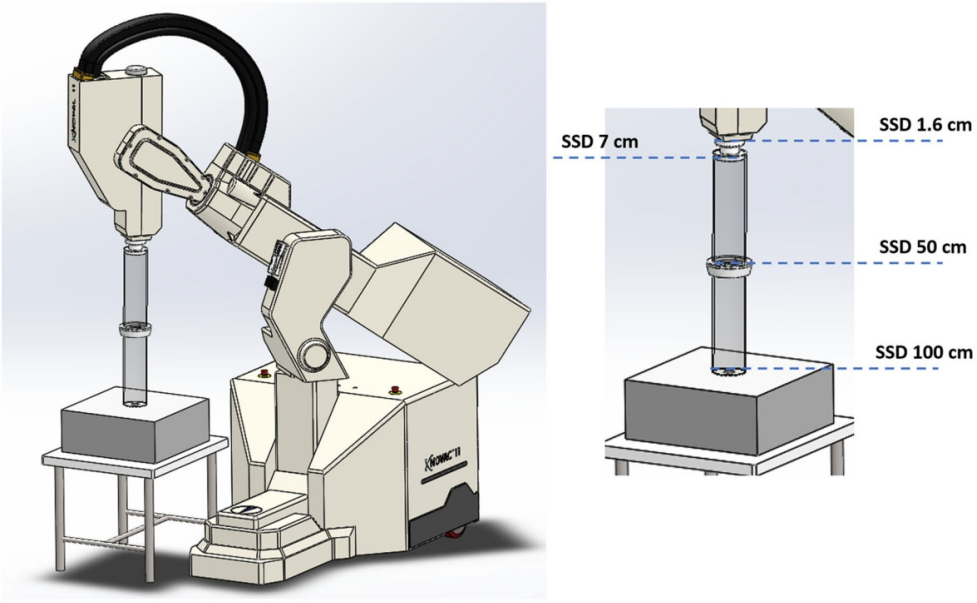

FIGURE 5.9: Four collimation configurations obtained acting on Novac7 collimation system architecture. Picture taken from (Felici et al., 2020).

reference field of 10 cm. For the small field size, the dose rate can reach up to 10000 Gy/s with a dose-per-pulse up to 40 Gy/pulse. In addition, the pulse duration can be modified between 0.5 μs to 4 μs in steps of 0.5 μs. For non-FLASH mode, only noise electrons are accelerated by the radiofrequency cavities. The beam monitoring system consists of a non-invasive system through current measurement for the fluence using toroidal inductors near the exit window and the energy through a pick-up inside the resonant cavity. Two main drawbacks were observed in the first version of this accelerator. The first is that the parameters of interest are dependent on each other, e.g. dose rate, dose per pulse and pulse duration cannot be varied on their own without affecting the other parameters. This limits the type of studies that can be performed. The second is that in non-FLASH mode, only noise electrons are accelerated; therefore, the electron spectrum was slightly different from the FLASH mode, which does not allow a proper comparison between the two modes.

The upgrade version of this accelerator (see Fig. 5.10), was built with gun-triode, like the one installed at the Centro Pisano Flash RadioTherapy (CPFR) for 7 and 9 MeV. It is an improved version of its predecessor that can irradiate in different conditions, for example, conventional and FLASH, without changing the energy spectrum and the experimental configuration.

FIGURE 5.10: ElectronFlash accelerator of 7 MeV and 9 MeV located at the Centro Pisano Flash RadioTherapy (CPFR) in Pisa, Italy.

5.3.2 Experimental setup used in the beam test at CPRF

First tests of silicon sensor's response in Ultra-High dose rate beams have been performed at the ElectronFlash accelerator (EF) of the Centro Pisano Flash RadioTherapy (CPFR) on 9 MeV electron beams.

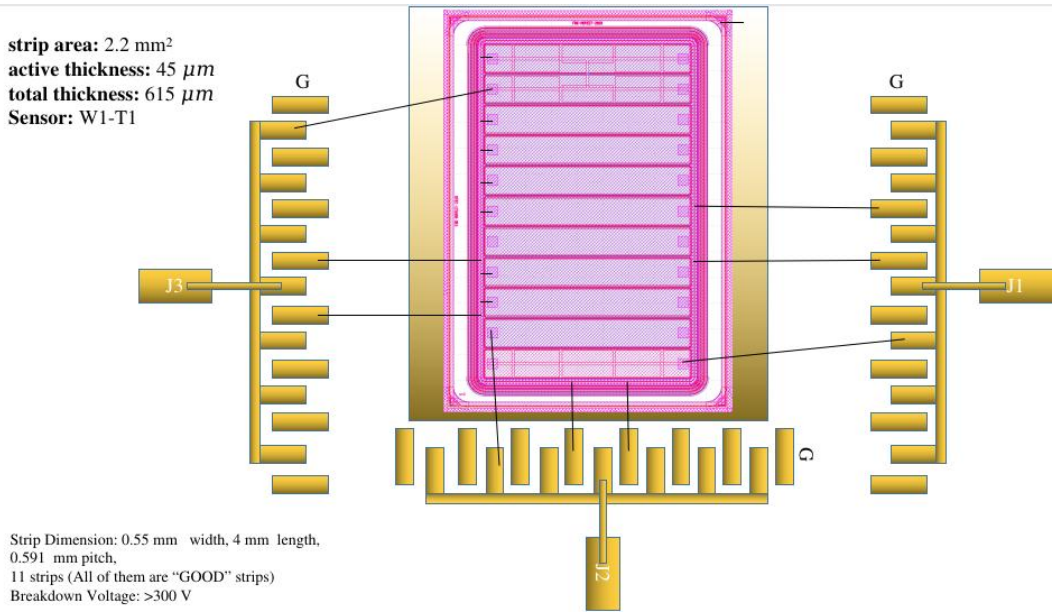

FIGURE 5.11: Schematic of the wire bonding of the sensor tested in UHDR. Additionally, the main characteristic of the detector is described.

Fig. 5.11 shows the schematic of the wire bonding of the sensor selected for testing in UHDR. A validated sensor type T of the MoVe-IT 2020 production was chosen without implanting the gain layer in any strips. It was selected W1-T_1, which was previously measured in the laboratory and has an active thickness of 45μm. All strips were found to have a breakdown above a reverse bias voltage greater than 300 V, therefore, having a perfect behavior. The sensor was glued on a passive PCB board to bias the sensor and extract the signal using the Channels J_3, J_2, and J_1, connected to the strips, from top to bottom: 2, 10, and 11, respectively. As mentioned previously, the strip dimension are: 0.55 mm width, 4 mm length, and 0.591 mm pitch.
The experimental setup used at CPFR is shown in Fig. 5.12. Measurements were performed using a 3 cm and 4 cm diameter PMMA applicator in two different days and the beam was crossing a 13 mm solid water slab before impinging on the silicon sensor. The sensor was placed approximately 3.4 cm from the solid water phantom. Ideally, the sensor is located at the build-up but it was necessary to consider the air gap between the solid water phantom and the sensor to retrieve the expected delivered dose. The three signals from

the board (J_1, J_2, and J_3) were readout by a Lecroy Digital Oscilloscope (Waverunner 640Zi, up to 40 GSample/s, 4 Bandwidth) triggered by the "Beam On" input signal. An additional experimental setup using the TERA08 chip to read out the signal coming from one strip instead of the oscilloscope was also used.

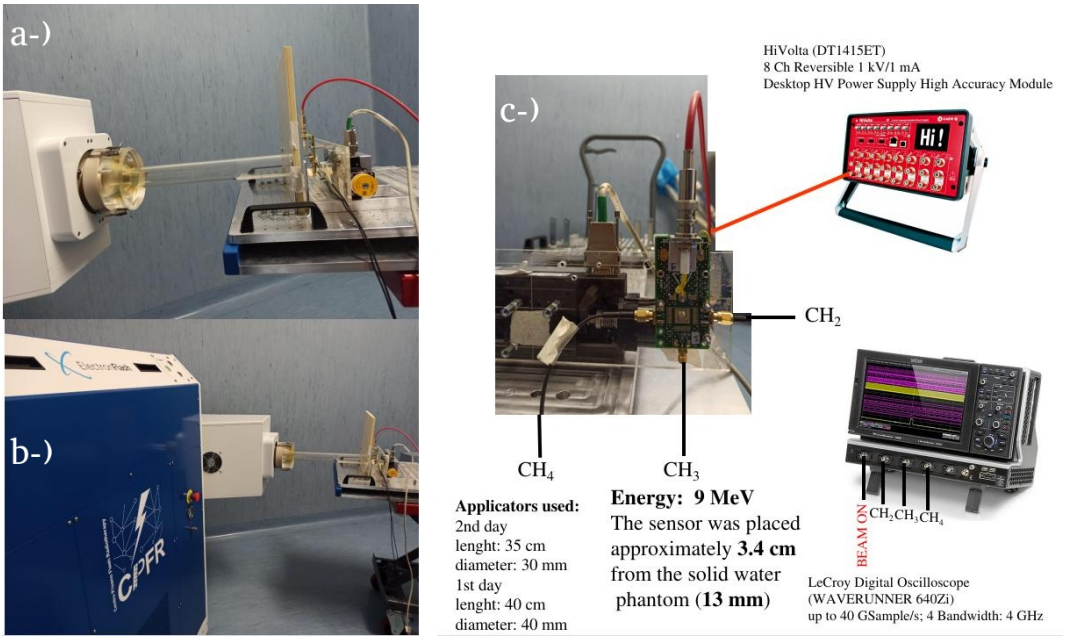

FIGURE 5.12: (a) Lateral view of the experimental setup used at the Centro Pisano Flash RadioTherapy (CPFR). (b) Zoom out of Fig. 5.12a. (c) Positioning of the sensor used at approximately 3.4 cm from the solid water phantom which was located at the exit of the applicator (see Fig. 5.12a and Fig. 5.12b). The three signals from the board (J_1, J_2, and J_3, see Fig. 5.11) were readout by a Lecroy Digital Oscilloscope (Waverunner 640Zi, up to 40 GSample/s, 4 Bandwidth) triggered by the "Beam On" input signal.

5.3.3 Results & Discussion

It was observed saturation in the charge measured by the chip because in the present configuration (splitting the signal among 64 channels) the chip only handles a maximum instantaneous current of 256 μA, still lower compared to the expected values in so intense beam. A very easy solution adopted to increase the range of TERA chip is to extend the signal duration by connecting between the output of the strip and the input of the chip, a RC circuit of $\tau = 2\ ms$. The same approach is reported in the literature by other authors (Kranzer et al., 2022). The linearity of the integrated charge over 10 pulses in 1 Hz of frequency respect to the dose-per-pulse was verified. More details

about these results are beyond the scope of this PhD thesis, as the main objective of this beam test was to test the silicon sensors for the first time, in so intense beams. In Fig. 5.13. can be appreciated the charge produced in 4 $\mu s(nC)$ *vs*. the expected delivered dose per pulse using a reverse bias voltage of 200 V. The measurements were taken in two different days. The three strips of the sensor in both days showed a linear response reaching 4 Gy per pulse ($R^2 \geq 0.99$) which was verified with a PTW FLASH diamond detector. The charge produced on the sensor on the two different days, even using a different applicator, demonstrates the reproducibility of the measurements, showing the potential of silicon sensors for QA and/or real-time beam monitoring for FLASH-RT. Additionally, the charge produced in silicon for different bias voltages and different pulse duration at different doses-per-pulse was also investigated.

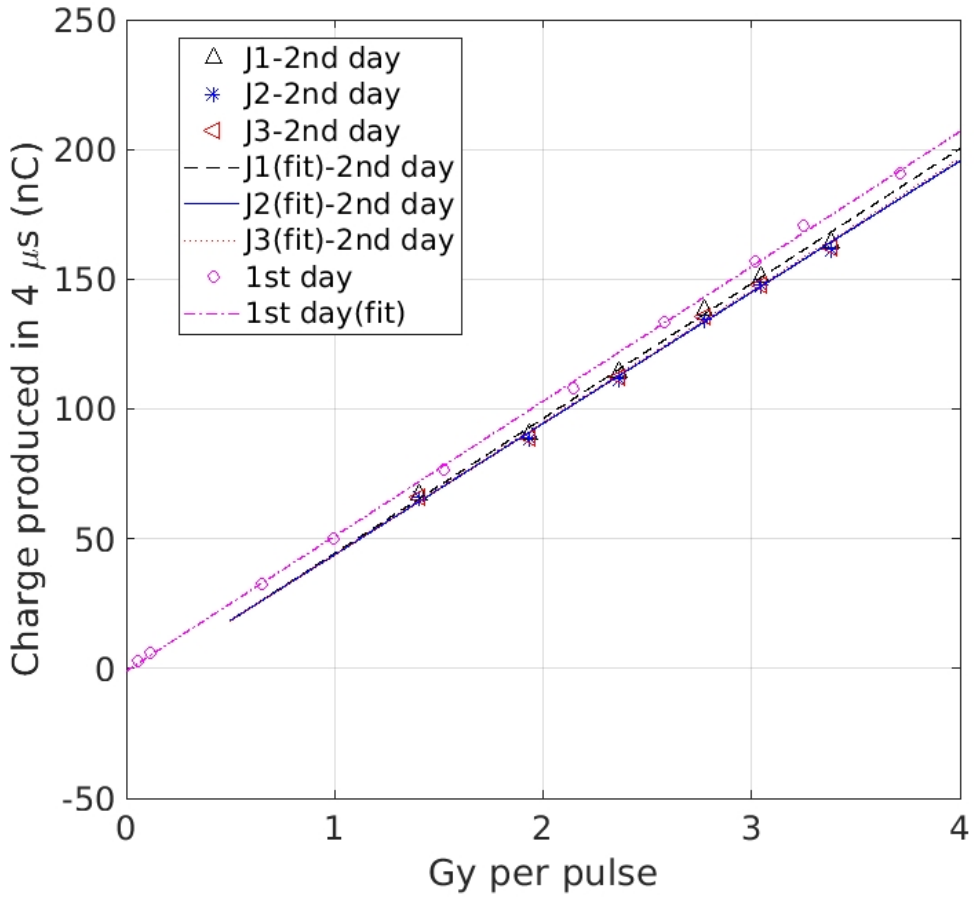

FIGURE 5.13: Charge produced in 4 $\mu s(nC)$ *vs*. the expected delivered dose per pulse using a reverse bias voltage of 200 V. It was obtained an rsquare ≥ 0.99 for all the cases. The measurements were taken in two different days.

Fig. 5.14 shows the overlap of several waveforms which corresponds to acquisitions at different dose-per-pulse using a reverse bias voltage of 50 V and 200 V.

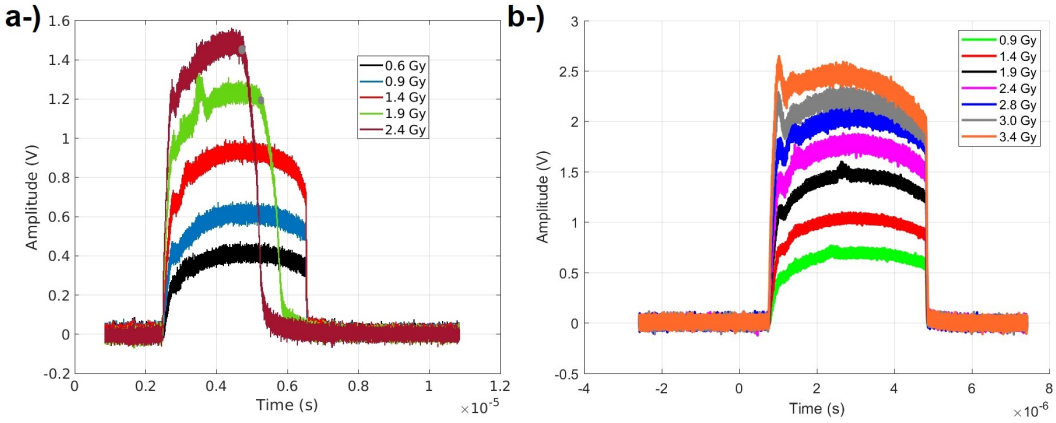

FIGURE 5.14: Example of several waveforms which corresponds to acquisitions at different dose-per-pulse with a duration of 4 μs using a reverse bias voltage of (a) 50 V. (b) 200 V.

In all the acquisitions presented in Fig. 5.14 the pulse duration was fixed to 4 μs, thus, for the case where signal duration was shorter than 4 μs (1.9 Gy and 2.4 Gy in Fig. 5.14a) the detector continues to be irradiated but the e/h pairs created are no longer collected.

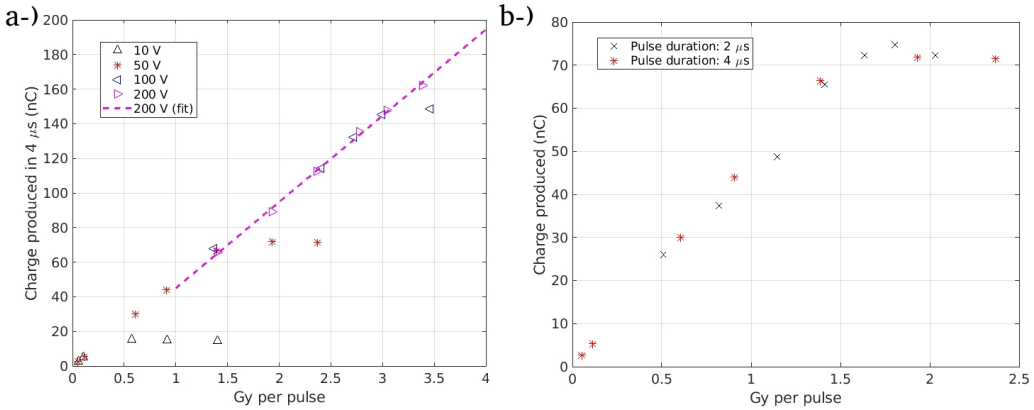

FIGURE 5.15: (a) Charge produced in 4 μs as a function dose per pulse for different bias voltage. (b) Charge produced using 50 V (reverse bias voltage) for two different pulse duration; The results refers to J_1.

A possible explanation of this effect is the creation of an opposite electric field that cancels the drift field, as a first approximation. Interesting, if we integrate the pulse from the beginning to the decay point (marked with a

gray circle) the measured charge is about 70 nC, which can be associated to the finite conductivity of the material. Coincidentally, that value is more or less the last point on the linear response in Fig. 5.15a for 50 V. The same happens for 10 V and 100 V. By increasing the bias voltage, the electric field inside of the silicon is higher and viceversa, therefore, the point in which the curve start to saturate is shift, exactly it was found a quadratic dependence between the bias voltage and that point. For that reason, in Fig. 5.14b it was not observed a saturation due to the higher electric field. Additionally, it was not found a dependence in the pulse duration as shown in Fig. 5.15b for a reverse bias voltage of 50.

This effect of the saturation of the charge produced which has a dependence with the electric field, need to be fully understood. The author encourages further work in that direction making use for example of TCAD simulation in order to study the electric field variation inside the silicon sensor as a function of the dose-per-pulse.

Chapter 6

Conclusions and future perspectives

This PhD thesis is focused on thin silicon sensor for beam monitoring in particle and FLASH radiotherapy. A production of thin silicon LGAD sensor segmented in strips dedicated to beam monitoring application was produced at FBK. The sensors type *A* were tested in laboratory before cutting at FBK and after cutting at the Physics Department of the University of Turin, confirming that the cut did not affect the yield of the production. The static electric test in the whole production proved that the MoVe-IT 2020 sensor production was of very high quality. The width of the inter-strip dead region measured in the sensors designed for counting was 80.8 μm, 22% larger than the distance of the gain layers, and has a small dependence on laser intensities. A preliminary beam test at CNAO using a sensor type *A* showed good separation between signal and noise in the LGAD strip, which allows counting the protons properly by selecting the optimal signal threshold.
In the beam test at Trento Proton Therapy Center (PTC) using a detector prototype made of a telescope of two UFSD sensors (reading only one strip per sensor) to measure the beam energy of a therapeutic proton beam with ToF technique, a few hundred of keV of deviation from nominal energies were achieved for all energies for 97 cm distance between the sensors, corresponding to <1 mm range, as clinically required. The promising results demonstrate that UFSD could represent a viable option for new beam energy monitors, potentially able to measure online the beam energy during irradiation. New experimental setup based on the readout of 8 strips to increase the sensitive area together with a new movement stage to increase the positioning precision was tested at CNAO. Indeed, in the measurements carried out at CNAO using an update version of the telescope system, only 3 energies (59.43, 182.75, and 227.40 MeV) and 4 distances between sensors were necessary to calibrate the system. For the calibration, it was used the self

calibration approach, which is independent from any priori knowledge of the values of nominal energy provided by the clinical facility. The obtained offset was -51.48 $\pm$ 0.72ps. The time resolution shown a dependence on the energy of the protons and the values were between 43 and 67 ps. For all the energies and distances the error in measured the energy was within $\pm$1 mm (less than 0.5 MeV) in water ranges, therefore, within the clinical acceptable accuracy. The most accurate results ($\pm$0.5mm) were for the largest distance as previously obtained in PTC. Finally, even though for the lowest distance the largest error was obtained, they are within the clinical acceptance margin, thus also that distance between detectors can be used to asses the beam energy as well. It was highlighted the lowest distance, once in the future can facilitate the construction of a device of small dimension, that can be useful at the time of daily Quality Assurance procedures.

The preliminary tests of thin silicon sensors for single carbon ions detection on clinical beams performed at CNAO (Pavia, Italy), shows very promising results and preparing the groundwork for future development of a counter and beam energy detector specifically developed for clinical carbon ions. In fact, the time resolution reached was lower than 30 ps for the two energies tested and for all the bias voltages. These values are comparable to the temporal resolution obtained with LGAD, for protons.

A linear accelerator entirely dedicated to research underwent an upgrade of charge per pulse for electron beam of 10 MeV. As a first approximation, a gain of mean charge per pulse between normal and FLASH condition was about 100. It was observed a decreased gain in 5 consecutive test for 8.5 A, ranging between 113 to 57. This effect was also observed by other authors (Lempart et al., 2019) in which in the first 10 minutes after a warm-up procedure (3000–5000 MU delivery of a 6 MV photon beam), the output (Dose/Charge) was high and stable. After that, the output began to drop and became more unstable. The reason of this instability, the authors associated it to the dependence upon the temperature and the functionality of some of the linac's components such as the magnetron, the gun, the accelerating waveguide, and beam steering. However, some preliminary results presented by the authors shown that by fine-tuning the resonance frequency of the accelerator can solve those issues without any need of a warm-up procedure. Those suggestions should be considered in the upcoming beam tests. Additionally, the pulse stability was checked for various pulse frequencies for 8.5 A. It was observed a pre-saturation peak due to the peripheral part of the filament reaches the saturation temperature before the remaining part, creating a

momentary maximum. Unfortunately, due to the time that takes for the filament to reach the working regime, for higher frequencies, it was not possible to observe the saturation regime because of the ionization chamber interlock, which interrupts the acquisition. Furthermore, it was possible to control the LINAC at pulse level very well, thanks to the pulse counter prototype, which during my thesis I designed, simulated, and, tested. In the future, a most extensive testing of the final prototype of the pulse counter is required, after soldering the components to ensure its perfect operation.

Initial tests on 9 MeV electron FLASH beams at the SIT ElectronFLASH Linac installed at the Centro Pisano for Flash RadioTherapy (CPRF) have demonstrated the potential of thin planar silicon sensors to monitor ultra-high dose rate electron beams up to a few Gy/pulse. For reverse bias voltage lower than 200 V, it was observed a saturation in the charge produced in the detector. It has a dependence with the electric field. This phenomena need to be fully understood. The author encourages further work in that direction making use for example of TCAD simulation in order to study the electric field variation inside the silicon sensor as a function of the dose-per-pulse.

Bibliography

Arcidiacono, Roberta et al. (2020). "State-of-the-art and evolution of UFSD sensors design at FBK". In: *Nuclear Instruments and Methods in Physics Research Section A: Accelerators, Spectrometers, Detectors and Associated Equipment* 978, p. 164375.

Bacchetta, N et al. (2001). "Improvement in breakdown characteristics with multiguard structures in microstrip silicon detectors for CMS". In: *Nuclear Instruments and Methods in Physics Research Section A: Accelerators, Spectrometers, Detectors and Associated Equipment* 461.1-3, pp. 204–206.

Bal, Navrit Johan Singh et al. (2021). "Medipix3 proton and carbon ion measurements across full energy ranges and at clinical flux rates in MedAustron IR1". In: *Journal of Instrumentation* 16.12, p. C12002.

Bethe, Hans and Walter Heitler (1934). "On the stopping of fast particles and on the creation of positive electrons". In: *Proceedings of the Royal Society of London. Series A, Containing Papers of a Mathematical and Physical Character* 146.856, pp. 83–112.

Betta, Gian Franco Dalla (2019). "Principles of semiconductor detectors". In: *Detectors and Electronics for High Energy Physics, Astrophysics, Space Applications and Medical Physics: International Course INFN*. URL: https://agenda.infn.it/event/17226/contributions/87527/attachments/62033/74211/Monday-01_04_DallaBetta_GF.pdf.

Bourhis, Jean et al. (2019). "Treatment of a first patient with FLASH-RT". In: *Radiotherapy and oncology* 139, pp. 18–22.

CATANA (2023-02-25). *Centro di AdroTerapia ed Applicazioni Nucleari Avanzate*. URL: https://www.lns.infn.it/it/applicazioni/catana.htm (visited on 02/25/2023).

Chiblak, Sara et al. (2016). "Radiosensitivity of patient-derived glioma stem cell 3-dimensional cultures to photon, proton, and carbon irradiation". In: *International Journal of Radiation Oncology* Biology* Physics* 95.1, pp. 112–119.

Cirio, Roberto et al. (2015). "A simple method to increase the current range of the TERA chip in charged particle therapy applications". In: *Nuclear*

Instruments and Methods in Physics Research Section A: Accelerators, Spectrometers, Detectors and Associated Equipment 798, pp. 107–110.

CNAO (2023-02-25). *Centro Nazionale di Adroterapia Oncologica*. URL: https://fondazionecnao.it/ (visited on 02/25/2023).

Croci, T et al. (2023). "Development and test of innovative Low-Gain Avalanche Diodes for particle tracking in 4 dimensions". In: *Nuclear Instruments and Methods in Physics Research Section A: Accelerators, Spectrometers, Detectors and Associated Equipment* 1047, p. 167815.

Cross, WG et al. (1997). "Physics of the Interaction of Electrons with Matter". In: *Reports of the International Commission on Radiation Units and Measurements* 1, pp. 12–17.

Debela, Dejene Tolossa et al. (2021). "New approaches and procedures for cancer treatment: Current perspectives". In: *SAGE open medicine* 9.

Debrot, Emily et al. (2018). "A silicon strip detector array for energy verification and quality assurance in heavy ion therapy". In: *Medical Physics* 45.2, pp. 953–962.

Di Martino, Fabio et al. (2020). "FLASH radiotherapy with electrons: issues related to the production, monitoring, and dosimetric characterization of the beam". In: *Frontiers in Physics* 8, p. 570697.

DT5742 (2023-02-26). *16+1 Channel 12 bit 5 GS/s Switched Capacitor Digitizer*. URL: https://www.caen.it/products/dt5742/ (visited on 02/26/2023).

Durante, Marco and Harald Paganetti (2016). "Nuclear physics in particle therapy: a review". In: *Reports on Progress in Physics* 79.9, p. 096702.

Fausti, F et al. (2021). "A single ion discriminator ASIC prototype for particle therapy applications". In: *Nuclear Instruments and Methods in Physics Research Section A: Accelerators, Spectrometers, Detectors and Associated Equipment* 985, p. 164666.

Favaudon V, et al (2014). "Ultrahigh dose-rate FLASH irradiation increases the differential response between normal and tumor tissue in mice Sci". In: *Transl. Med* 6.

FBK (2023-02-26). *Fondazione Bruno Kessler*. URL: https://sd.fbk.eu/en/ (visited on 02/26/2023).

Felici, Giuseppe et al. (2020). "Transforming an IORT linac into a FLASH research machine: procedure and dosimetric characterization". In: *Frontiers in Physics* 8, p. 374.

Félix-Bautista, Renato et al. (2019). "Experimental verification of a non-invasive method to monitor the lateral pencil beam position in an anthropomorphic phantom for carbon-ion radiotherapy". In: *Physics in Medicine & Biology* 64.17, p. 175019.

Fernandez, Marcos (2021). "Status report on the radiation tolerance assessment of CNM AIDA2020v2 and HPK-P2 LGADs". In: *16th Trento Workshop on Advanced Silicon Radiation Detectors*.

Ferrero, M et al. (2017). "Developments in the FBK production of ultra-fast silicon detectors". In: *2017 IEEE Nuclear Science Symposium and Medical Imaging Conference (NSS/MIC)*. IEEE, pp. 1–5.

Ferrero, Marco et al. (2021). *An Introduction to Ultra-Fast Silicon Detectors*. CRC Press.

Galeone, Cosimo (2019). "Innovative silicon detectors for measuring the energy of clinical proton beams." In: URL: https://webthesis.biblio.polito.it/12977/1/tesi.pdf.

Gehrke, Tim et al. (2017). "Energy deposition measurements of single 1H, 4He and 12C ions of therapeutic energies in a silicon pixel detector". In: *Journal of Instrumentation* 12.04, P04025.

Giacomini, Gabriele (2021). "Fabrication of silicon sensors based on low-gain avalanche diodes". In: *Frontiers in Physics* 9, p. 618621.

Giordanengo, S et al. (2013). "Design and characterization of the beam monitor detectors of the Italian National Center of Oncological Hadron-therapy (CNAO)". In: *Nuclear Instruments and Methods in Physics Research Section A: Accelerators, Spectrometers, Detectors and Associated Equipment* 698, pp. 202–207.

Giordanengo, S et al. (2022). "Data acquisition system for a 146-channel counter of protons in particle therapy". In: *arXiv preprint arXiv:2205.03051*.

Giordanengo, Simona and Hugo Palmans (2018). "Dose detectors, sensors, and their applications". In: *Medical physics* 45.11, e1051–e1072.

Gómez, Faustino et al. (2022). "Development of an ultra-thin parallel plate ionization chamber for dosimetry in FLASH radiotherapy". In: *Medical Physics* 49.7, pp. 4705–4714.

Gondré, Maude et al. (2020). "Optimization of alanine measurements for fast and accurate dosimetry in FLASH radiation therapy". In: *Radiation research* 194.6, pp. 573–579.

IBA (2023-02-25). *Ion Beam Applications*. URL: https://www.iba-worldwide.com/ (visited on 02/25/2023).

Jayakumar, Raghavan (2012). "Linear Accelerators, the Straight Story". In: *Particle Accelerators, Colliders, and the Story of High Energy Physics: Charming the Cosmic Snake*, pp. 131–145.

Karger, Christian P et al. (2010). "Dosimetry for ion beam radiotherapy". In: *Physics in Medicine & Biology* 55.21, R193.

Kranzer, R et al. (2022). "Response of diamond detectors in ultra-high dose-per-pulse electron beams for dosimetry at FLASH radiotherapy". In: *Physics in Medicine & Biology* 67.7, p. 075002.

Kryder, Cynthia L (2017). "Home Radiation Oncology Proton-Beam Therapy Versus Photon-Beam Therapy: The Debate Continues". In: URL: https://www.ilcn.org/proton-beam-therapy-versus-photon-beam-therapy-the-debate-continues/.

Landau, Lev Davidovich (1944). "On the energy loss of fast particles by ionization". In: *J. Phys.* 8, pp. 201–205.

Lawrence, Ernest O (1934). *Method and apparatus for the acceleration of ions*. US Patent 1,948,384.

Lempart, Michael et al. (2019). "Modifying a clinical linear accelerator for delivery of ultra-high dose rate irradiation". In: *Radiotherapy and Oncology* 139, pp. 40–45.

Leroy, Claude and Pier-Giorgio Rancoita (2011). *Principles of radiation interaction in matter and detection*. World Scientific.

Li, Qiang et al. (2007). "Heavy-ion conformal irradiation in the shallow-seated tumor therapy terminal at HIRFL". In: *Medical & biological engineering & computing* 45, pp. 1037–1043.

LLUH (2023-02-25). *LLU Cancer Center celebrates 30 years of proton treatment*. URL: https://news.llu.edu/patient-care/llu-cancer-center-celebrates-30-years-of-proton-treatment (visited on 02/25/2023).

Malouff, Timothy D et al. (2020). "Carbon ion therapy: a modern review of an emerging technology". In: *Frontiers in oncology* 10, p. 82.

Marinelli, Marco et al. (2022). "Design, realization, and characterization of a novel diamond detector prototype for FLASH radiotherapy dosimetry". In: *Medical Physics* 49.3, pp. 1902–1910.

Marti Villarreal, Oscar Ariel et al. (2021). "Energy measurement of clinical proton beams with a telescope of Ultra-Fast Silicon Detectors". In: *Il nuovo cimento C* 44.143, pp. 1–4.

McManus, M et al. (2020). "The challenge of ionisation chamber dosimetry in ultra-short pulsed high dose-rate Very High Energy Electron beams". In: *Scientific reports* 10.1, p. 9089.

Mirandola, Alfredo et al. (2015). "Dosimetric commissioning and quality assurance of scanned ion beams at the Italian National Center for Oncological Hadrontherapy". In: *Medical physics* 42.9, pp. 5287–5300.

Mitin, Timur and Anthony L Zietman (2014). "Promise and pitfalls of heavy-particle therapy". In: *Journal of Clinical Oncology* 32.26, p. 2855.

Mohamad, Osama et al. (2017). "Carbon ion radiotherapy: a review of clinical experiences and preclinical research, with an emphasis on DNA damage/repair". In: *Cancers* 9.6, p. 66.

Mohammadian-Behbahani, Mohammad-Reza et al. (2022). "Two-channel combination methods for count-loss correction in radiation measurements at high rates and with pulsed sources". In: *Nuclear Instruments and Methods in Physics Research Section A: Accelerators, Spectrometers, Detectors and Associated Equipment* 1040, p. 167195.

Montay-Gruel, Pierre et al. (2017). "Irradiation in a flash: Unique sparing of memory in mice after whole brain irradiation with dose rates above 100 Gy/s". In: *Radiotherapy and Oncology* 124.3, pp. 365–369.

Møller, Chr. (1932). "Zur Theorie des Durchgangs schneller Elektronen durch Materie". In: *Annalen der Physik* 406.5, pp. 531–585. DOI: https://doi.org/10.1002/andp.19324060506. eprint: https://onlinelibrary.wiley.com/doi/pdf/10.1002/andp.19324060506. URL: https://onlinelibrary.wiley.com/doi/abs/10.1002/andp.19324060506.

Neamen, Donald A (2003). *Semiconductor physics and devices: basic principles*. McGraw-hill.

Paganetti, Harald (2018). *Proton therapy physics*. CRC press.

Paternoster, G et al. (2021). "Novel strategies for fine-segmented low gain avalanche diodes". In: *Nuclear Instruments and Methods in Physics Research Section A: Accelerators, Spectrometers, Detectors and Associated Equipment* 987, p. 164840.

Patrignani Claudia, et al. (2016). "Review of particle physics". In: *CHINESE PHYSICS C* 40. DOI: 10.1088/1674-1137/40/10/100001.

Peach, K, P Wilson, and B Jones (2011). "Accelerator science in medical physics". In: *The British journal of radiology* 84.special_issue_1, S4–S10.

Pellegrini, Giulio et al. (2014). "Technology developments and first measurements of Low Gain Avalanche Detectors (LGAD) for high energy physics applications". In: *Nuclear Instruments and Methods in Physics Research Section A: Accelerators, Spectrometers, Detectors and Associated Equipment* 765, pp. 12–16.

Pennazio, Francesco et al. (2022). "Proton therapy monitoring: Spatiotemporal emission reconstruction with prompt gamma timing and implementation with PET detectors". In: *Physics in Medicine & Biology* 67.6, p. 065005.

Petersson, Kristoffer et al. (2017). "High dose-per-pulse electron beam dosimetry—a model to correct for the ion recombination in the Advanced Markus ionization chamber". In: *Medical physics* 44.3, pp. 1157–1167.

PTC (2023-02-25). *Centro Protonterapia di Trento*. URL: https://protonterapia.provincia.tn.it/ (visited on 02/25/2023).

PTCOG (2021). "Particle Therapy Co-Operative Group". In: URL: https://www.ptcog.ch/index.php/ptcog-patient-statistics/.

Rackwitz, Tilmann and Jürgen Debus (2019). "Clinical applications of proton and carbon ion therapy". In: *Seminars in oncology*. Vol. 46. 3. Elsevier, pp. 226–232.

Ramo, Simon (1939). "Currents induced by electron motion". In: *Proceedings of the IRE* 27.9, pp. 584–585.

Ridolfi, Riccardo (2015). "Adroterapia: principi e applicazioni". In: URL: https://core.ac.uk/download/pdf/31158586.pdf.

Royon, Christophe and Nicola Minafra (2021). *Multipurpose front-end board to characterize solid-state sensors for particle detection*. US Patent App. 15/733,977.

Sacchi, R et al. (2020). "Test of innovative silicon detectors for the monitoring of a therapeutic proton beam". In: *Journal of Physics: Conference Series*. Vol. 1662. 1. IOP Publishing, p. 012002.

Sadrozinski, HF-W et al. (2013). "Ultra-fast silicon detectors". In: *Nuclear Instruments and Methods in Physics Research Section A: Accelerators, Spectrometers, Detectors and Associated Equipment* 730, pp. 226–231.

Schüller, Andreas et al. (2020). "The European Joint Research Project UHDpulse–Metrology for advanced radiotherapy using particle beams with ultra-high pulse dose rates". In: *Physica Medica* 80, pp. 134–150.

Shakarami, Zahra (2021). "Development of a novel solid state detector for beam monitoring in proton therapy." In: URL: https://iris.unito.it/handle/2318/1843251.

Shockley, William (1938). "Currents to conductors induced by a moving point charge". In: *Journal of applied physics* 9.10, pp. 635–636.

Sola, V et al. (2019). "First FBK production of 50 μm ultra-fast silicon detectors". In: *Nuclear Instruments and Methods in Physics Research Section A: Accelerators, Spectrometers, Detectors and Associated Equipment* 924, pp. 360–368.

Spieler, Helmuth (2005). *Semiconductor detector systems*. Vol. 12. Oxford university press.

Sung, Hyuna et al. (2021). "Global cancer statistics 2020: GLOBOCAN estimates of incidence and mortality worldwide for 36 cancers in 185 countries". In: *CA: a cancer journal for clinicians* 71.3, pp. 209–249.

Sze, S. M. (2008). *Semiconductor devices: physics and technology*. John wiley & sons.

Tommasino, F et al. (2017). "Proton beam characterization in the experimental room of the Trento Proton Therapy facility". In: *Nuclear Instruments and Methods in Physics Research Section A: Accelerators, Spectrometers, Detectors and Associated Equipment* 869, pp. 15–20.

Uehling, E A (1954). "Penetration of Heavy Charged Particles in Matter". In: *Annual Review of Nuclear Science* 4.1, pp. 315–350. DOI: 10.1146/annurev.ns.04.120154.001531. URL: https://doi.org/10.1146/annurev.ns.04.120154.001531.

UNITO (2023-02-26). *Physics Department of the University of Turin*. URL: https://www.physics.unito.it/do/home.pl (visited on 02/26/2023).

Vavilov, PV (1957). "Ionization losses of high-energy heavy particles". In: *Soviet Phys. JETP* 5.

Verona Rinati, Gianluca et al. (2022). "Application of a novel diamond detector for commissioning of FLASH radiotherapy electron beams". In: *Medical Physics* 49.8, pp. 5513–5522.

Vignati, A et al. (2017). "Innovative thin silicon detectors for monitoring of therapeutic proton beams: preliminary beam tests". In: *Journal of Instrumentation* 12.12, p. C12056.

Vignati, A et al. (2020a). "A new detector for the beam energy measurement in proton therapy: a feasibility study". In: *Physics in Medicine & Biology* 65.21, p. 215030.

Vignati, A et al. (2020b). "Thin low-gain avalanche detectors for particle therapy applications". In: *Journal of Physics: Conference Series*. Vol. 1662. 1. IOP Publishing, p. 012035.

Vignati, A et al. (2022a). "FRONTIER SOLID-STATE TECHNOLOGIES: A POSSIBLE ACE UP YOUR SLEEVE FOR FLASH BEAM MONITORING?" In: *Physica Medica: European Journal of Medical Physics* 94, S68.

Vignati, A et al. (2022b). "Monitoring therapeutic proton beams with LGAD silicon detectors". In: *Journal of Instrumentation* 17.11, p. C11001.

Vignati, Anna et al. (2020c). "Beam monitors for tomorrow: the challenges of electron and photon FLASH RT". In: *Frontiers in Physics* 8, p. 375.

Villarreal, OA Marti et al. (2023). "Characterization of thin LGAD sensors designed for beam monitoring in proton therapy". In: *Nuclear Instruments and Methods in Physics Research Section A: Accelerators, Spectrometers, Detectors and Associated Equipment* 1046, p. 167622.

Villarreal, Oscar Ariel Marti et al. (2022). "Characterization of large LGAD sensors for proton counting in particle therapy". In: *Journal of Instrumentation* 17.09, p. C09022.

Wang, Zhen et al. (2017). "A beam monitor using silicon pixel sensors for hadron therapy". In: *Nuclear Instruments and Methods in Physics Research Section A: Accelerators, Spectrometers, Detectors and Associated Equipment* 849, pp. 20–24.